Repeat LiDAR measurements of a lake-terminating glacier ice cliff

Heather Jane Amanda Bell

Department of Geography

Durham University

2018

Thesis submitted for the degree of Master of Science

Cover image: Fjallsjökull, the lake-terminating glacier in Iceland which is the focus of this study with calved ice floating in the foreground.

Declaration

I confirm that no part of the material presented in this thesis has previously been submitted for a degree in this or any other university. In all cases the word of others, where relevant, has been fully acknowledged.

Heather Bell

Durham University

August 2017

Acknowledgements

Firstly, I would like to thank Sveitarfélagið Hornafjörður (Hornafjörður Municipality), Vatnajökulsþjóðgarður (Vatnajökull National Park), and Rannis (The Icelandic Centre for Research) for allowing us permission to camp in front of Fjallsjökull and undertake this research in Iceland. Also, the Iceland Meteorological Office for providing data from the Kvísker automatic weather station. I extend my gratitude to the Department of Geography for paying for my course fees as an arrangement alongside my part-time job as an Administration Assistant over the last two years, and for the Postgraduate Fund and Research Development Grant which made fieldwork possible.

On a more personal note, I have had an incredible time working and studying part-time in the Department of Geography at Durham University, and there are many people I would like to thank for making my time here so fulfilling. Firstly, to Rachel Carr for encouraging me to pursue an MSc. Mike Lim and Matt Strzelecki, whom I am grateful to for taking me under their wings on fieldwork in Svalbard in 2015. Charlie Bunce, who helped me greatly as a field assistant in Iceland and Dave Evans for allowing us to use his logistics and also for his advice on the fieldsite at Fjallsjökull and Iceland in general. The whole of the Coastal Behaviour and Rates of Activity (COBRA) research group have made my time working in the department so enjoyable, Matt Brain, Nick Rosser, Saskia de Vilder, Simon Varley, Zuzanna Świrad, Sam Waugh, Siobhan Whadcoat, Jessica Benjamin, and Emma Vann Jones, and also the cohort of postgraduates and postdocs from 2015 through to 2017 who I have seen come and go. Also those people who I have gone to ad hoc with questions and who have offered helpful advice, Mark Kincey, Tom Robinson, and Jack Williams.

To my supervisors, Chris Stokes and Nick Rosser who have provided me with sage advice throughout the whole of my degree. Chris Stokes, for his endless enthusiasm and encouragement. Nick Rosser, as both my manager and supervisor has offered me many bright opportunities during my time here, including my part-time jobs on the COBRA project and on the Thames Tideway Tunnel project, and also for shipping me off to Svalbard in my first year which was an adventure. Finally, to Peter Wollaston and my family.

Thank you all, kindly.

Heather.

Abstract

The use of repeat LiDAR measurements to monitor processes of rockfall and landslides is well established in the geosciences, but only a limited number of studies have applied this method to study ice cliff processes and change at the termini of calving glaciers. In this study, the terminus of Fjallsjökull, an outlet glacier in SE Iceland, was scanned using a Riegl *VZ*-4000, a very-long-range laser scanner which has sufficient sensitivity to obtain laser reflections from ice surfaces and was programmed to acquire data automatically each hour, over a diurnal cycle (13th–14th August 2016). A total of 46 scans were captured across a 1300 m wide section of the terminus from a range of c. 1000 m, generating an average point spacing of 0.15 m. A 300 m wide area of interest was used in subsequent data processing for scans over a 28-hour period. Change analyses show that calving is the dominant mode of ice loss for the subaerial ice cliff, with 70% focussed in the bottom third (11 m) of the ice cliff. Calving events were distributed across the width and height of ice cliff face, but the two largest events (of volumes ~4000 m^3 and ~3000 m^3) appeared to begin with a small failure (< 10 m^3) at the waterline which then propagated up-cliff 30 to 60 minutes later. Precursory deformation of the ice cliff face in the order of 2.00 m h^{-1} (greater than the average velocity of 0.15 m d-1) and forward rotation from the toe of the ice cliff is also observed prior to failure. Calving event scars are also observed to evolve between scans with smaller failures coalescing with subsequent failures. This study shows that a new generation of terrestrial laser scanners can be used to automatically monitor processes at the termini of calving glaciers at exceptionally high temporal and spatial resolutions.

Units

The units used in this thesis are listed below.

Quantity	Name	Symbol
Length	metre	m
Time	second	s
Celsius temperature	degrees Celsius	°C
Mass	Mean water equivalent	m w.e.
Elevation	Metres above sea level	m a.s.l
Degree of arc	degree	°
Volume	Metre cubed	m^3

List of abbreviations

LiDAR	Light Detection and Ranging
TLS	Terrestrial Laser Scanning
DEM	Digital Elevation Model
DoD	Digital Elevation Model of Difference
GPS	Global Positioning System
AOI	Area of Interest
C2C	Cloud-to-Cloud
TIN	Triangulated Irregular Network
SOCS	Scanner's Own Coordinate System
PRCS	Project Coordinate System

Note on coordinate axis

In most of the discussions herein a rectangular coordinate system is used with the *x*-axis horizontal or sub horizontal and in the direction of flow, the *y*-axis horizontal and transverse, and the *z*-axis normal to the other two, being vertical or slightly inclined to vertical.

Note on translation

Many frequently used Icelandic suffixes in this thesis will not be repeated in English. These include the following: ***-jökull*** = glacier, outlet glacier; ***-fjall*** = mountain; ***kvísl*** = river; ***-lón*** = lake, reservoir. The Icelandic word ***jökulhlaup***, meaning pro- or subglacial outburst flood is an internationally accepted scientific term for this phenomenon and therefore will be used without further translation. In a similar way, the Norwegian suffix ***-breen*** = glacier, for example, the glacier ***Hansbreen***, and the Swedish ***-glaciären*** = glacier and will not be repeated in English.

Contents

List of Figures

List of Tables

Chapter 1

Introduction

Since the latter half of the 20th century there has been a progressive increase in the number and volume of ice-marginal lakes worldwide (Figure 1.1; Richardson & Reynolds, 2000; Stokes *et al.*, 2006; Schomacker, 2010; Trüssel *et al.*, 2013; Carrivick & Quincey, 2014) and, although there is no global inventory to document these changes, the pattern is expected to continue in line with future climate change predictions (Vaughan *et al.*, 2013). The onset of calving at previously land-based glacier termini can lead to enhanced rates of retreat (Pelto *et al.*, 2013) and plays a crucial role in glacier dynamics (Schomacker, 2010). Calving at glacier termini is a mechanical process of ablation which occurs when fracture propagation through the ice column causes the detachment of blocks of ice (Benn *et al.*, 2007b). At present, outlet glaciers from the Vatnajökull Ice Cap in Iceland, Europe's largest ice cap, are undergoing accelerated rates of retreat due to the increased heat capacity of ice-marginal lakes and the development of calving fronts (Schomacker, 2010). On millennial timescales, the melting to calving transition has been suggested to represent a sharp threshold signalling rapid deglaciation (Kirkbride, 1993). Despite the importance of calving as a mechanism of ice loss, the processes by which it occurs, particularly at lacustrine glacier termini are not fully understood (Van der Veen, 2013; Sugiyama *et al.*, 2016) and, therefore, conditions at the ice cliff are not well

Figure 1.1) Photograph of the fieldsite investigated in this study. The proglacial lake Fjallsárlón and the calving front of Fjallsjökull on the 14th August 2017. Fjallsjökull is an outlet glacier of the Vatnajökull Ice Cap, Iceland. The lake was first observed in aerial imagery in 1945 (Howarth & Price, 1969) and has been expanding until the present day. The terminus of Fjallsjökull is approximately 3 km wide, most of which terminates in the lake.

represented in numerical models (Bassis, 2011). In contrast to the numerous studies which have focussed on the processes of tidewater calving, there are few studies which have reported specifically on the processes of lacustrine calving (Sugiyama *et al.*, 2016), particularly at short (sub-daily) timescales (Chapuis & Tetzlaff, 2014) and at high spatial resolutions (sub-metre). This constitutes a gap in the knowledge of the processes that occur at lacustrine glacier ice cliffs (Van der Veen, 2013) and how these may relate to calving due to the methods which have been used to study them (Chapuis & Tetzlaff, 2014). A new generation of terrestrial laser scanners (e.g. Riegl VZ-4000 & VZ-6000) which are capable of acquiring rich topographic data from ice surfaces at high spatiotemporal resolutions (Gabbud *et al.*, 2015; Riegl Data Sheet, 2015) have the potential to allow the investigation of the processes which operate at the termini of lacustrine glaciers at a level of detail which up until now has not been possible. However, so far, no time series data using this technique has been published (Chapuis & Tetzlaff, 2014).

This thesis demonstrates the use of terrestrial laser scanning and discusses how similar future studies could improve our understanding of the processes which operate at the termini of lacustrine glaciers, and how this is important in terms of modelling and predictions of future ice loss (see aims in Section 1.3).

1.1 The role of ice-marginal lakes in the present day global deglaciation

In general, contemporary calving into proglacial lakes at mountain glacier and ice sheet margins has been shown to exacerbate ablation by introducing mechanical and thermal stresses (Carrivick & Tweed, 2013). These additional stresses permit ice to be lost from glaciers at much greater volumes than would be possible through surface ablation alone (Van der Veen, 2002). Conversely, and serving to highlight the complexity of the relationship between coupled proglacial lakes and lake-terminating glaciers, some studies have shown that very large lakes can moderate summer air temperatures and delay summer ice ablation (Carrivick & Tweed, 2013).

Research in the Russian High Arctic has shown that at multi-decadal timescales, glacier retreat rates can be significantly different depending on whether glaciers terminate on land, into lakes, or the sea (Figure 1.2; Carr *et al.*, 2017). Carr *et al.* (2017) show that glaciers which terminate into lakes or the ocean receded 3.5 times faster than those which terminate on land. The importance of this terminus type is further evidenced in the Quaternary record, during deglaciation from the Last Glacial Maximum (Stokes & Clark, 2004; Pollard, 1984; Cutler *et al.*,

2001) and recorded in deep-sea sediment records (Heinrich, 1988; Bond & Lotti, 1995), whereby proglacial lakes and embayments have been linked to the rapid demise of ancient ice sheets (e.g. the Laurentide Ice Sheet). Moreover, geomorphological evidence from New Zealand suggests that similar calving phases have not occurred since the Late Pleistocene deglaciation, indicating that contemporary changes to glacier termini are of great significance in the Holocene (Kirkbride, 1993). When used as an analogue, the collapse of the Laurentide Ice Sheet may offer insights into future changes of the Greenland Ice Sheet over the coming century (Carlson *et al.*, 2008), and, perhaps, the role of ice-marginal lakes and lacustrine calving to the present day global deglaciation.

1.2 Iceberg calving as a hazard

The present day increase in the numbers of lacustrine calving glaciers has wide-reaching implications. Direct short-term hazards to human life and infrastructure originating from iceberg calving exist in the form of glacial outburst floods (GLOFs) (Figure 1. 3; Richardson & Reynolds, 2000) and calving tsunamigenesis at the glacier ice-lake interface (Lüthi & Vieli, 2016; Kohler, 2008). The products of calving, icebergs (freeboard 4 m a.s.l), bergy bits (freeboard 1-4 m a.s.l), and growlers (freeboard < 1 m a.s.l) can cause iceberg-capsize tsunamigenesis (Macayeal *et al.*, 2011) and also introduce hazards to shipping (Hill, 2000). In 1996, for example, the collapse of 10,000 m^3 of ice at the Miage Glacier, Italy caused a calving tsunami which injured around a dozen tourists (Tinti *et al.*, 1999).

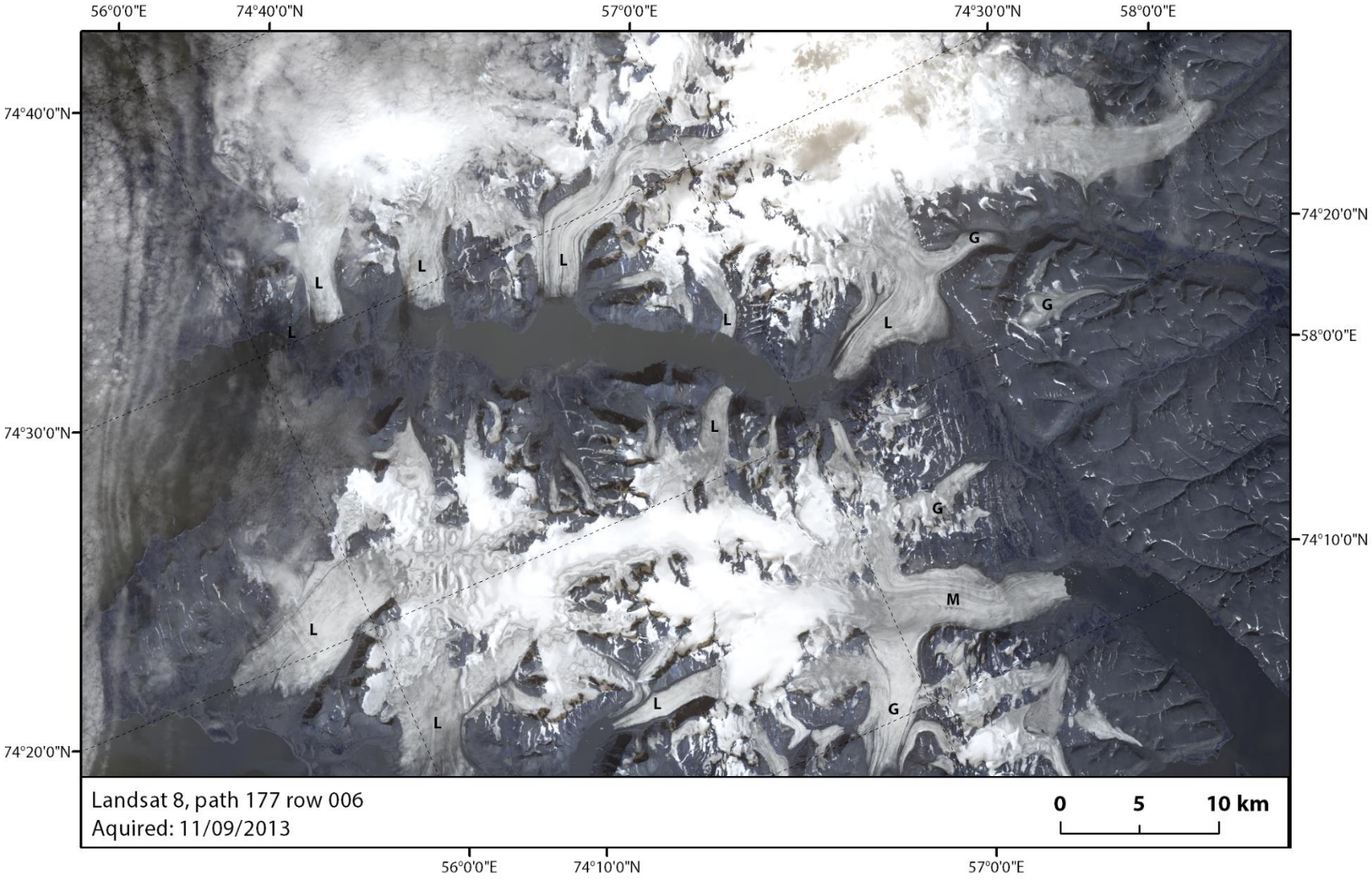

Figure 1.2) Glaciers in the Russian High Arctic, Novaya Zemlya. Land-, lake- and marine-terminating glaciers are all observed in this image, labelled 'G', 'L', and 'M', respectively. Lake- and marine- terminating glaciers have been shown to retreat significantly faster than land terminating glaciers in the same area.

Despite the importance of lacustrine calving and the role it may play in changes to future glacier dynamics and in amplifying glacial retreat, many of the physical mechanisms and the interplay between them remain unknown (Van der Veen, 2013; Benn *et al.*, 2007a), particularly for lake-terminating glaciers. This gap in knowledge is highlighted by the lack of realistic simulations of calving, which stems largely from the lack of observations of calving at glacier termini particularly for lake-terminating glaciers, which are known to be widespread (Stokes *et al.*, 2006; Schomacker, 2010; Carrivick & Quincey, 2014; Jóhannesson *et al.*, 2013). Understanding the mechanisms which control calving, and through which it occurs is therefore an important issue, which is widely identified in the literature (Chapuis & Tetzlaff, 2014; Benn *et al.*, 2007b; Åström *et al.*, 2014; Petlicki *et al.*, 2015; Murray *et al.*, 2015a).

Figure 1.3) Evidence of a GLOF breaching a moraine-dammed proglacial lake in Peru (Mountain Research Initiative, 2016).

1.3 Research questions and aims

Through a comprehensive review of the presently available literature on the dynamics of calving (see *Chapter 2*), a number of research questions have been formulated:

RQ1 What are the spatial characteristics of calving behaviour at the ice cliff at hourly to sub-hourly timescales?

RQ2 Are the factors controlling the pattern of ice loss at the terminus over a diurnal cycle solely due to external environmental forcing, or due to internal glacial dynamics, or are they time-dependent?

RQ3 Do observations of the magnitude/frequency of events match those from previous research on calving?

The aims of this research project are to (1) monitor the ice cliff of a lake-terminating glacier near-continuously, at hourly to sub-hourly intervals and at a high spatial resolution (<1.0 m); (2) observe calving processes at the single event scale from successive sub-metre TLS derived DEMs over at least one diurnal cycle; (3) describe the automatic monitoring method used and the techniques used for processing TLS data and quantifying glaciological processes; (4) investigate the temporal relationships between patterns of change and potential calving mechanisms.

Chapter 2

A review of the research into lacustrine calving

2.1 The occurrence and distribution of lacustrine calving glaciers

An increasing number of lacustrine calving glaciers have begun to form in many regions worldwide, in response to a changing climate. There is, however, no global inventory indicating the prevalence of this terminus type. Lacustrine calving margins generally form where proglacial lakes form behind moraine or ice dams. Conditions at the bed of calving glaciers can be cold or temperate, and either grounded, floating or near flotation (Figure 2.1). Furthermore, research has shown that lacustrine calving glaciers form a population distinct from both tidewater and non-calving glaciers in terms of stability, climate sensitivity, and dynamics (Warren *et al.*, 2001). Calving environments differ and, therefore, calving glaciers produce a variety of ice detachments ranging from large tabular icebergs such as those observed at Glacier Nef, Patagonia (Warren *et al.*, 2001), to the smaller bergy bits and growlers which were been observed to detach at Fjallsjökull, Iceland in this study.

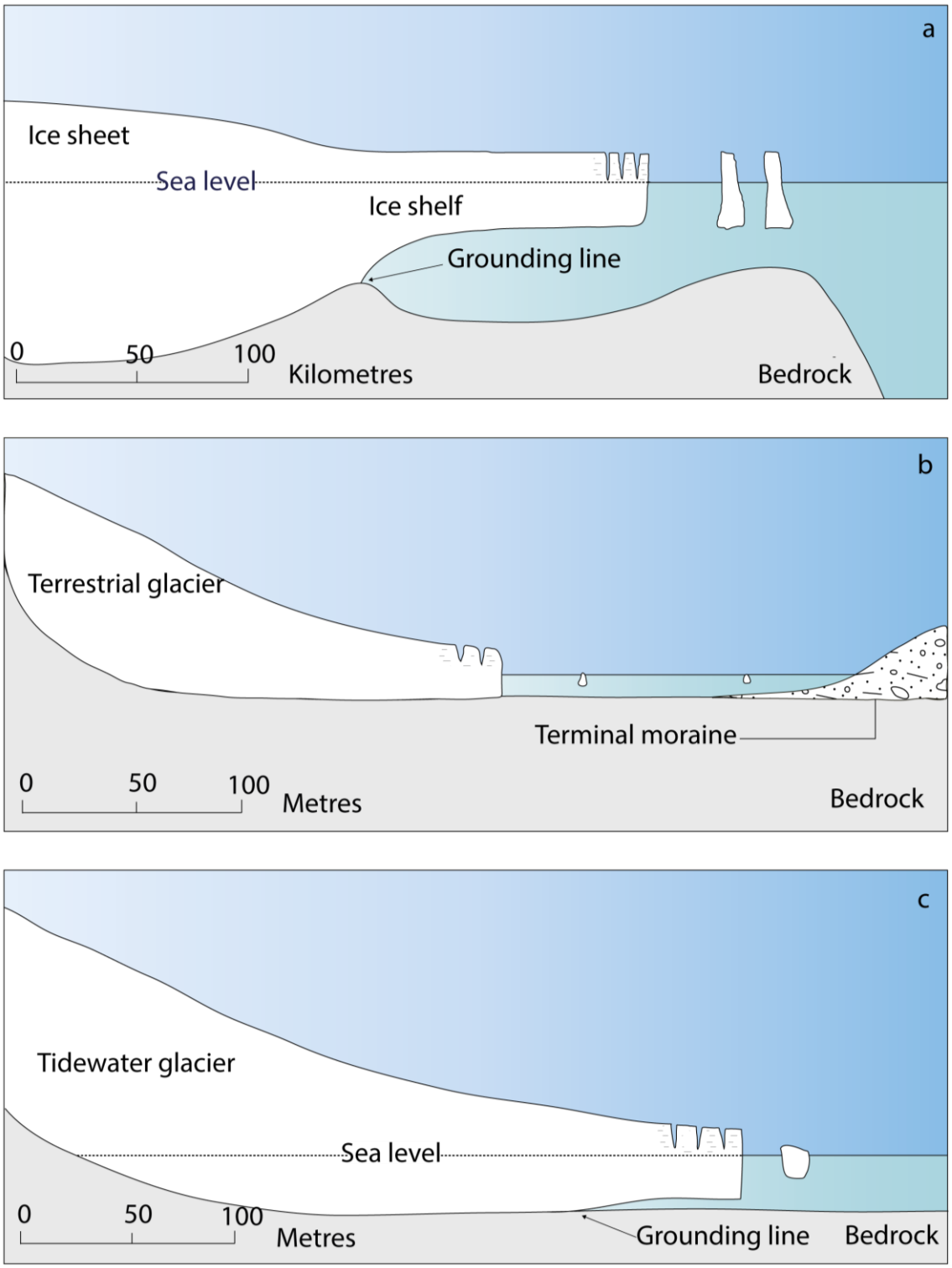

Figure 2.1) Examples of simplified calving glacier margins. a) Fully floating ice shelf, e.g. the Ross Ice Shelf, Antarctica; b) Lacustrine calving glacier terminating in shallow water with a fully grounded terminus; c) Tidewater glacier, whereby floating begins to occur at the grounding line, marked in a) and d).

2.2 Glacier dynamics and calving processes

2.2.1 The relationship between calving processes and glacier dynamics

The relationship between calving processes and glacier dynamics is a contentious issue. Much of the foundational work on calving dynamics was established using data from Columbia Glacier, a tidewater glacier in Alaska, which has led to a disproportionately large number of studies focussing on the dynamics of tidewater glaciers (Benn *et al.*, 2007b). Less attention has therefore been directed to studying lacustrine calving margins, which has led, perhaps, to the general assumption that the calving dynamics of these two different calving margins are assumed to operate in more or less the same way. However, research conducted on glaciers terminating in hydropower storage lakes revealed that lacustrine calving rates were lower than those of tidewater glaciers (Bindschadler, 1983; Funk & Röthlisberger, 1989), and further investigation of lacustrine calving glaciers in environments of analogous settings to tidewater glaciers (e.g. Kirkbride & Warren, 1997; Rott *et al.*, 1998; Skvarca *et al.*, 2002; Warren & Kirkbride, 2003), showed that lake-terminating glaciers calve at an order of magnitude less than tidewater glaciers.

With such a notable difference between different calving regimes, this has prompted some to question the processes which control calving, and whether these are fundamentally different in disparate environments or that perhaps they operate at different scales (Van der Veen, 2002; Bassis & Jacobs, 2013). The general differences in calving rates have been attributed to contrasts in water densities, upwelling and subaqueous melt rates, frontal over steepening and longitudinal strain rates (Funk & Röthlisberger, 1989; Venteris *et al.*, 1997; Whillans & Van Der Veen, 1997; Warren *et al.*, 2001; Warren & Kirkbride, 2003; Sugiyama *et al.*, 2016).

One key debate has discussed whether calving activity is the cause or the consequence of ice flow acceleration (Benn *et al.*, 2007b). A body of research developed around these two concepts, which are generally referred to as the 'master and slave' hypotheses (Benn *et al.*, 2007b). The 'master' relationship views calving as triggering a cascade of dynamic changes up-glacier, leading to flow acceleration (Figure 2.2; Hughes, 1986; Meier & Post, 1987; Meier, 1994, 1997; Howat *et al.*, 2005; Trüssel *et al.*, 2013), and the 'slave' relationship sees calving as an almost passive response to changes in other parts of the glacier system (Van der Veen, 1996; Venteris *et al.*, 1997; Van der Veen, 2002). Interestingly, both of these contrasting perspectives were developed using the Columbia Glacier dataset. Benn *et al* (2007b) maintain that calving and the dynamics of calving glaciers can only be understood as inseparable parts of an intricately coupled system and that to phrase the dynamics of calving in terms of 'master' and 'slave' is to give rise to a false dichotomy.

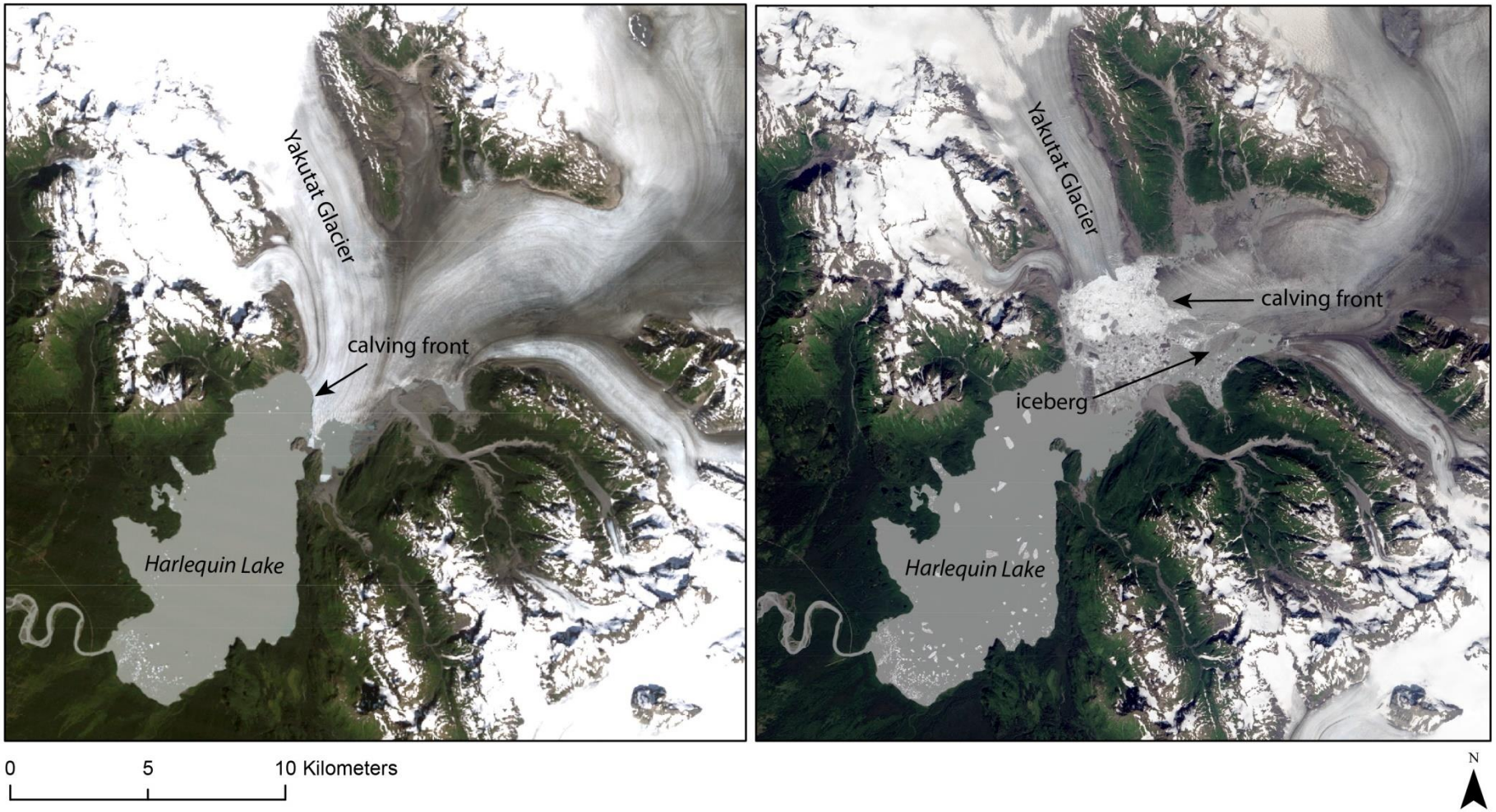

Figure 2.2) Landsat 8 NASA Earth Observatory image of Yakutat Glacier, Alaska. Left in 1987; right in 2013. Yakutat Glacier, a lacustrine calving glacier, is one of the fastest retreating glaciers in the world and retreated more than 5 kilometres between 1987 and 2013. Over the past few years, a long floating ice tongue has been breaking down which is thought to have triggered dynamic changes in the terminus of Yakutat Glacier.

2.2.2 The underlying mechanism of calving

Calving is a multifaceted process and is controlled by a variety of complex processes (Benn *et al.*, 2007b) but all calving events occur when fractures propagate and isolate blocks of ice from the main body of the glacier. Tensile stresses associated with longitudinal and transverse flow gradients in ice velocity are frequently large enough to generate crevasse formation on glaciers and ice shelves (Van der Veen, 2013; Benn & Evans, 2010). Crevasses, whether advected down-glacier, or propagated near the margins of calving glaciers, act as preferential lines of weakness. These are the mode 1 type failure, which opens in response to tensile stresses pulling the walls of a crack apart. Mode 2 which occurs as a result of shear stresses applied in the plane of the fracture, and mode 3, tearing, which is a result of applied shear stress parallel to the leading edge of the crevasse (Figure 2.3; Van der Veen, 2013). In reality, fracture events can involve two or three modes simultaneously, termed a mixed mode fracture.

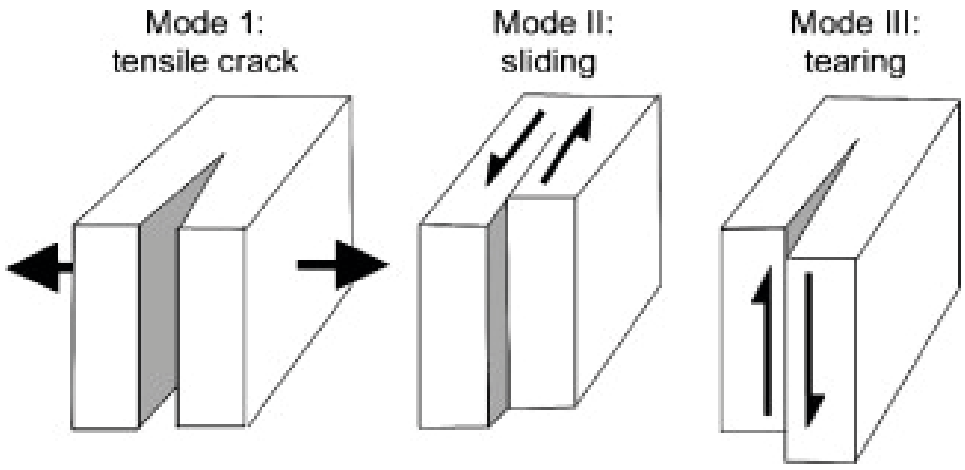

Figure 2.3) Schematic diagram of the three basic modes of fracturing (Benn *et al.*, 2007b, p. 149 https://doi.org/10.1016/j.earscirev.2007.02.002).

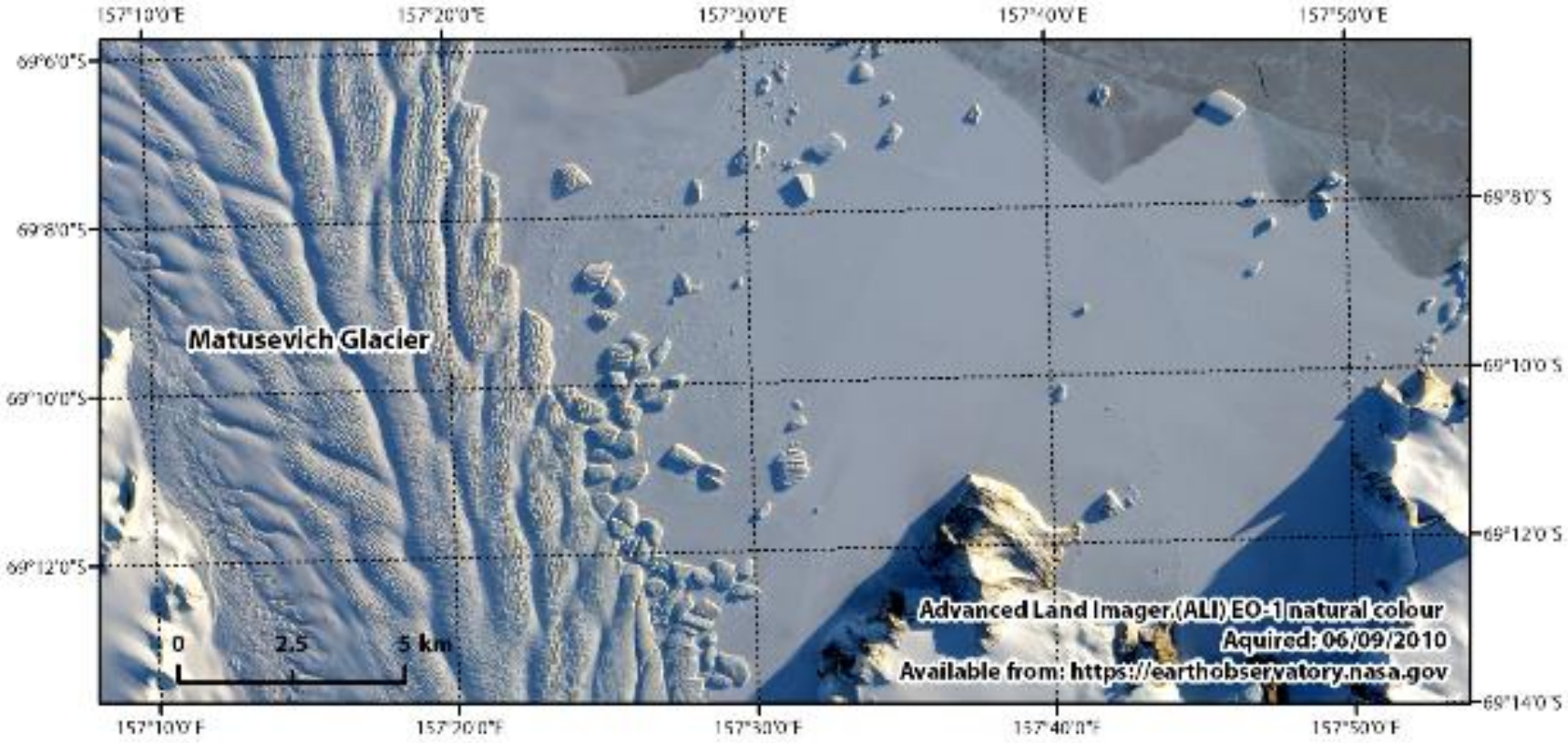

Figure 2.4) The Matusevich Glacier, Antarctica. Large calving events occur where pre-existing lines of weakness have been introduced by crevasse patterns.

2.2.3 Drivers of lacustrine calving

i) Longitudinal stretching

Longitudinal stretching is the downstream stretching of glacier ice and the opening of crevasses transverse to flow. Longitudinal stretching occurs in response to increased velocities towards the terminus (Benn *et al.*, 2007b). Calving events occur where pre-existing lines of weakness have been introduced by crevassing (Figure 2.4), largely due to longitudinal stretching at the terminus.

ii) Meltwater-driven fracture propagation

Meltwater-driven fracture propagation has been identified as a key driver of disintegration calving on the ice shelf scale. Repeated rapid fracturing creates narrow ice-cliff-parallel blocks which subsequently topple and fragment (Scambos *et al.*, 2009). The presence of surface or near-surface meltwater has been shown to pre-condition this disintegration style of calving, as with the Larsen Ice Shelf (Scambos *et al.*, 2000), but hydro-fracture acts as key mechanism for this calving process when water drains into crevasses and increases pressure upon the fracture tip (Benn *et al.*, 2007b). Meltwater-driven fracture propagation has also been suggested as a control for larger scale calving activity near the terminus of lacustrine calving glaciers, where the addition of meltwater to surface crevasses causes fractures to penetrate deeper in the ice column, in some cases to full thickness (Figure 2.5; Benn *et al.*, 2007b). However, recent observations of calving at tidewater glaciers have shown that fractures do not always contain water prior to calving which suggests that meltwater-driven fracture propagation should not be assumed to be a universal driver of calving (Petlicki *et al.*, 2015).

iii) Steep stress gradients

Cryostatic pressure increases down through the ice column (Figure 2.6). For the subaerial portion of the ice cliff, the outward cryostatic pressure is largely unopposed by atmospheric pressure, which results in large tensile stresses, particularly at the waterline of tall subaerial ice cliffs (Hanson & Hooke, 2003). Reeh (1968) and Hughes (1998; 2002) envisaged that calving is a cyclical process, whereby unbalanced stresses cause calving through geometric changes, which then reinstates unbalanced forces at the new marginal cliff and so on.

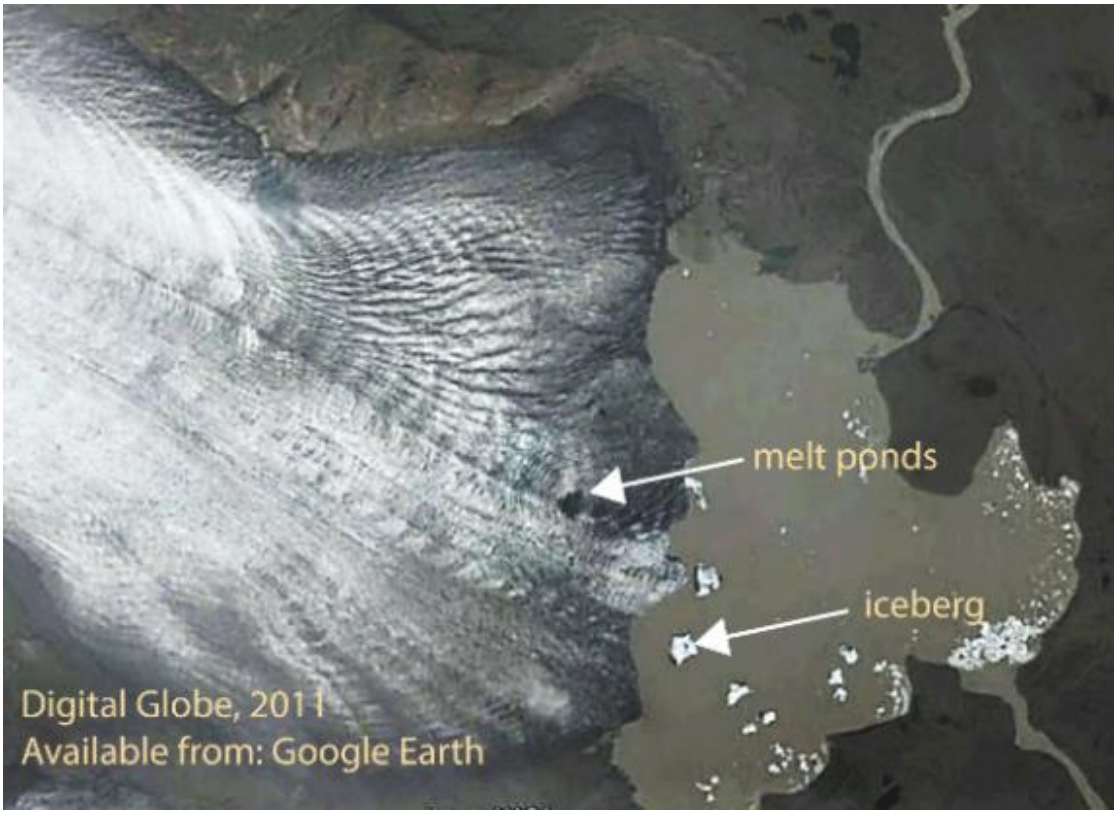

Figure 2.5) Surface meltwater ponds and fills crevasses on the surface of Fjallsjökull in 2011. In 2012 a large calving event took place which stepped the terminus back to this area of meltwater accumulation. Volcanic dust present on the surface of the glacier after 2010 Eyjafjallajökull eruption could have also played a role in enhancing surface melt.

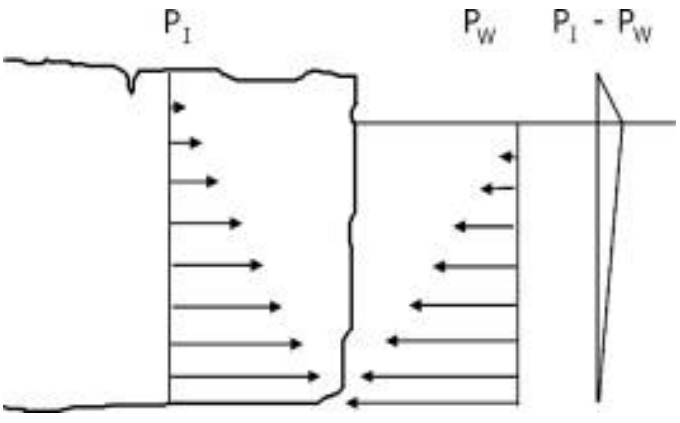

Figure 2.6) Schematic of the forces present at an ice cliff, with opposing outward-directed cryostatic (P_I) and backward-directed hydrostatic forces (P_W). The net outward-directed force is shown by the triangle and is equal to $P_I - P_W$ (Benn *et al.*, 2007b, p. 149 https://doi.org/10.1016/j.earscirev.2007.02.002).

iv) Buoyant forces

Force imbalances are present in the termini of calving glaciers and ice shelves (Reeh, 1968). Buoyant forces (Figure 2.7) have been suggested to trigger lacustrine calving from observations in Patagonia (Warren *et al.*, 2001), Alaska (Lingle *et al.*, 1993; Boyce *et al.*, 2007), Norway (Theakstone & Knudsen, 1986; Theakstone, 1989), Arctic Canada (Holdsworth, 1973), and Iceland (Howarth & Price, 1969). Imbalanced hydrostatic stresses at calving termini which reach flotation impose an upward-bending moment which leads to buoyancy driven calving (Warren *et al.*, 2001; James *et al.*, 2014). At Glacier Nef, Patagonia, buoyancy driven calving was observed to lead to high magnitude, low frequency calving (Warren *et al.*, 2001). No observational evidence for basal crevassing at lacustrine calving glaciers has been published; however, there is no plausible reason why basal crevassing would not occur, if buoyant forces were great enough to cause upward bending at the terminus.

v) Melting at or below the waterline and the development of a waterline notch

Subaqueous melt rates can commonly exceed that of subaerial melt rates for tidewater glaciers (Bartholomaus *et al.*, 2015; Sugiyama *et al.*, 2016). Less is known about rates of subaqueous melt for lacustrine glaciers, and the thermal structure of lakes is distinct from typical fjords (Figure 2.8; Sugiyama *et al.*, 2016). Research on proglacial lakes in Patagonia has found that wind-driven circulation conveys heat to the calving front, but cold glacial water fills the regions near the lake bottom, resulting in no efficient heat transfer to the deeper part of the ice-water interface (Sugiyama *et al.*, 2016). In contrast to tidewater glaciers, upwelling plumes are not observed at lacustrine glaciers, most likely because highly turbid subglacial meltwater is denser than lake water and stays near the lake bottom (Sugiyama *et al.*, 2016). Sugiyama *et al.'s* (2016) research highlights the need for further detailed investigations of the processes that occur at the ice-water boundary, in order to more accurately understand frontal ablation in freshwater calving glaciers.

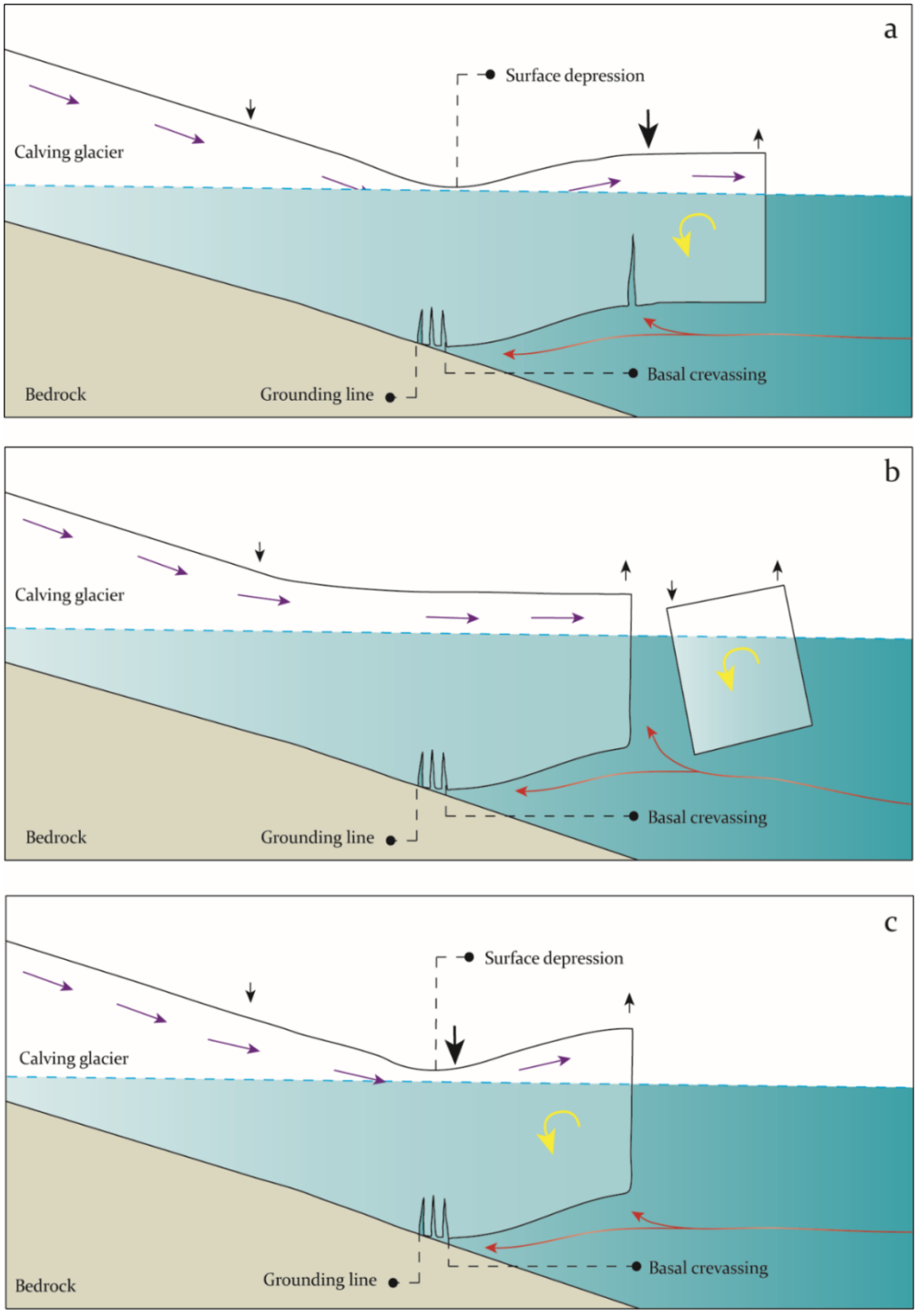

Figure 2.7) A floating terminus on a sloped bed where buoyant forces cause isostasy-driven upward deflection of the terminus coupled with a surface depression at the grounding line (Modified from: Murray *et al.*, 2015b, p. 977 CC BY-NC-ND 4.0 https://creativecommons.org/licenses/by-nc-nd/4.0/legalcode). a) Buoyant flexure which is being driven by an imbalance of forces at the terminal margin (black arrows) causing basal crevassing observed in b); c) Basal crevasse propagation can result in successional calving events and retreat to the surface depression (where the grounding line is also hypothesised to be located). Red arrows indicate warm water which is drawn into basal crevasses by rotation (yellow arrow) of the flexion zone causing enhanced rates of melt.

Warm water at the ice-water interface (Sugiyama *et al.*, 2016) can thermally erode a notch at the waterline of a glacier ice cliff, and this has been suggested as a driver of calving at the termini of lacustrine calving glaciers in Patagonia and New Zealand (Warren *et al.*, 2001; Kirkbride & Warren, 1997). Calving cycles have been suggested to operate at some glaciers in New Zealand (Robertson *et al.*, 2012; Kirkbride & Warren, 1997); beginning with waterline melting and the collapse of the roof of a sub-horizontal notch at the cliff foot. This melting process can progressively undercut the termini of calving glaciers, and cause calving by the fracturing and toppling of overhanging blocks (Iken, 1977; Haresign & Warren, 2005). A constant lake level is important in the development of a waterline notch, with fluctuations in lake level more than 0.15 m over 24 hours enough to significantly retard the development of thermal notches on Tasman Glacier (Röhl, 2006).

vi) Calving of submerged 'ice feet'

Submarine ice feet, or ramps, are transient features and have been observed to extend up to 500 m underwater from the subaerial glacier termini of some glaciers (Figure 2.9; Robertson *et al.*, 2012). Submarine ice feet form due to proportionally higher melt rates nearer the water surface (Sugiyama *et al.*, 2016; Wagner *et al.*, 2016) which leaves an unsupported ice overburden. This overhang eventually collapses, leaving behind a submerged protrusion (Benn *et al.*, 2007b; Wagner *et al.*, 2016; Robertson *et al.*, 2012).

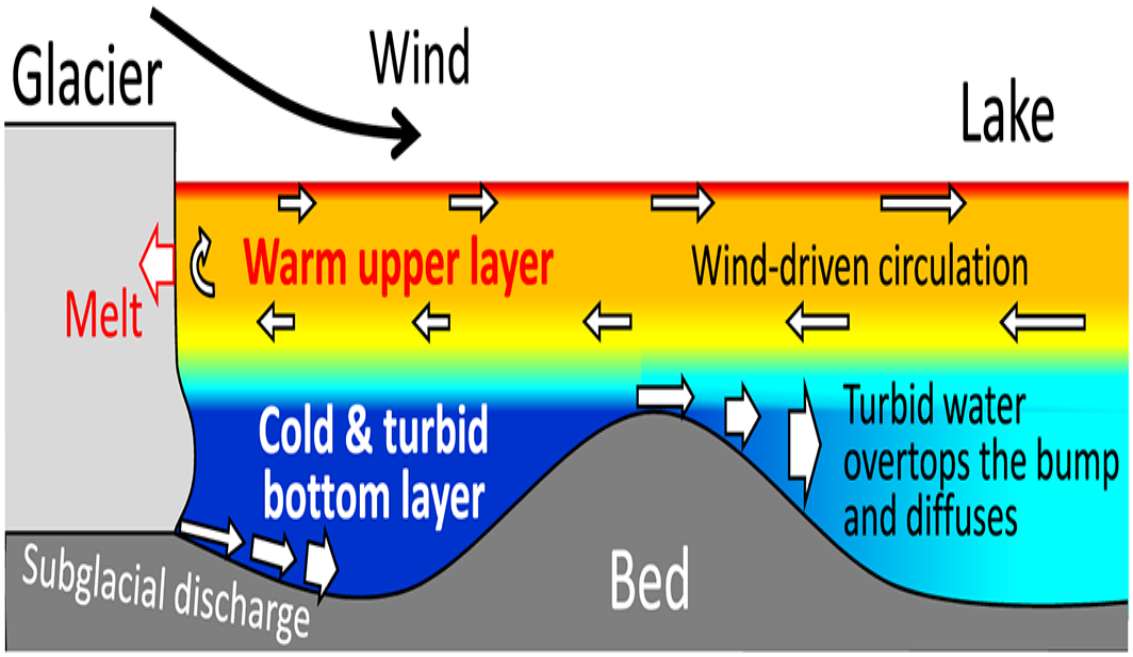

Figure 2.8) Thermal structure of a proglacial lake in Patagonia (Sugiyama *et al.*, 2016, p.2284 CC BY-NC-ND 4.0 https://creativecommons.org/licenses/by-nc-nd/4.0/legalcode).

Robertson *et al.*(2012) suggested that the development and maintenance of these ice ramps is controlled by a cyclic calving pattern, relatively stable lake level and the debris cover. Wagner *et al* (2016) suggested that subaqueous ice protrusions at the glacier front may provide additional buoyant forces at the terminus which can trigger calving.

2.2.4 A hierarchy of calving processes

Benn *et al* (2007b) provide a useful hierarchical summary of calving processes in order to define their relative importance to calving. In this hierarchy, each calving process is defined as either a first-, second-, or third-order process (Figure 2.10). This hierarchy provides a useful method to categorise the key drivers acting on calving glaciers, but with the noted caveat that for different environments, for example, where longitudinal stress rates are low, other processes may act as a dominant control for particular margins.

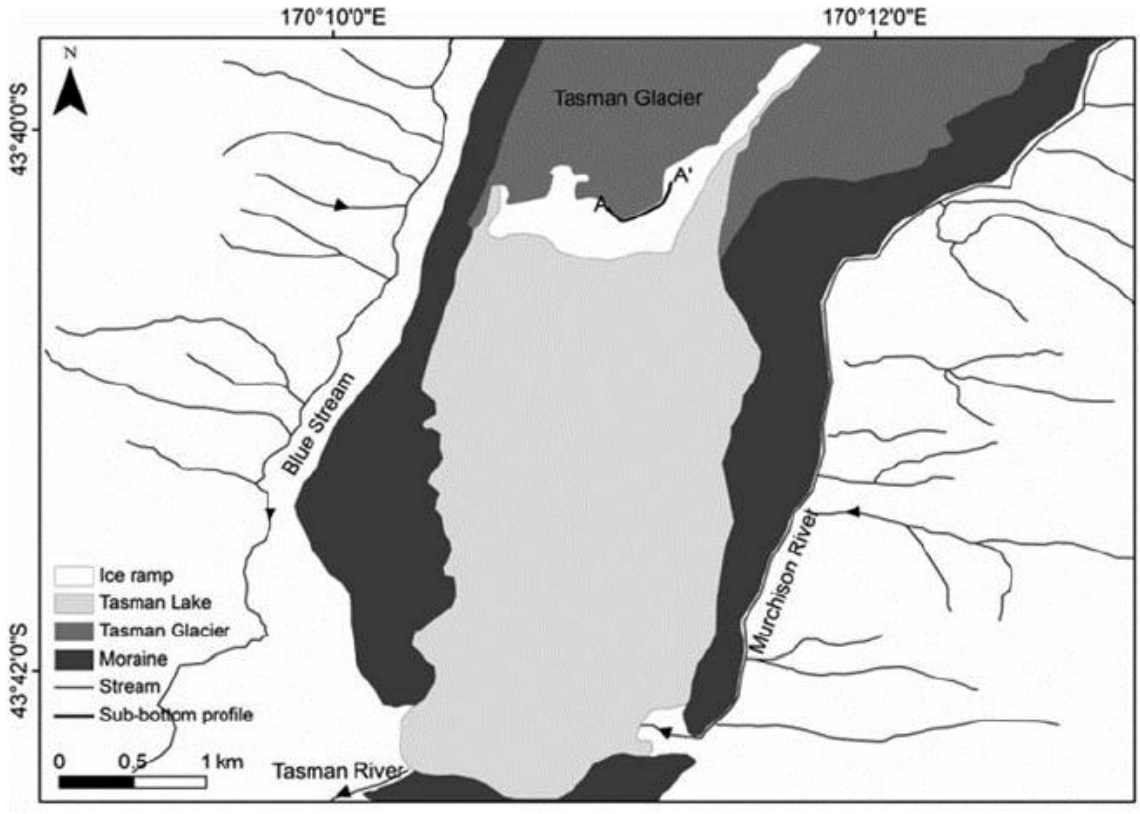

Figure 2.9) The subaqueous terminus morphology of Tasman Lake in 2008 (from: Robertson *et al.*, 2012, p.1044 reprinted from the Journal of Glaciology with permission of the International Glaciological Society). The white area protruding into the lake is an underwater ice ramp which reaches up to approximately 500 m out from the subaerial glacier terminus.

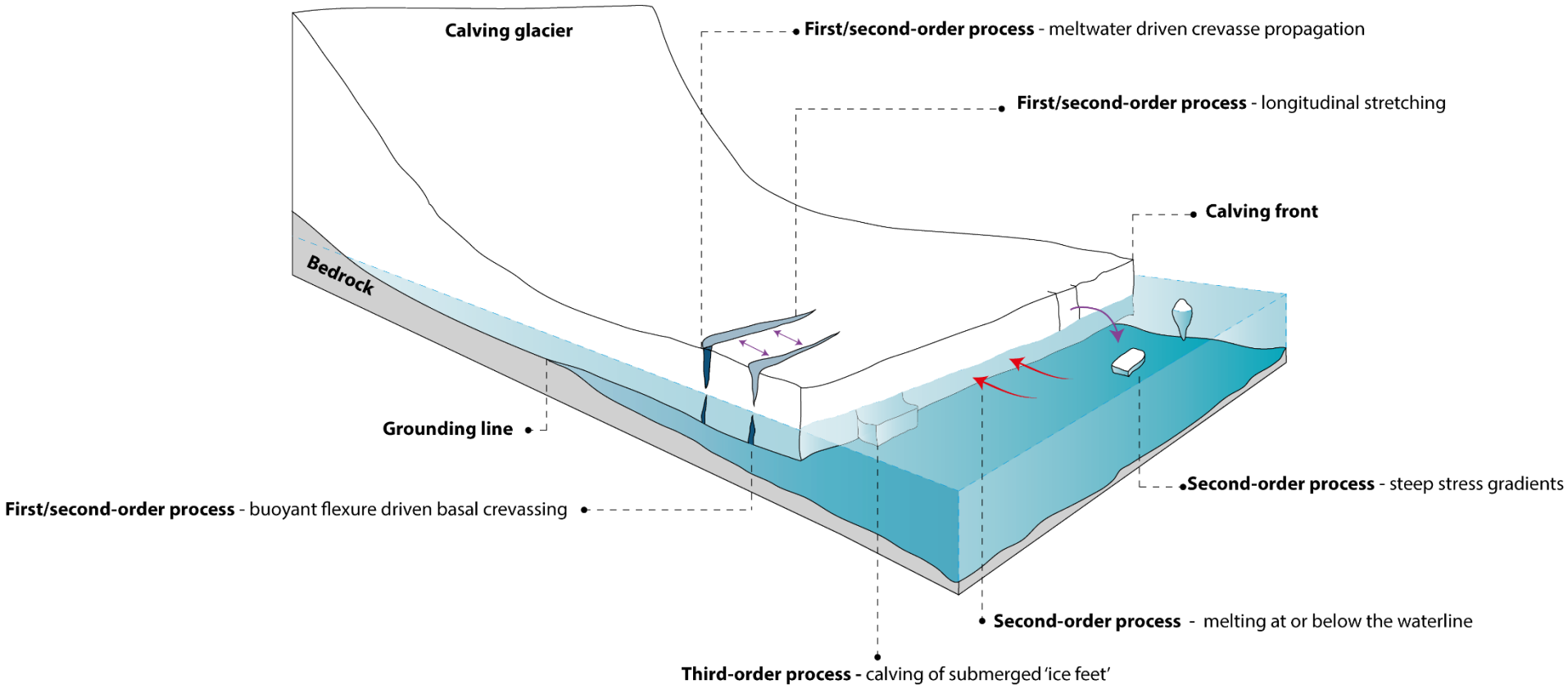

Figure 2.10) A schematic diagram illustrating some of the key mechanisms of calving in relation to the hierarchy proposed by Benn *et al* (2007b).

2.3 Calving laws, criterions, and the modelling of realistic calving events

Numerical models are used to make quantitative predictions about the future of glaciers and constrain the changes that might occur, such as: sea level rise, retreat over time, dynamic feedback and thresholds. Incorporating calving into glacier models has been challenging (Moore *et al.*, 2013), but essentially, all numerical models need a mechanism for removing mass from the terminus in line with observations (Bassis, 2011). The majority of the laws and criterion which are applied in calving models are based on tidewater glaciers, and when they do consider lacustrine calving they use a number of assumptions which given recent advancements in understanding the physical environments at the lake-ice interface (Sugiyama *et al.*, 2016; Robertson *et al.*, 2012), may not be appropriate to produce realistic results. The ongoing pursuit of a universal calving law (e.g. Bassis, 2011) has led to the development of models which reproduce calving with varying levels of success (Cuffey & Paterson, 2010).

Given the diversity of calving environments, especially the difference between lacustrine, tidewater glaciers and ice shelves, in addition to the conditions at each individual glacier, and the presence of transient features such as subaqueous ice ramps, the search for one unifying law could be an elusive goal (Benn *et al.*, 2007b; Van der Veen, 2013) particularly for lacustrine glaciers, for which there are less observations and subsequent research. Models which do exist tend to be based around larger-scale calving events (Bassis, 2011; Nick *et al.*, 2010; Benn *et al.*, 2007b) or on parameterising an average (Van der Veen, 1996; O'Neel, 2000). This is largely because modelling glacier behaviour at the fracture level requires more computational power (Bassis, 2011). Recent models which have applied supercomputing resources to the problem have produced realistic distributions of calving fragments based on fundamental elastic deformation, granular flow, and viscotic cohesion (Åström *et al.*, 2014, 2013). However, the resolution of many models still does not include small ice cliff failure (Moore *et al.*, 2013; Cuffey & Paterson, 2010).

Attempts to include calving in glacier models have been approached from two distinct groups; the 'calving laws', which aim to model calving as a continuous process using calving rates, and the 'calving criterion', which use a defined set of conditions that when met, will initiate calving at some point in time (O'Leary, 2012).

2.3.1 Fundamental calving laws

i. Calving rate

The calving rate (Equation 1) is the difference between ice velocity at the glacier terminus and glacier length change over time. This equation provides a foundation for most calving laws. These laws can be tuned to fit particular glaciers or groups of glaciers and are usually empirical or semi-empirical (Benn & Evans, 2010). Where U_c is the calving rate, $\overline{U}_t$ is the vertically averaged glacier velocity, L is glacier length and t is time. This equation shows that calving losses are closely linked to the rate of ice delivery to the glacier terminus, but can be viewed in two different ways (the aforementioned 'master and 'slave' hypotheses) which has produced two different branches of calving laws (O'Leary, 2011).

Equation 1

$$U_c = \overline{U}_t - \frac{\delta L}{\delta t}$$

ii. Water-depth

The water-depth calving laws describe the relationship between calving rate and water depth. Observations have shown that as a glacier advances into deeper water it becomes more buoyant and calves at a faster rate (Brown *et al.*, 1982; Pelto & Warren, 1991). A linear relationship is displayed for this relationship in some cases where the individual glacier is stable (Brown, Meier and Post, 1982), or only slowly advancing or retreating (Vieli *et al.*, 2001). Equation 2 is an example of a simple water-depth law whereby a and b are empirically determined coefficients and Dw is the width-averaged water depth. Both a and b have been found to be consistently smaller for freshwater glaciers than tidewater glaciers in analogous settings (e.g. Funk & Röthlisberger, 1989; Rott *et al.*, 1998; Skvarca *et al.*, 2002)

Equation 2

$$U_c = a + b\, D_w$$

2.3.2 Calving criterion

i. Height-above-buoyancy

The height above buoyancy criterion was first described by Sikonia (1982). When applied to numerical models (e.g. Van der Veen, 1996), the position of the terminus is determined by the local water depth and ice thickness, in contrast to earlier models where the calving rate (Equation 1) is linked to these parameters (Van der Veen, 2013). Through calving and dynamical changes, the glacier front has been observed to maintain a critical value above buoyancy (Van der Veen, 1996). Time-evolving glacier models which incorporate the height-above-buoyancy criterion have successfully reproduced the macroscopic behaviour of calving glaciers (Vieli *et al.*, 2001, 2000; Nick *et al.*, 2007). However when the height-above buoyancy criterion is applied in singularity (e.g. Van der Veen, 1996), modelled glacier behaviour is not realistic (Benn *et al.*, 2007a) because it prohibits the formation of ice shelves and floating ice tongues which have been observed to occur in nature with Columbia Glacier and Yakatut Glacier (Figure 2.2; Walter *et al.*, 2010; Trüssel *et al.*, 2013). Models produce such results because the terminus position is always assumed to be at a location where flotation has not been reached (Benn *et al.*, 2007a)

ii. Crevasse depth

The crevasse depth criterion was first proposed by Benn *et al.*, (2007a) in response to the limitations of the height-above-buoyancy criterion, which prohibits the formation of ice shelves and floating ice tongues. The crevasse depth criterion is based on the downward propagation of surface crevasses, whereby, calving occurs when surface crevasses reach the water level of the lake, fjord or ocean which the glacier is terminating into. Nick *et al.* (2010) proposed the addition of basal crevassing to models using the crevasse depth criterion, positing that calving will occur when basal crevasses and surface crevasses reach the same depth within the ice.

2.3.3 The application of laws and criterion in models of calving

When applied to numerical models, calving laws and criterion reproduce observed calving with varying levels of success. One of the earliest models of calving behaviour showed that force imbalances exist near the terminus of floating glaciers and ice shelves; however, this model did not extend to grounded glaciers, and most lacustrine glaciers are grounded (Reeh, 1968). Furthermore, very rough approximations were made, the most severe being the assumption that the viscosity of glacier ice is constant (Reeh, 1968). Reeh's early work did show, however, that the magnitude of the icebergs as well as the frequency of calving is a function of glacier thickness, density, and temperature. Further progress was made by Weertman (1973), who modelled the conditions required for a single fracture to propagate through the full ice column and initiate calving. Weertman (1973) suggested that an isolated water filled crevasse could theoretically reach an unlimited depth within glacier ice, but in nature this was an apparent rarity. Early models such as this only included mode 1 failures (Figure 2.3) which impacted how well they simulated calving. Some later models began to consider other modes including Schulson & Hibler (1991) and van der Veen (1999), which did improve the modelled results.

Investigations revolving largely around the tidewater Columbia Glacier dataset, led to the development of the water depth relation (Brown *et al.*, 1982; Equation 2). In general there is a similar relationship between water depth and calving rate for lacustrine calving glaciers, except that they are typically an order of magnitude less than their tidewater counterparts (Funk & Röthlisberger, 1989). However, for both calving regimes, when the water-depth criterion was applied to models, this could only reproduce annually-averaged calving rates, and broke down when seasonal calving rates were considered (Sikonia, 1982; Meier, 1997; Krimmel, 1997). Further debate around the water-depth model is put forward by Van der Veen (1996; 2002; 2013), who suggests that the linear correlation between glacier speed and calving rate observed during Columbia Glacier's rapid retreat between 1984 and 1989 casts doubt on the water-depth model. It is worth highlighting that caution should be taken when interpreting correlations to be causal in this way, and therefore discounting relations which hold under certain conditions (e.g. Brown, Meier & Post, 1982), because calving regimes are diverse and can adjust over time. For example, O'Neel *et al.* (2003) discovered through short-term measurements of between 2 to 8 hours over a 30-day period that this correlation between calving rate and ice speed breaks down, forming part of the basis for this study.

Van der Veen (1996) suggested a different mechanism for calving, based again on the Columbia Glacier dataset. He argued that when the terminal thickness of a glacier reaches a critical value in excess of flotation, calving will occur. Vieli *et al.* (2001), through flowline modelling of calving at Hansbreen, Svalbard, introduced a modification, whereby the minimum height above buoyancy is replaced by a fraction of the flotation thickness at the terminus (Van der Veen, 2013). Following on from Vieli *et al.* (2001), Nick *et al.* (2007) employed a similar flowline model to simulate the advance and retreat of Columbia Glacier which implemented both the height-above-buoyancy and the water-depth calving criterion, with both yielding similar glacier behaviour. To overcome the limiting factors of the height-above-buoyancy criterion (see Section 2.3.2), Benn *et al.* (2007a) introduced a calving criterion which predicts calving where the depth of surface crevasses equal the ice height above sea level, in cases where longitudinal stretching is a first-order mechanism.

Nick *et al.* (2010) expanded on this crevasse-depth model to include basal crevassing, and work by James *et al.* (2014) and Wagner *et al.* (2016) has also incorporated the buoyant flexure component. The approach of using fracture mechanics to model calving, pioneered by Weertman (1973) has been revisited by Åström *et al.* (2014) in their 3D model, where the authors describe calving behaviour as a self-organised critical system. The IPCC (Vaughan *et al.*, 2013) also identify that recently, more realistic models have been developed allowing the

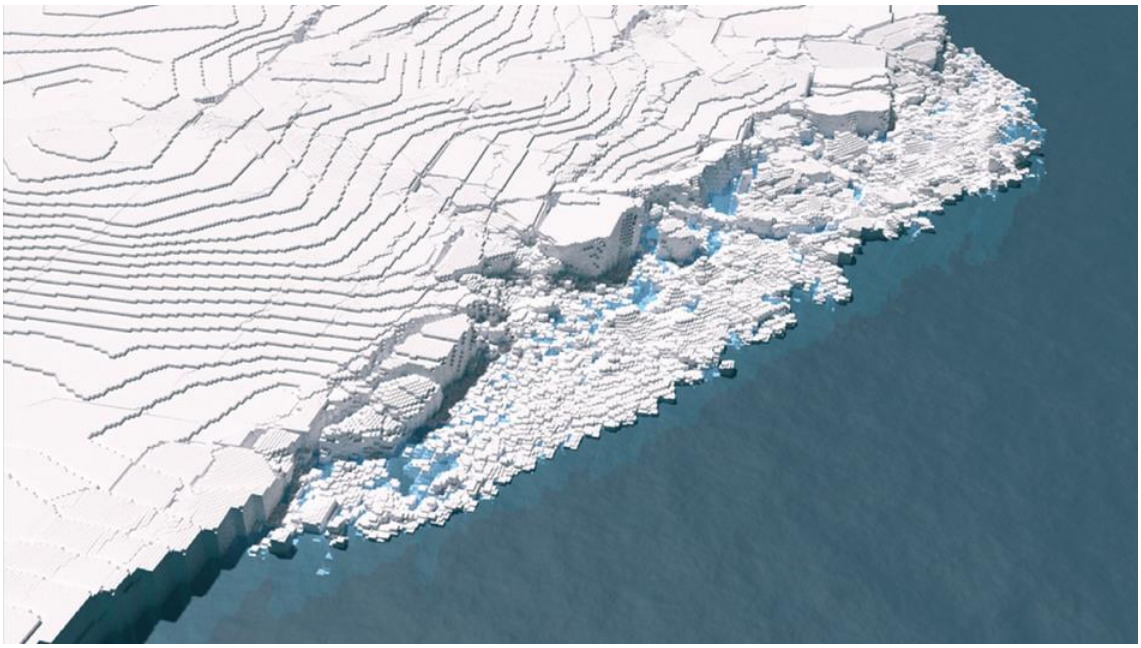

Figure 2.11) The geometry of Kronebreen, Svalbard, implemented in an example of a new generation of particle models (Åström *et al.*, 2014, p.87 doi:10.1038/ngeo2290).

dependence of calving and climate to be explicitly investigated (Norman *et al.*, 2013; Vaughan *et al.*, 2013).

Determining a calving law which can be applied to all glaciological and environmental regimes remains a persistent problem in glaciology (Bassis, 2011). Although it would be very convenient to group the mechanisms of calving in terms of their relative importance (Benn *et al.*, 2007b) this has not proved to show realistic results when longitudinal strain is not the sole driving mechanism. Recently-developed fracture level models (Figure 2.11) which focus on tidewater glaciers and ice shelves (e.g. Åström *et al.*, 2013, 2014; Chapuis & Tetzlaff, 2014) require further observations to constrain simulations of calving, and to model how calving behaviour responds to environmental forcing and initial conditions. The future changes which might be displayed by lacustrine glaciers have been overlooked in these models, and it is critical that the mechanisms of their retreat are also understood. Although lacustrine glaciers are apparently less sensitive to perturbations than tidewater glaciers, they have been shown to retreat rapidly after an initial climate signal (Warren *et al.*, 1995).

It is clear that iceberg calving is a multifaceted and dynamic process. The variety of mechanisms which act upon calving must therefore be considered to have mutual interplay (James *et al.*, 2014). Models are mostly based on relations obtained from tidewater glaciers, and do not simulate small-ice cliff failures very realistically (Cuffey & Paterson, 2010; Moore *et al.*, 2013). Lacustrine environments are significantly different from tidewater environments, and further evidence for why this may be the case has emerged since many of the key models were developed (Sugiyama *et al.*, 2016). Therefore, in order to aid the development of realistic models of calving at lacustrine termini, further observational data of calving behaviour at the lacustrine ice cliff scale is required.

2.4 Monitoring calving at the ice cliff

2.4.1 Monitoring discrete calving events

Many studies have observed calving dynamics in terms of calving rates (e.g. Vieli *et al.*, 2002), magnitude and frequency relationships of detachments, and their mechanisms (e.g. Kirkbride & Warren, 1997). However, these tend to be biased towards large calving events of over 10 m^3 (e.g. Bassis, 2011) and or/seasonal cycles at tidewater glaciers and ice shelves, because seasonal studies are easier to operate and tidewater glaciers have attracted more interest perhaps because they occur in greater numbers and calve directly into the sea. Lower

magnitude (<10 m^3) calving events occurring at the ice cliff, and not necessarily involving an instantaneous whole cliff failure, could be important in understanding the mechanisms of calving, and how calving does or does not relate to environmental conditions. However, these events are difficult to monitor and have therefore been largely neglected in the literature by all but a handful studies (Glowacki *et al.*, 2015; Chapuis & Tetzlaff, 2014; Petlicki *et al.*, 2015; Bartholomaus *et al.*, 2015; Kirkbride & Warren, 1997).

Many magnitude and frequency relationships which occur in the geosciences have a characteristically skewed frequency distribution of variables, where the highest frequency events occur in the low to middle magnitude range, and there are only a small proportion of high magnitude events (Wolman & Miller, 1960). Previous observations (Budd *et al.*, 1980; Orheim, 1985) may have introduced bias towards the importance of low frequency, high magnitude events because the low resolution of data used to base measurements of calving activity are not capable of capturing high frequency, low magnitude calving events.

Advances in high-resolution technologies and a reduction in costs has resulted in the recent proliferation of studies addressing the calving problem for tidewater glaciers at the single-event scale. Previous studies of calving events have been based on sporadic observations of calving events (Warren *et al.*, 1995; O'Neel *et al.*, 2003) or, in some cases, have used indirect measurements obtained from icebergs already floating in the sea (Orheim, 1985; Budd *et al.*, 1980). Studies relying on such indirect measurements will inevitably introduce error because icebergs are exposed to melting and disintegration as soon as they are calved (Chapuis & Tetzlaff, 2014). Some studies have approached the difficulties of monitoring individual calving events by using seismic detection (O'Neel *et al.*, 2010; Glowacki *et al.*, 2015; Bartholomaus *et al.*, 2015). Though passive seismic detection of calving event timings and sizes are improving in accuracy, it is at present only reliable for large-scale events (> 700 m^3) (Bartholomaus *et al.*, 2015). Chapuis & Tetzlaff (2014) used human observers to record the timing and quantity of ice detachment in conjunction with imagery taken at 3 second intervals (Figure 2.12).

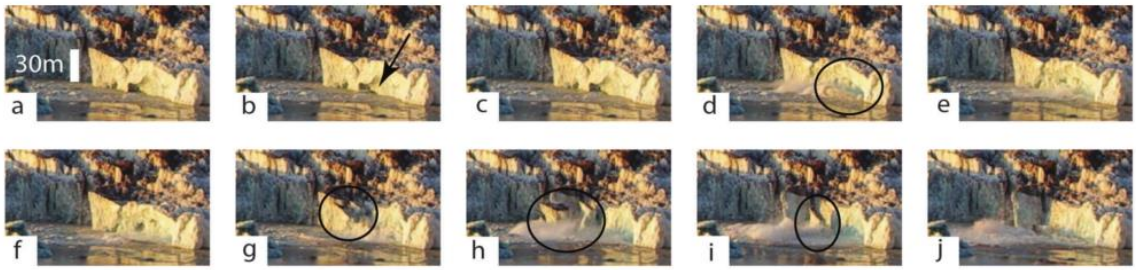

Figure 2.12) Images recording a calving event at Kronebreen, Svalbard at 3 second intervals (from: Chapuis and Tetzlaff, 2014, p.627, reprinted from the Journal of Glaciology with permission of the International Glaciological Society).

Interestingly, they were able to model calving event sizes and inter-event intervals and could statistically explain the variability in tidewater calving activity entirely as a result of mutual interplay between calving and destabilisation of the local area in the calving front.

The challenge of continuously studying change at the cliff stems from the fact that most available remotely-sensed data is limited too greatly by its resolution both spatially (e.g. Landsat 30 m) and temporally (hours to days, and longer), and the angle of data acquisition, to allow investigation at the level of individual calving events (Chapuis & Tetzlaff, 2014). Further restrictions are placed by the lack of sunlight during polar nights (Glowacki *et al.*, 2015), the hazards of collecting data at the terminus of calving ice bodies (Kohler, 2008) and the nature of study sites which are difficult to access, especially during winter (Ryan *et al.*, 2015). There is, therefore, a need to employ new methods to study these processes in order to parametrize calving (Chapuis & Tetzlaff, 2014; Petlicki *et al.*, 2015; Meier *et al.*, 2007), particularly within hourly time scales and at small magnitudes (calving events of < 100 m^3 and associated activity at the terminus) in order to quantify the total impact of calving on the ice mass budget (Vaughan *et al.*, 2013; Glowacki *et al.*, 2015). The geometric qualities and

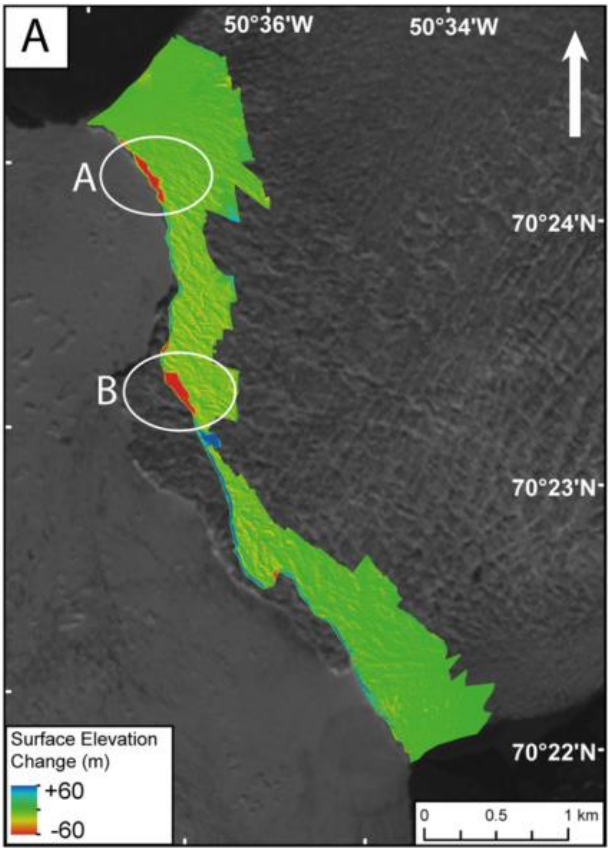

Figure 2.13) Surface elevation difference between two DEMs collected on 1 July and 2 July 2013. DEMS of Store Glacier, Greenland produced from SfM data (adapted from: Ryan *et al.*, 2015, p.4 CC BY 3.0 https://creativecommons.org/licenses/by/3.0/legalcode)

measurements of calving at the single event scale could, in theory, be monitored by repeat Structure-from-Motion (Figure 2.13; Ryan *et al.*, 2015), laser scanning (Petlicki *et al.*, 2015; Abellán *et al.,* 2015; Conforti *et al.*, 2005), or ground based radar (Chapuis *et al.*, 2010). So far however, data collected at sufficient resolutions and at high frequency intervals capable of capturing the geospatial behaviour of discrete events at the termini of lacustrine calving glaciers have not been published using these techniques (Chapuis & Tetzlaff, 2014).

The application of repeat terrestrial laser scanning is an established technique which has been used to assess temporal and spatial characteristics of the retreat of hard rock cliffs (Abellán *et al.*, 2014; Vann Jones *et al.*, 2015; Rosser *et al.*, 2005; Norman *et al.*, 2013) and has the potential to be applied to the ice cliff. So far laser scanning has been used to monitor glacial characteristics in a number of ways, but never at a sufficient temporal resolution to monitor discrete changes at the ice cliff. Conforti *et al.* (2005) demonstrated the use of terrestrial laser scanning on an ice cliff at Miage glacier, Italy. The scanning system used at the time, an Optech ILRIS-3D permitted measurements over the glacier surface with an average point spacing of 0.15 m from a distance of up to 300 m. To provide sufficient coverage of the glacier surface, 14 scans were obtained from three partially overlapped scan positions. The resulting DEMs were

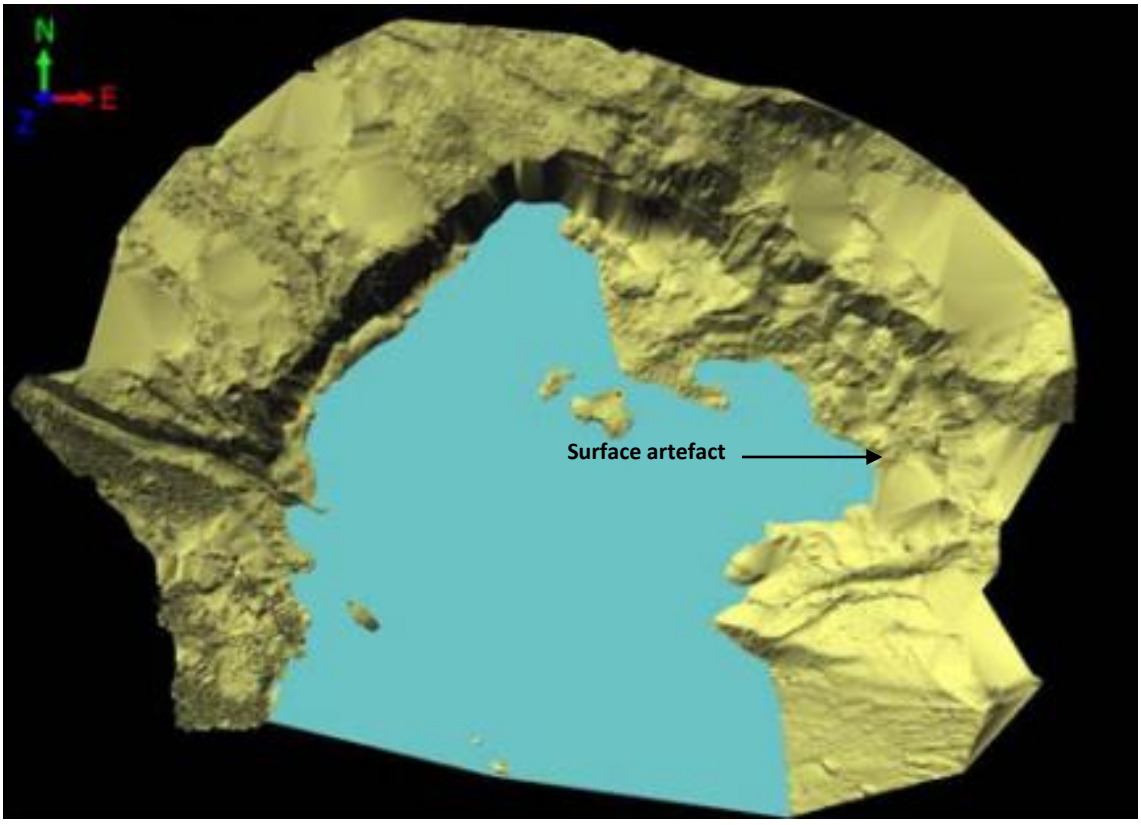

Figure 2.14) A triangulated irregular network (TIN) model of Miage Glacier (Modified from: Conforti *et al.*, 2005, p.4). Very smooth areas are likely to be areas which contain sparse data points and have been heavily interpolated.

approximately one year apart, and showed retreat at the ice cliff of c. 45 m, demonstrating the applicability of laser scanning to the monitoring of ice cliffs. However, visual analysis of the DEMs produced show that although the average point was stated to be 0.15 m, there are very smooth surface artefacts (Figure 2.14) probably arising from a low point density in these areas, and this is not something which the authors allude to. Schwalbe *et al. (*2008) used a Riegl LPM-321 terrestrial laser scanning system to successfully map surface features, track surface velocities and determine the height of a glacier front. Petlicki *et al. (*2015) used an ILRIS-LR laser scanning system to scan the ice cliff of Hansbreen, a tidewater glacier on Svalbard and monitored the development of a waterline notch and its control on calving from a distance of 250-400 m (Petlicki *et al.*, 2015). They provided two cross-sectional profiles of the ice cliff geometry prior to and after a calving event, but do not discuss the method of interpolation used to create the DEMs from which these profiles are extracted. This is important because the use of linear interpolation could give erroneous results which could be interpreted as a waterline notch due to the interpolation between different ice cliff geometries across the width of the glacier front but at the same height up cliff. Or the measurements of this area could be inaccurate due to interpolation across sparse data points which do not represent surface roughness in great enough detail. The monitoring interval which is used is also spread over a number of days, and although it does capture evidence of a calving, it could overlook the finer details of calving behaviour.

A study on Kårsaglaciären, a glacier in Sweden, was able to obtain glacier-scale 2 m resolution DEMs using a Riegl *VZ*-1000 instrument (Smith *et al.*, 2016). Further to the core aims of their study, Smith *et al.* (2016) observed surface changes associated with lacustrine calving at the terminus of the glacier (Figure 2.15). However, they did not obtain detailed cliff-normal topographic information of the ice cliff itself. Gabbud *et al.* (2015) presented a methodology for monitoring glacial properties at the hourly scale. They used an example of one of a newer generation of very-long range laser scanners (*VZ*-6000) to measure the surface melt of Glacier d'Arolla, Switzerland. The high frequency of the scanning intervals is chosen at the expense of scan coverage because it is necessary that the scanner remains in one position to acquire scans at an hourly rate. This leads to the presence of scan shadows because multiple, overlapping scan positions are not used. Although data is obtained from only one scan position, the resulting DEMs do have a good coverage, and the error which is associated with scan registration is eliminated (Gabbud *et al.*, 2015).

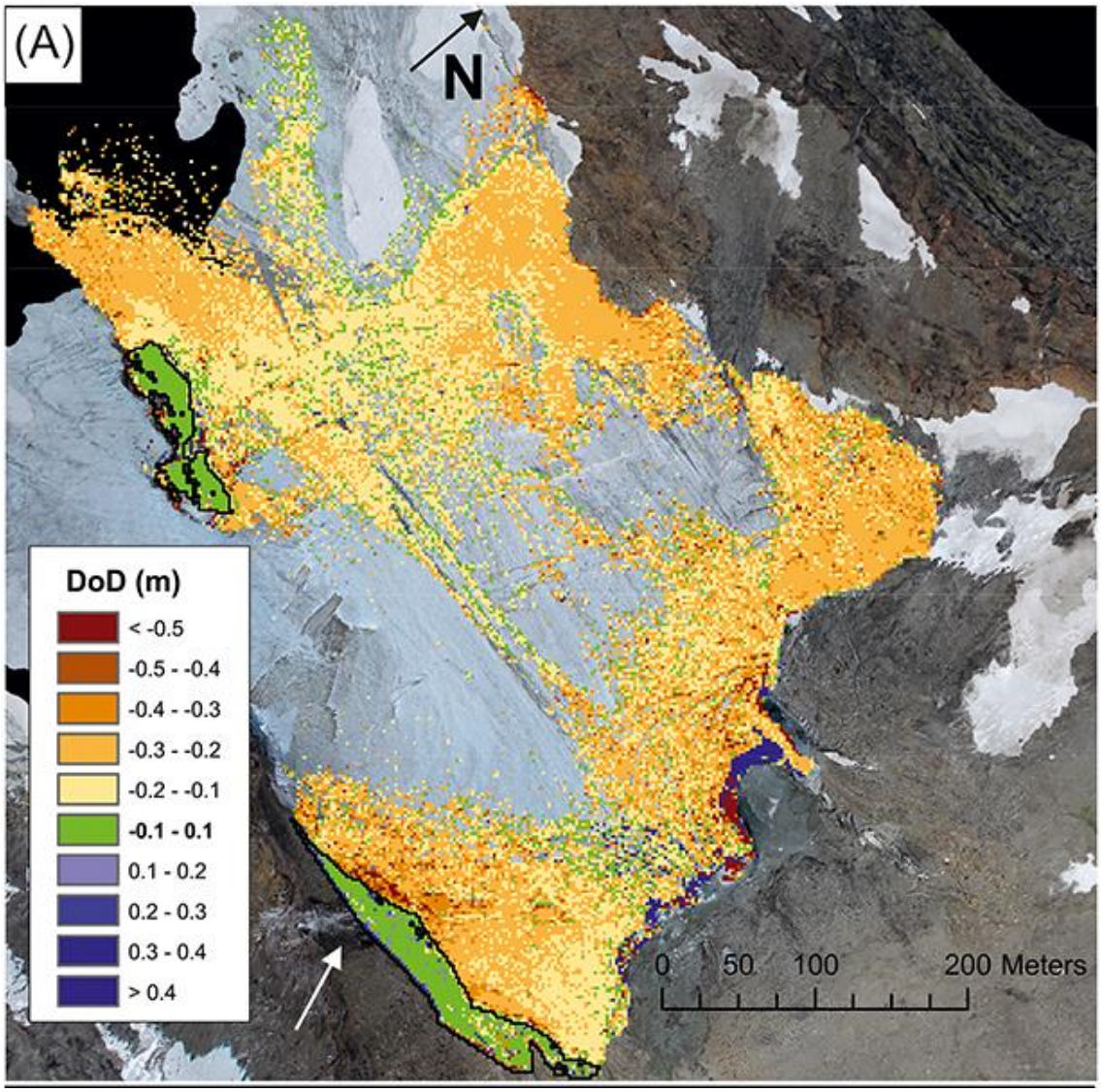

Figure 2.15) A DEM of difference from repeat TLS surveys over a 3 day interval. Bedrock areas are outlined in black. Surface changes associated with calving are observed at the glacier terminus. From: Smith *et al.*, 2016, p.759 CC BY-NC-ND 4.0 https://creativecommons.org/licenses/by-nc-nd/4.0/legalcode).

2.4.2 Environmental and time-dependent controls on lacustrine calving

It is largely assumed that calving responds to a variety of environmental variables (Cook *et al.*, 2014), such as: submarine melt and undercutting (Pętlicki *et al.*, 2015), air temperature and wind strength (Petlicki *et al.*, 2015; Wainwright, 2014), increased water in crevasses, and changes in basal water pressure. However, calving has been shown to display a non-linear response to most environmental variables (Åström *et al.*, 2014; Chapuis & Tezlaff, 2014). Calving models have been proposed which provide a level of numerical explanation for this non-linear response of glacier calving to environmental variables (Åström *et al.*, 2014; Cook *et al.*, 2014; Chapuis & Tetzlaff, 2014).

Chapuis & Tezlaff (2014) developed a simple calving model which demonstrates that for a tidewater glacier, the observed interplay between calving and terminus destabilization is sufficient on its own to explain the large variability of iceberg sizes and inter-event intervals observed in the field data. Furthermore, observations of changes in air temperature and tides do not affect the shape of the size and interval distributions obtained from the field data, which resemble power laws with long tails spanning several orders of magnitude (Chapuis & Tetzlaff, 2014). Furthermore, the authors suggested that observed calving variability is a characteristic feature of calving and not primarily the result of fluctuating external environmental factors. The size of future calving events cannot be predicted from previous events. They iterate that all magnitudes have to be expected, even under ideal stationary conditions (Chapuis & Tetzlaff, 2014). It is worth noting that studies such as this, from which relationships have been drawn (e.g. Åström *et al.*, 2014; Chapuis & Tetzlaff, 2014), use human observers to obtain information which inevitably introduces human error and subjectivity into any results, particularly in regard to the magnitude of calving events which can only be estimated using this method.

To confirm the stability criterion of such recent models, more data is needed from different calving environments, particularly lacustrine, and in different dynamical states (advance, stable, retreat). Automatic monitoring, such as continuous or near continuous terrestrial laser scanning would be highly desirable (Chapuis & Tetzlaff, 2014). Repeat 3D topographic measurements at the ice cliff would further help in unravelling the relationship between calving, internal glacier dynamics, and perturbations which may give rise to sustained calving at glacier termini. Here lies the motivation for the present study (see *Section 1.3*).

Chapter 3

Fieldsite

3.1 Identifying a suitable fieldsite

The fieldsite for this study is required to meet a number of criteria in order to address the research questions outlined in *Section 1.3*: (1) the lake-terminating glacier must be accessible with heavy equipment and have the facility to camp nearby in order to maintain the power supply to the laser scanner; (2) the glacier must have an ice cliff which is known to calve; (3) the distance between the ice cliff and the scanner position must be within the range of the laser scanner; (4) the geometry of the terminus needs to be free of obstructions to the line of sight of the scanner.

Taking these factors into account, the Vatnajökull Ice Cap, Iceland, was considered to be a suitable choice for the fieldsite. A number of Icelandic outlet glaciers from the Vatnajökull Ice Cap are presently retreating into expanding proglacial lakes. These outlet glaciers offer a natural laboratory for monitoring frontal changes of lake-terminating glaciers in high-resolution. The glacier, Fjallsjökull (Figure 3.1) was selected in particular because: ; (1) there is road access up to one kilometre away from the fieldsite; (2) the glacier has a defined ice cliff that is known to calve as evidenced from icebergs floating in the proglacial lake, visible in satellite imagery (Figure 3.1); (3) there is an elevated moraine ridge on which the laser scanner can be installed, within scanning range of the glacier terminus; (4) the geometry of the terminus is open and free of large scale obstructions.

3.2 Fjallsjökull

Fjallsjökull is a lake-terminating outlet glacier of Öræfajökull, a glacier which forms part of the Vatnajökull Ice Cap (Figure 3.1). The moraine dammed lake, Fjallsárlón, in which Fjallsjökull terminates, was first observed in aerial imagery in 1945 (Björnsson, 2017) and has been expanding since. The development of Fjallsárlón began with one narrow lake which ran parallel to the terminus, but between 2001-2009, two to three ice-marginal lakes in front of Fjallsjökull merged into one and the majority of the terminus now ends in water (Schomacker, 2010; Figure 3.2).

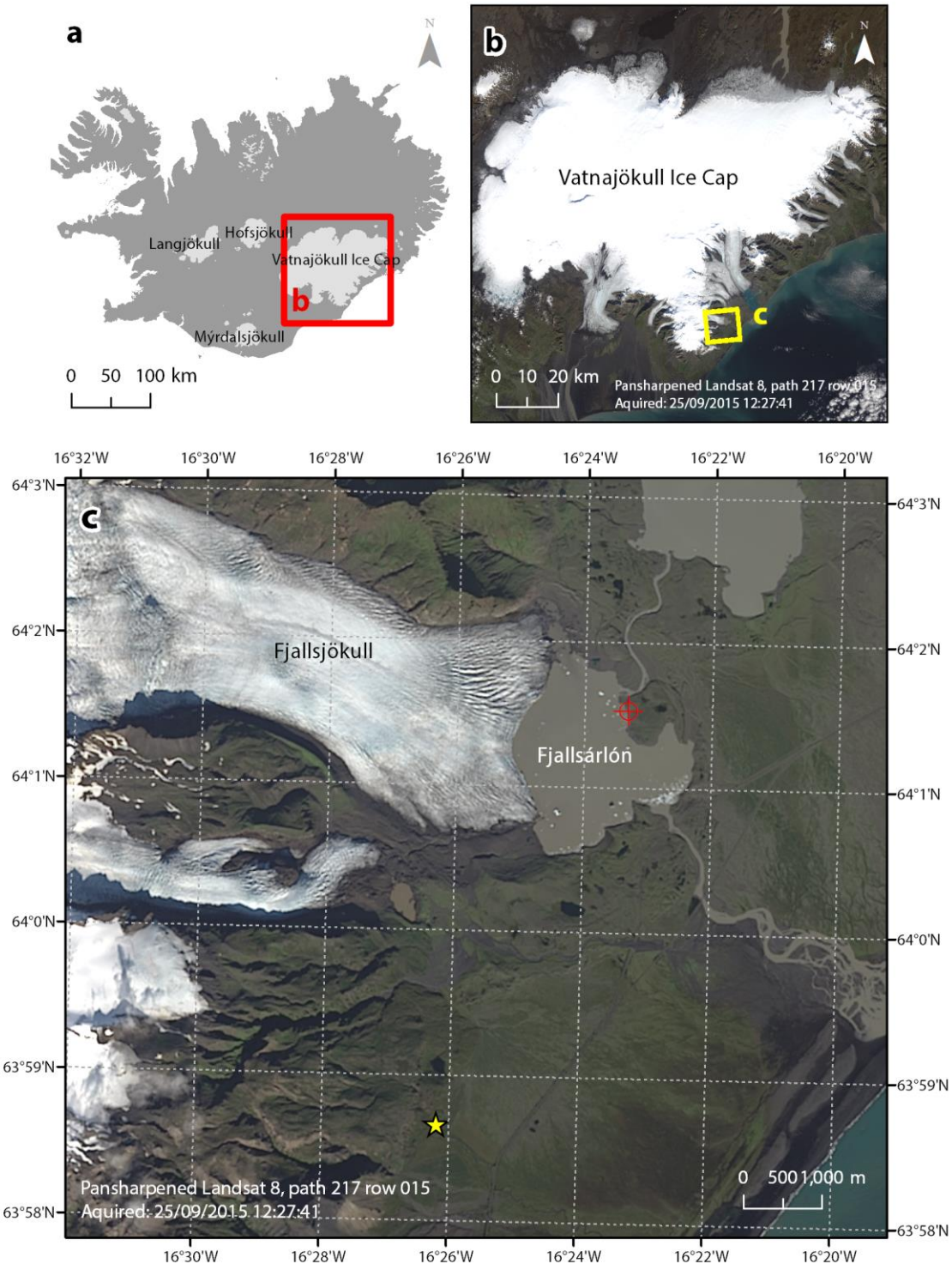

Figure 3.1) Study site maps: (a) Map of Iceland, showing glaciers and ice caps in light grey, land area in dark grey and a red box showing the extent of map (b); (b) the Vatnajökull Ice Cap, with a yellow box showing the extent of map (c); (c) Fjallsjökull, a lake- terminating outlet glacier of the Öræfajökull a glacier, Vatnajökull Ice Cap. Yellow star marks the location of Kvísker weather station and the red target marks the location of the portable weather station used in this study.

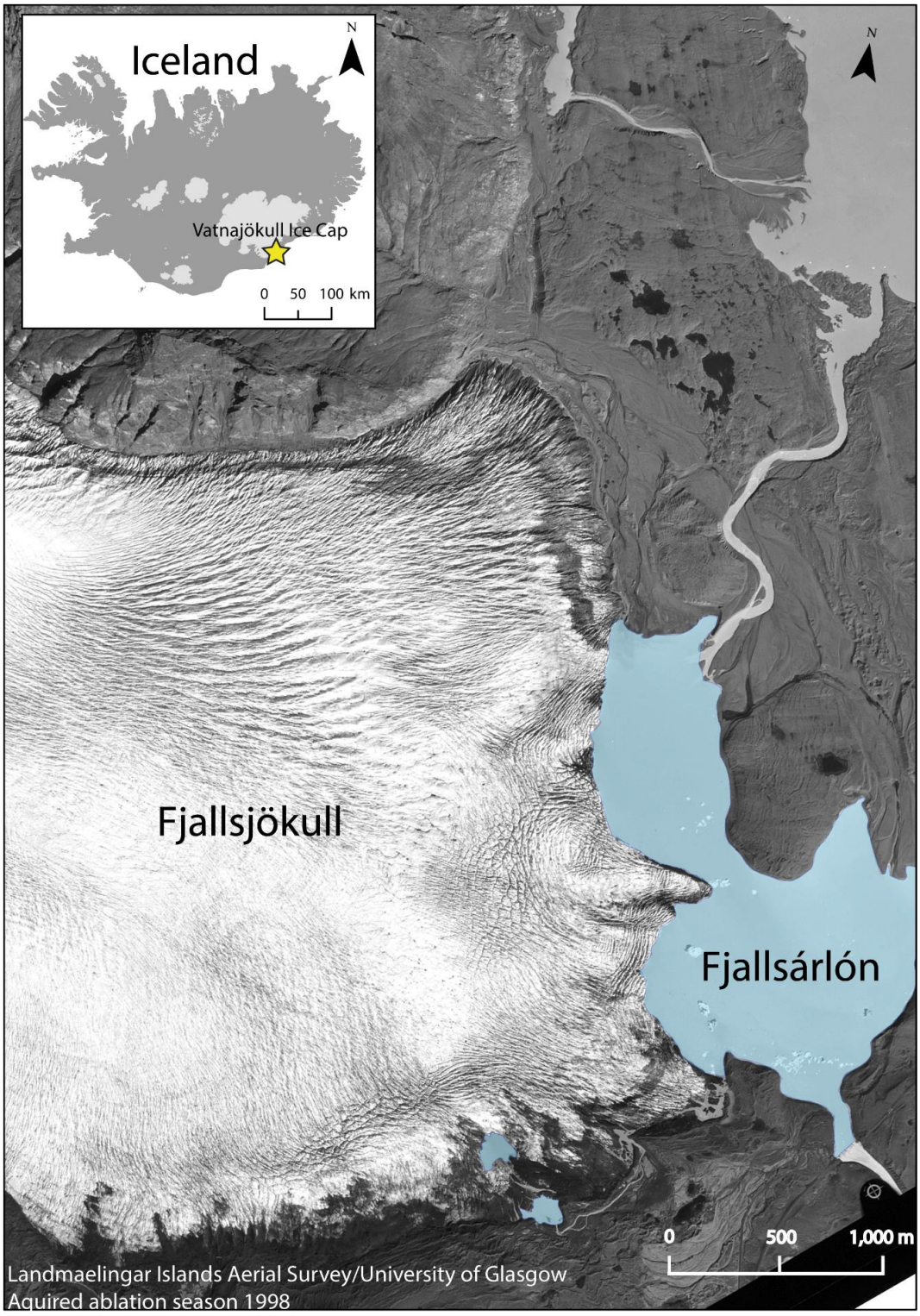

Figure 3.2) Map of Fjallsjökull and the developing ice-contact lake, Fjallsárlón in 1998 before the two, to three lakes (coloured blue for clarity), had merged between the years 2001-2009. Yellow star marks the location of Fjallsjökull in Iceland.

The glacier had a surface area of 43.7 km^2 in 2015 (as mapped from Landsat TM imagery; Figure 3.4). In 2010 the terminus elevation at the crest of the ice cliff was 20-30 m a.s.l. with an ice divide at 2030 m a.s.l., a mean slope 7.9° and an ELA of 915 ± 45 m a.s.l. (Hannesdóttir *et al.*, 2015).

The glacier geometry has been described in the past as a piedmont lobe (Evans & Twigg, 2002), but more recent satellite imagery shows that since *c.* 2015, Fjallsjökull has retreated to develop a concaved calving cliff (Figure 3.1). From field observations in 2016, the centreline of the terminus was visibly retreating into what is hypothesised to be a deeper section of water (Figure 3.3) due to the presence of intense transverse crevassing, a surface depression, and frequent calving events released from this area. No depth soundings in this part of the lake are known to exist.

3.3 Glaciers and climate change in Iceland

After the Little Ice Age (LIA), Icelandic glaciers collectively lost 22% of ice mass, contributing 0.15±0.02 mm to sea-level rise (Hannesdóttir *et al.*, 2015). By 1952 the recession of Fjallsjökull had slowed considerably and there was a period of relative stability between 1952 and 1990 (Evans & Twigg, 2002). However, since 1995 the net mass balance of Vatnajökull has been consistently negative (Figure 3.5) averaging -1.34 ± 0.12 m w.e. a^{-1} (Vaughan *et al.*, 2013; Hannesdóttir *et al.*, 2015) in line with contemporary climate change (IPCC, 2013), and many outlet glaciers of the ice cap are retreating into expanding proglacial lakes (Schomacker, 2010). Numerical models of volume and area reductions for Vatnajökull vary.

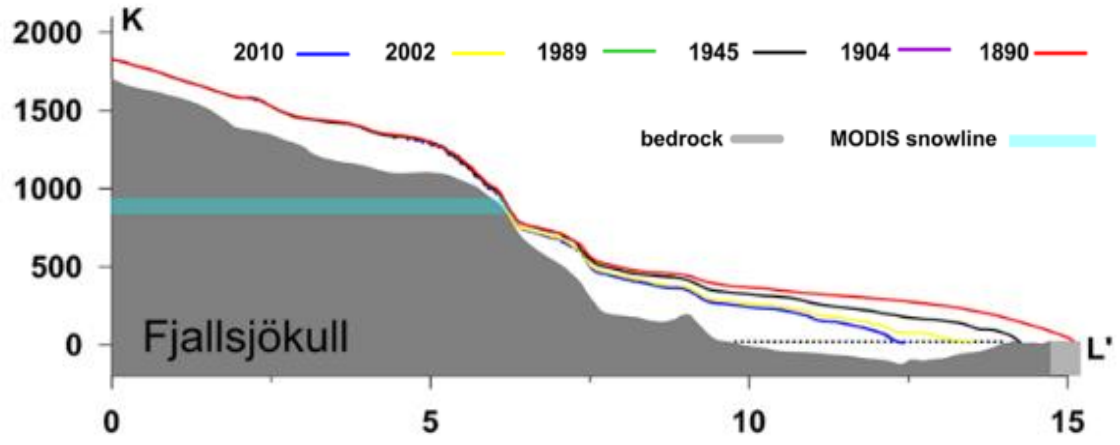

Figure 3.3) Longitudinal profiles of Fjallsjökull showing ice thickness and location of the termini at different times. *Y*-axis is in metres. The light blue horizontal line shows the average ELA derived from the MODIS images. A general pattern of retreat and thinning are observed with Fjallsjökull retreating into an over deepening forming a proglacial lake (Hannesdóttir *et al.*, 2015, p.576, CC BY 3.0 CC BY 3.0 https://creativecommons.org/licenses/by/3.0/legalcode).

Flowers *et al.* (2005) model volume reductions for Vatnajökull to be in the order of 50% within a 200 year period with a ≥2°C warming per century, but others suggest that a 25% volume reduction within the first half of this century, or even complete disappearance of the ice cap within the next 200 years is possible (Aðalgeirsdóttir *et al.*, 2006).

3.4 Summary

Fjallsjökull is an ideal study area to investigate calving processes using terrestrial laser scanning. The glacier is lake-terminating, and is readily accessible with heavy field equipment due to its proximity to the main ring road in Iceland. The ice cliff of Fjallsjökull was within the range of the Riegl VZ-4000 at the time of the survey, and the terminus geometry was free of

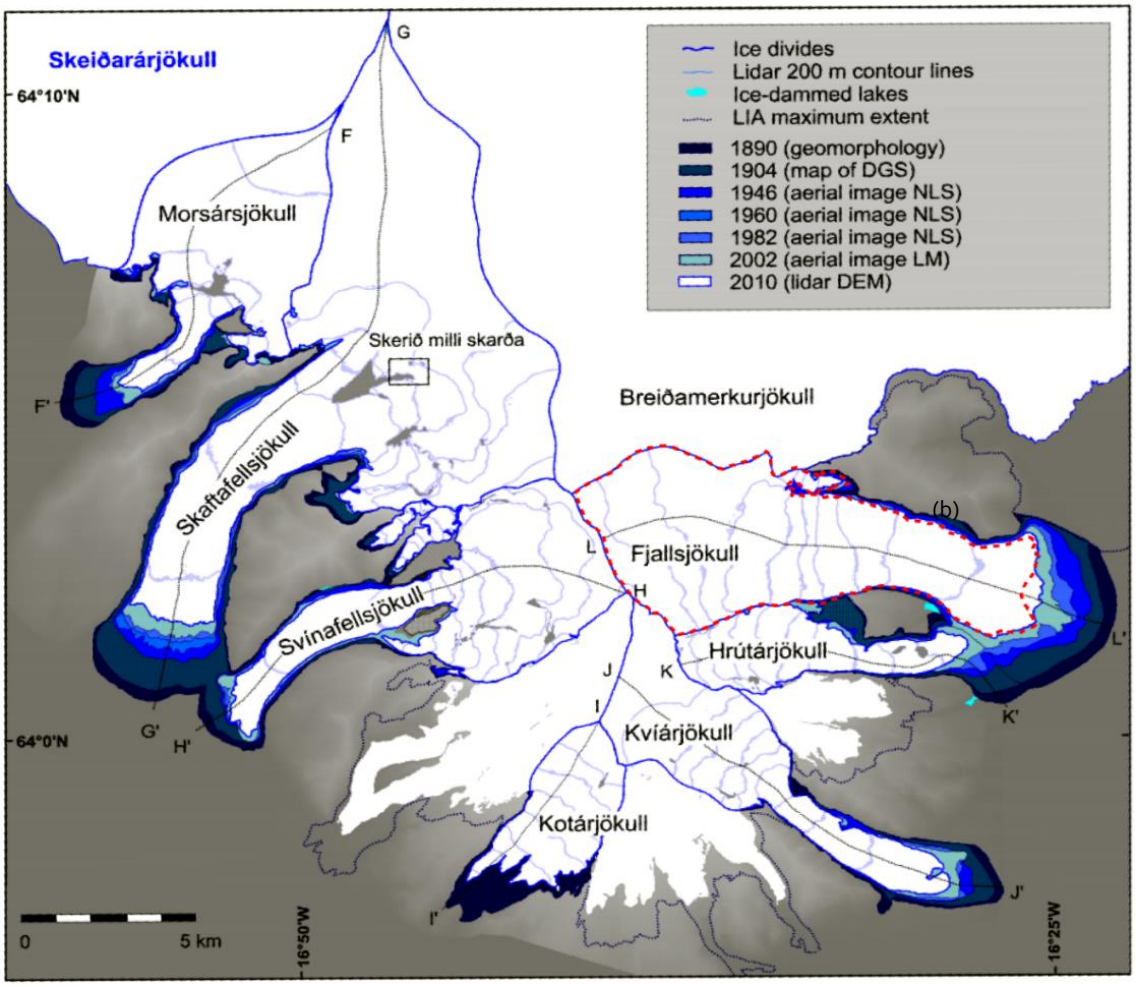

Figure 3.4) The extent of Öræfajökull's outlet glaciers at different times (modified: Hannesdóttir *et al.*, 2015, p.574 CC BY 3.0 CC BY 3.0 https://creativecommons.org/licenses/by/3.0/legalcode). The red dashed line overlays Hannesdóttir *et al* (2015) data and is the extent of Fjallsjökull mapped from Landsat data for the 25th September 2015. The ice extent in 1904 is uncertain in the mountains surrounding Skaftafellsjökull, due to distorted topography on the DGS map. DGS: Danish General Staff, NLS = National Land Survey of Iceland, LM: Loftmyndir.

major obstructions to the line of sight of the scanner. Although lake-terminating glaciers calve at an order of magnitude less than marine-terminating glaciers (Benn *et al.*, 2007b), it was deemed quite likely that at least one calving event would be observed during the course of the survey due to the number of icebergs which are visible in satellite imagery (Figure 3.1), and the rapid rate at which the glacier has been retreating via calving since the late 1990s (Schomacker, 2010). Furthermore, due to the high spatiotemporal resolution which was applied in this study, there is the potential to study processes at the single event scale at a level of detail which has not been possible in previous studies without the influence of external perturbations such as tidal forcing, waves and sea ice buttressing.

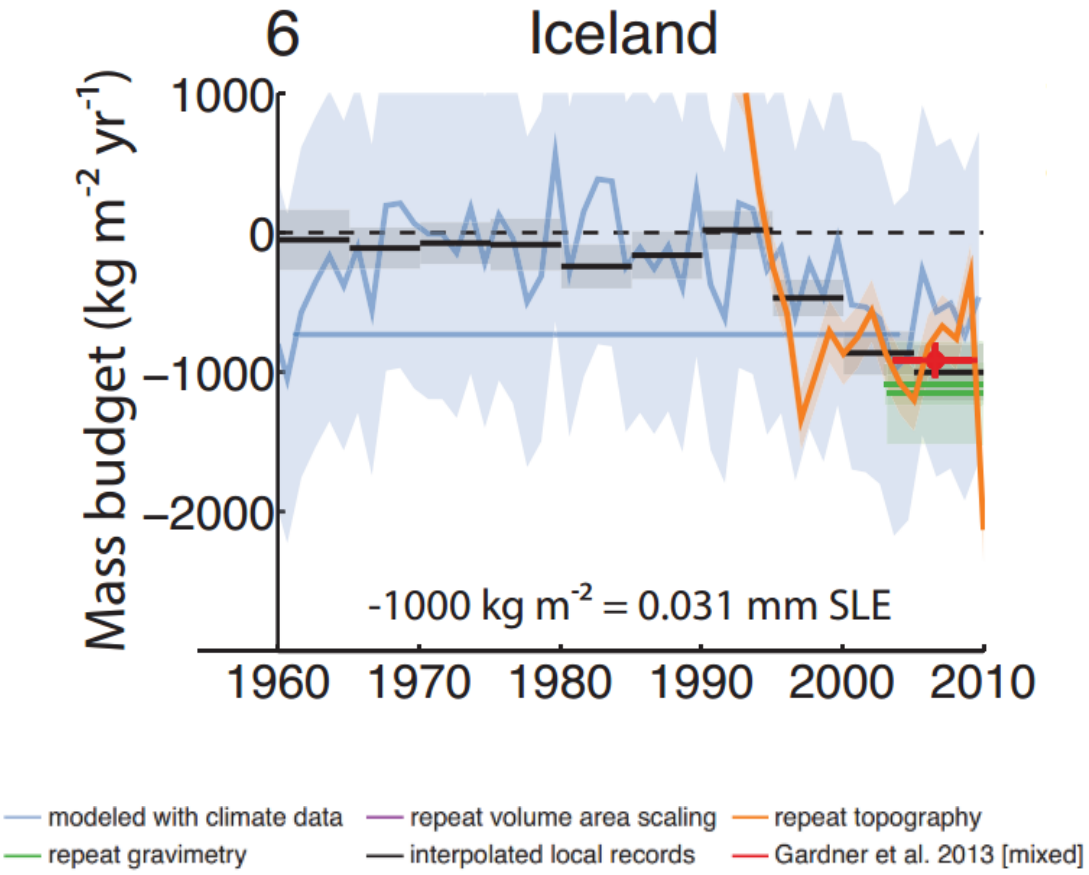

Figure 3.5) Regional glacier mass budgets in units of kg m^{-2} yr^{-1}. Mass-budget estimates include 90% confidence envelopes (IPCC, 2013, p.341).

Chapter 4

A method for the automatic monitoring of an ice cliff

4.1 Introduction

As discussed in *Chapter 2*, approaches for investigating calving activity at the termini of glaciers are limited by the methods which are available that can be used to record individual events. Remotely-sensed data of glaciers is usually acquired from satellite or aircraft-based sensor technologies. The nature and scale of changes at the terminus can be lost due to this aerial view, and the ability to identify small-scale events and those which undercut the terminus is hindered by the resolution and radiometric contrast of remotely-sensed data. Terrestrial laser scanning (TLS) has been identified as a potentially suitable technique for monitoring the ice cliff of Fjallsjökull, based upon knowledge gained from previous studies (Conforti *et al.*, 2005; Chapuis & Tetzlaff, 2014; Petlicki *et al.*, 2015). With the advent of very-long-range laser scanning technology (e.g. Riegl *VZ*-4000), data of the ice cliff could be obtained from a safe distance (*c.* 1000 m), and offers the potential to map the glacier termini in 3D at resolutions of an order of magnitude greater than those which are currently available using alternative methods (e.g. Landsat TM imagery). Furthermore, scans can be acquired with a much higher frequency than in previous studies due to the acquisition speed of newer instruments (e.g. Conforti *et al.*, 2005), allowing data to be collected at hourly, or sub-hourly intervals across a glacier terminus.

This chapter presents the methods used in this study, which allows changes at the ice cliff of a lacustrine glacier to be mapped near continuously throughout a monitoring period, with the implementation of an automatic 3D time-lapse (4D) laser scanning system. This chapter will describe the methods used to acquire 3D TLS data of the terminus of the glacier in parallel with the environmental data collected in order to assess controls on any changes observed at the ice cliff. The steps taken in the field to acquire this TLS data, pre-processing and post-processing of the data will also be presented.

4.1.1 Terrestrial laser scanner: VZ-4000

Terrestrial laser scanning is a ground-based form of LiDAR (Light Detection and Ranging), an active remote sensing technique. This study focuses on ice surfaces which have a low reflectivity in the near-infrared because of their high liquid water content (Gabbud *et al.*, 2015). The reflectivity of a glacier surface is further affected by the purity of surface ice (Gabbud *et al.*, 2015) which is known to alter a calving event (Conforti *et al.*, 2005), with debris content and cover, and changes in wetness at, for example the base of the ice cliff near the waterline. Most laser scanning systems are not able to measure ice surface geometry due to their relatively low sensitivity. Longer-range, and hence high sensitivity instruments are, however, increasingly capable of imaging ice surfaces.

In this study a RIEGL *VZ*-4000 scanner was deployed, which is a very-long-range 3D VZ-line scanner using a class 1 laser which is theoretically capable of acquiring measurements from wet ice at *c*. 1300 m in a standard clear atmosphere. The scanner can capture returns from up to a maximum of up to 4000 m for a planar specular white surface (Figure 4.1). The calving front at Fjallsjökull fell just within the range of the instrument at the time of the survey from a suitable vantage point. In future, the position of the TLS system, or type of system used would likely have to be adjusted to meet these requirements as the glacier retreats and the range increases.

The *VZ*-4000 is marketed to operate even in poor visibility and demanding multi target situations caused by dust, haze, rain, and snow (Riegl Data Sheet, 2015). The *VZ*-4000 laser scanner emits a near-infrared laser pulse and measures the time required for the signal to be reflected from the target of interest back to the receiver, based on echo digitisation and waveform processing. The distance between the object and the instrument is calculated by recording the time between transmission and return of the laser pulse using the speed of light. For further system characteristics see Table 4.1.

This type of instrument has been used extensively to monitor rock slopes (e.g. Rosser *et al.*, 2005; Kromer *et al.*, 2017), rivers (e.g. Hodge & Brasington, 2009; Wheaton *et al.*, 2009) and volcanoes (e.g. Pesci *et al.*, 2007; Nguyen *et al.*, 2011), to name but a few geomorphological applications. Though there have been fewer examples of the application of TLS to ice surfaces, studies have demonstrated that, in practise, it is possible to monitor change at ice cliffs using this method (Telling *et al.*, 2017). In this study, the Riegl *VZ*-4000 acquired data from a complex natural surface. Ice at the terminus of Fjallsjökull was wet, highly specular and angled acutely to the scanner look view, all of which are factors that can undermine the quality of LiDAR data. The next section will discuss the application of the *VZ*-4000 to the ice cliff at Fjallsjökull and the steps taken to acquire data in the field.

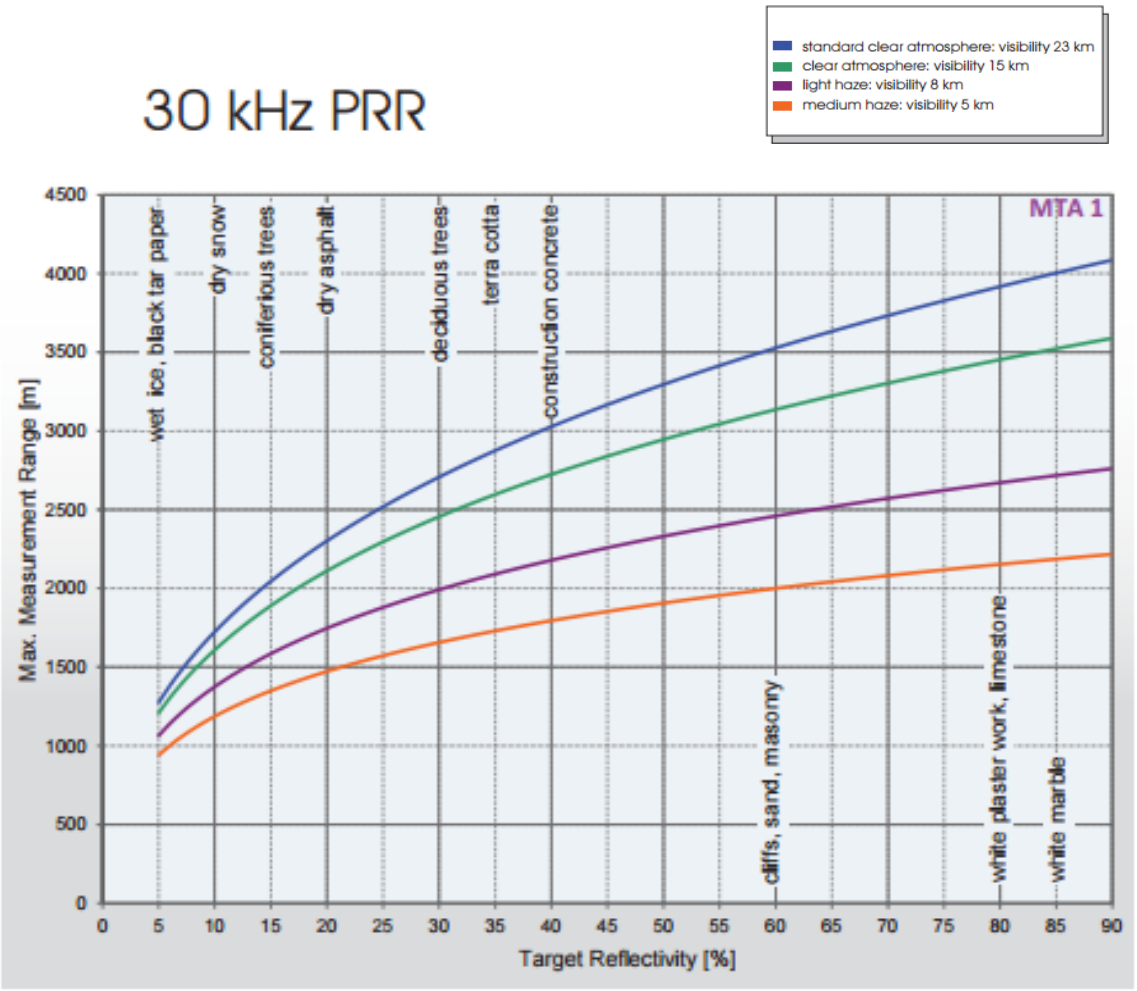

Figure 4.1) Maximum measurement range of the Riegl *VZ*-4000 © RIEGL LMS, www.riegl.com. The following conditions are assumed: a flat target larger than footprint of laser beam, perpendicular angle of incidence, average brightness, ambiguity resolved by post processing with RiMTA TLS (Riegl Data Sheet, 2015). Reflectance of the glacier surface was in the order of 5-10 % for ice surfaces, and 20 % for debris covered surfaces.

Table 4.1) System parameters for the Riegl VZ-4000 (Riegl Data Sheet, 2015).

System parameters	Value (range)
Measuring range for:	
wet ice	> 1500
dry snow	> 2000
debris	> 1500
Accuracy	± 15 mm
Precision/Repeatability	± 10 mm
Laser wavelength	Near infrared
Laser beam divergence	0.15 mrad
Laser beam footprint (Gaussian beam definition)	150 @ 1000 m
Field of View (FOV):	
horizontal	0° - 360°
vertical	-30° to 30°
Power supply	11 – 32 V DC
Temperature range:	
operational	- 0°C up to + 40°C
storage	-10°C up to + 50°C

4.2 Application to Fjallsjökull

4.2.1 Field data acquisition

The nearest possible location to install the *VZ*-4000 was approximately 800-1300 m (depending on glacier geometry) away from the ice cliff (Figure 3.1; 4.2). To achieve returns at such long distances the instrument was operated on the lowest measurement frequency and greatest range (30 kHz pulse repetition rate) available. At this frequency, a measurement step of 0.007° was possible, giving an average point spacing of ~ 0.15 m at 1 km. The system uses a class 1 (eye safe) laser and no precautions had to be taken by the instrument operators, or to manage the optical risk to people in the landscape. The resulting scan program took 36 minutes to complete. The coverage of the raw scan is shown in Figure 4.3. With the application of VNC Viewer operated through a Panasonic Toughbook via Wi-Fi to the *VZ*-4000, the scan program was fully automated using a built in time-lapse controller. This process allowed the acquisition of a 4D (3D time-lapse) sequence without direct user supervision of the system, meaning that scans could be acquired over a continuous period, night and day. To allow continuous monitoring, the scanner was powered simultaneously by three independent

Figure 4.2) The fieldsite at Fjallsjökull. The *VZ*-4000 was housed inside the tent porch on a moraine directly opposite the ice cliff of the glacier. The weather station is mounted to the left of the tent.

sources of power (two batteries and a petrol generator) which were 'hot swapped', whereby the power source was switched without interruption to the instrument.

In total, 46 scans were acquired; 28 were of sufficient quality for processing and subsequent analysis, for full details see Table 4.2. The scans which were discarded were not of sufficient quality for use in further analysis due to a variety of reasons. Mostly, this was due to inclement weather (discussed in *Chapter 6*) such as heavy rain and mist which reduced the number of laser pulse returns from the glacier surface. After heavy rain on the evening of the 14th August, the equipment started to fail due to water ingress and high humidity within the instrument. Data up to 04:30 in the morning on the 15th August was able to be retrieved from the instrument, at which point the instrument declared a 'fatal error'. There was no usable data after 21:30 on the 14th August because the returns from the glacier were significantly reduced due to heavy rain.

In order to meet aim (1) and address the research questions of this study, the *VZ*-4000 was operated from one single scan position (Figure 4.4). For complex glacier surfaces, though not ideal, Gabbud *et al.* (2015) have demonstrated that for sub-daily measurements, a survey can be operated from a single position as long as a suitable vantage point can be identified. The advantage of using one single scan position, rather than multiple overlapping scan positions, which is standard practise, is that there is a greater precision for measurements at the sub-daily timescale (Gabbud *et al.*, 2015) and the registration uncertainty between point clouds is eliminated (Lague *et al.*, 2013). Some limitations of this method are that because only one scan position is used, scan shadows (occlusions) are present, which could only be filled by data collected from multiple scan positions. Areas of low point density are also evident due to acute angles of incidence between the target and the scanner. These tended to be located at the edge of the scan pattern, and at sharp edges on the glacier surface which resulted in a reduction in data density at the edges of the area of interest where the strike of the terminus became more oblique to the scanner look direction.

Table 4.2) Laser scan data acquisition between the 13th and 14th August 2016.

Scan number	Scan timestamp	Date/Time	Used in analysis	Notes
1	160813_151907	13/08/2016 15.19 hrs	No	Panorama scan
2	160813_152613	13/08/2016 15.26 hrs	No	Test scan
3	160813_152753	13/08/2016 15.27 hrs	Yes	Test scan
4	160813_160251	13/08/2016 16.02 hrs	Yes	Test scan
5	160813_170000	13/08/2016 17.00 hrs	Yes	Test scan
6	160813_171504	13/08/2016 17.15 hrs	Yes	Test scan
7	160813_173000	13/08/2016 17.30 hrs	Yes	Clear visibility
8	160813_183000	13/08/2016 18.30 hrs	Yes	
9	160813_193000	13/08/2016 19.30 hrs	Yes	
10	160813_203000	13/08/2016 20.30 hrs	Yes	
11	160813_213000	13/08/2016 21.30 hrs	Yes	
12	160813_223000	13/08/2016 22.30 hrs	Yes	
13	160813_233000	13/08/2016 23.30 hrs	Yes	
14	160814_003000	14/08/2016 00.30 hrs	Yes	
15	160814_013000	14/08/2016 01.30 hrs	Yes	
16	160814_023000	14/08/2016 02.30 hrs	Yes	
17	160814_033000	14/08/2016 03.30 hrs	Yes	
18	160814_043000	14/08/2016 04.30 hrs	Yes	Low reflectivity
19	160814_053000	14/08/2016 05.30 hrs	Yes	
20	160814_063000	14/08/2016 06.30 hrs	Yes	
21	160814_073000	14/08/2016 07.30 hrs	Yes	
22	160814_083000	14/08/2016 08.30 hrs	Yes	
23	160814_093000	14/08/2016 09.30 hrs	Yes	
24	160814_103000	14/08/2016 10.30 hrs	No	Obstruction
25	160814_104911	14/08/2016 10.49 hrs	No	Raining
26	160814_110118	14/08/2016 11.01 hrs	No	Raining useable
27	160814_113632	14/08/2016 11.36 hrs	No	Reduced extent
28	160814_114707	14/08/2016 11.47 hrs	Yes	Useable
29	160814_123000	14/08/2016 12.30 hrs	Yes	
30	160814_133000	14/08/2016 13.30 hrs	Yes	
31	160814_143000	14/08/2016 14.30 hrs	No	Mist, poor visibility
32	160814_153000	14/08/2016 15.30 hrs	Yes	
33	160814_163000	14/08/2016 16.30 hrs	Yes	
34	160814_173000	14/08/2016 17.30 hrs	Yes	
35	160814_183000	14/08/2016 18.30 hrs	No	Mist, poor visibility
36	160814_193004	14/08/2016 19.30 hrs	Yes	
37	160814_203000	14/08/2016 20.30 hrs	Yes	
38	160814_213000	14/08/2016 21.30 hrs	Yes	Drizzle, last useable scan
39	160814_223000	14/08/2016 22.30 hrs	No	Heavy rain, poor visibility
40	160814_233000	14/08/2016 23.30 hrs	No	Heavy rain, poor visibility
41	160814_003000	14/08/2016 00.30 hrs	No	Heavy rain, poor visibility
42	160814_013000	14/08/2016 01.30 hrs	No	Heavy rain, poor visibility
43	160814_023000	14/08/2016 02.30 hrs	No	Heavy rain, poor visibility
44	160814_033000	14/08/2016 03.30 hrs	No	Heavy rain, poor visibility
45	160814_043000	14/08/2016 04.30 hrs	No	Equipment failure
46	160814_044850	14/08/2016 04.48 hrs	No	Equipment failure

Figure 4.3) The coverage of the scan program which automatically scanned once every hour. The area includes the glacier ice directly in front of the scanner and the area of bedrock to the right but does not extend further to the left of the image. This is because the point density was greatly reduced in this area due to an embayment in the glacier terminus where the ice is beyond the maximum measurement range of the *VZ*-4000.

Figure 4.4) The location of *VZ*-4000 in front of Fjallsjökull under the tent porch to provide some shelter from wind and rain.

4.3 LiDAR point cloud processing

4.3.1 Overview of TLS data processing

In this study point cloud processing required the following steps to be undertaken, with the workflow discussed in Figure 4.9: (1) an initial data quality check in RiSCAN Pro; (2) the removal of clear visual outliers, for example arising from atmospheric reflections such as dust or moisture, icebergs floating in the lake, tourist boats operating in front of the glacier and wildlife, using manual point removal in RiSCAN Pro; (3) 3D rigid rotation of the point cloud around the *z*-axis from the scanners own coordinate system (SOCS) to the project coordinate system (PRCS) so that the ice cliff is parallel to the *x*-axis in RiSCAN Pro, to enable the data to be readily mapped in a 2D projection in {*x*, z}; (4) Exporting of *.LAS files and transformation of the point cloud by 90° around the *y*-axis in Cloud Compare so that the data is in a cliff-normal view for further processing in ArcMap; and (5) the production of filtered 2D raster data in ArcMap. Co-registration was not required because only one scan position was used.

4.3.2 Data quality check

An initial check of the data showed that the overall coverage of the glacier was highly variable. Although the average point spacing was 0.15 m, some areas of the ice cliff did not produce any signal returns and other areas had a greater density of points. There was also a considerable decay in data density with distance from the scanner, and also from surfaces which were steeply inclined from the scanner. Therefore, the point density of the scans was not uniform within individual scans, but also between scans (Figure 4.5). This is to be expected in a natural environment, where environmental conditions are constantly changing due to rain, mist, moisture levels at the glacier surface, and glare into the instrument from sunlight.

It would be unrealistic to expect to capture a surface, especially one as complex as a glacier terminus, homogenously between surveys (e.g. Hodge & Brasington, 2009; Lague *et al.*, 2013; Figure 4.6). It is important to note the nature of this heterogeneous data, because although specific processing methods can be applied to overcome the nature of the raw data, it will be useful to refer back to the raw data when drawing conclusions about any changes detected. Based on a visual assessment of the point cloud data, the quality was too poor in some scans for use in subsequent analysis. For example, at 14:30 on the 14th August 2016 (Table 4.2) the presence of mist caused a very low number of returns from the glacier surface.

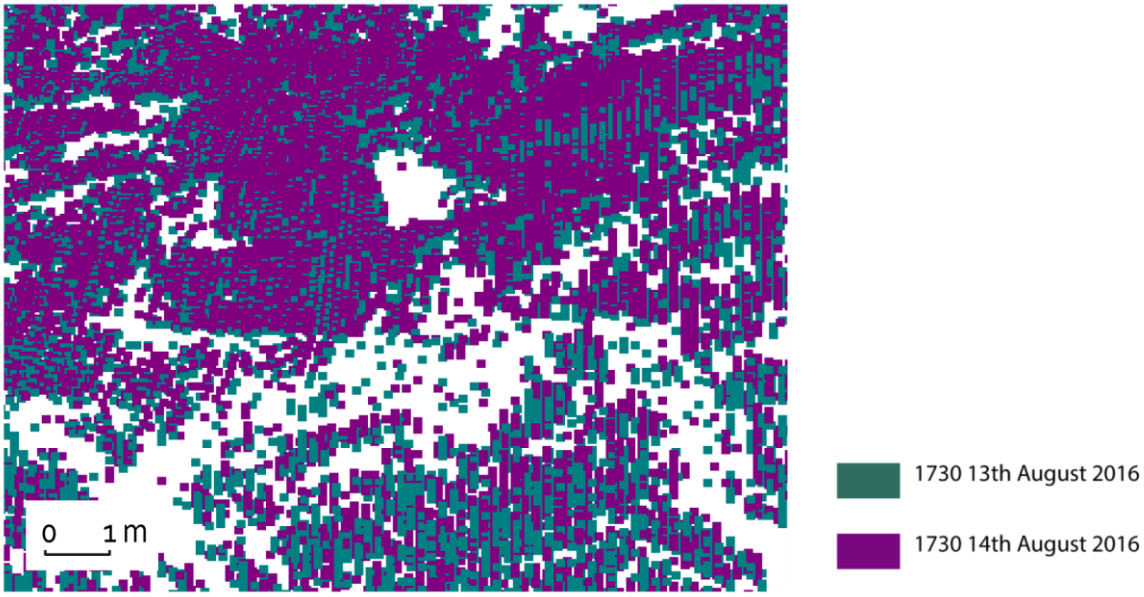

Figure 4.5) Two point clouds showing the variable point density between different scanning epochs and scan shadows in the raw data, these holes in the data will have been interpolated across in the DEMS.

Figure 4.6) Complex topography of the glacier surface at Fjallsjökull.

4.4 Pre-processing

There was a large volume of LiDAR data which required careful pre-processing in order to operate an efficient workflow for further analysis. The raw data which was downloaded from the scanner was over 6 GB in size, and each scan contained just under seven million points. In order to undertake analysis on the data, it was necessary to filter the LiDAR data so that the files were not too cumbersome to use in software such as Cloud Compare and ArcMap. This involved filtering the data so that only the Area of Interest (AOI) and any required points were kept in the dataset. Scans between 15:27 13th August and 21:30 14th August were manually filtered in RiSCAN Pro to remove points which were not useful to the study including returns from icebergs floating in the lake and bedrock areas in front of the glacier, in addition to erroneous points such as atmospheric reflections (Figure 4.9). The point clouds were then rotated in the project coordinate system (PRCS) around the *z*-axis so that the ice cliff and direction of glacier flow were as parallel as possible to the *x*-axis (Figure 4.9). This is important for further processing in ArcMap whereby the changes at the ice cliff are to be investigated in the cliff-nadir view. The point clouds were then exported in *.LAS file format, a binary format which maintains LiDAR specific information, and offers faster performance than alternative formats such as *.ASCII. The point clouds were then transformed by 90 ° around the *y*-axis in Cloud Compare so that the data was in a cliff-normal view when displayed in a map-view in ArcMap; and (5) the production of filtered 2D raster data in ArcMap. Co-registration was not required because only one scan position was used.

4.4.1 Point cloud to gridded raster image conversion

For the purposes of change detection, it is common practise to grid TLS-derived point clouds into 2.5D rasters, because of their heterogeneous point densities, and cumbersome file sizes (Schürch *et al.*, 2011; Fischer *et al.*, 2016). The scans acquired in this study do not have a uniform point density within individual scans, but also between scans. The former can be attributed largely to the particularly complex geometry of the glacier surface (Figure 4.6), but also variable target reflectivity due to spatial and temporal changes in surface moisture and debris content. The latter is, in part, due to abrupt changes in slope, aspect, local surface roughness and high local relief, but also to changes in visibility caused by mist and rain (scan 31; Table 4.2).

There is an inherent uncertainty with laser scanning that necessitates the assumption that no point on a surface is measured twice. In relative terms, movement of points therefore has to account for the point spacing, and the probability of the same point having been measured again. Gridding data overcomes this issue as it transforms 3D point clouds with no topological context into continuous 2, 2.5 or 3D surface, from which comparisons can be made.

Digital Elevation Models (DEMs) are a simple and efficient means of handling complex topographic data and consist of images of the interpolated surface, which are essentially 2D maps, whereby each pixel is assigned a value which represents the depth relative to the plane of the cliff, a format commonly referred to as 2.5D (Figure 4.9 and 4.10). This is a technique which is commonly used in landslide monitoring (e.g. Rosser *et al.*, 2013) but at present has not been used to monitor an ice cliff. Point clouds were gridded in ArcMap following the workflow outlined in Figure 4.9. The point clouds were gridded to a 0.2 m spatial resolution raster using the average linear interpolation in Spatial Analyst (ESRI ArcMap).

Previous studies have shown that the survey strategy appears to be more important than the choice of interpolation algorithm (Bater & Coops, 2009; Schürch *et al.*, 2011). The best recommended grid size of 0.2 m was estimated using a point pattern analysis grid size calculator (Hengl, 2006).This resolution was also deemed to be a higher resolution than most macro surface roughness features and yielded at least one data point for most of the grid cells, except for areas of significant occlusion. The result of this processing is the conversion of the time-series of 3D point clouds to a sequence of DEMs which will be further analysed in ArcMap.

4.4.2 Sources of uncertainty in TLS data

Uncertainty in TLS-derived surface elevation changes can be attributed to two main sources: (1) errors related to data acquisition inherent within terrestrial laser scanners; and (2) errors originating from data processing and DEM production (Schürch *et al.*, 2011; Fischer *et al.*, 2016). Uncertainty in the TLS measurements can arise from the occlusion of a surface due to surface roughness. This effect causes the spatial sampling of rough surfaces to never be identical between surveys (Hodge & Brasington, 2009).

Therefore, even if the surface does not change between a survey, a small uncertainty in range will be captured (Schürch *et al.*, 2011), and cannot be overcome. This justifies the need for a confidence interval, below which the difference measured between scans cannot be considered sufficiently large enough to be statistically significant to constitute a change. In

the case of this study, the root mean square difference is determined in RiSCAN for successive scans of an unchanging and static reference surface on the rock face adjacent to the glacier, at 0.11 m. As scans are captured from a single and fixed view point, all errors associated with relocation of the instrument, cloud alignment, and variable errors between instruments are negated. Figure 4.7 shows frequency distributions for an off-ice area of bedrock located directly in front of the terminus.

When producing DEMs, gaps in the raw data are interpolated across. An estimation of the surface which exists in the gap is produced using the characteristics of the surrounding surface. Depending on the method of interpolation, levels of error can vary. Figure 4.8 gives an idea of how widespread gaps in the LiDAR data were. For a glacial surface, the impact of interpolating across gaps can be significant and needs to be dealt with carefully. For example, areas of no data could have arisen either from a scan shadow due to the scanner look-view, or because of crevasses. Due to this, it was necessary to follow a method which interpolated where there was sufficient data, and did not interpolate across crevasses or areas of no data because the glacier surface was so variable on the sub-metre scale.

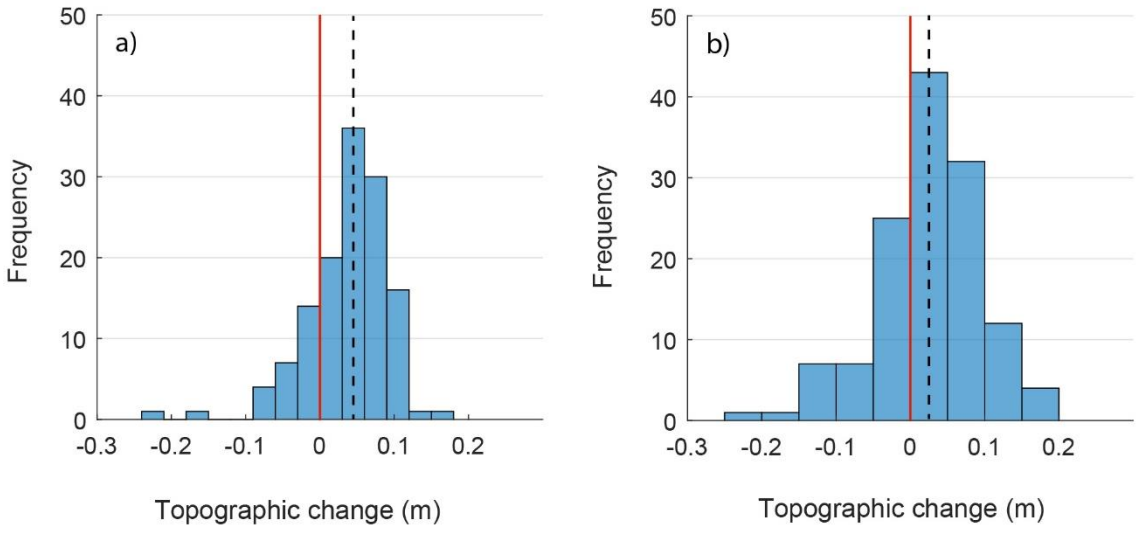

Figure 4.7) Frequency histograms for a 6 m^2 area of bedrock located infront of the terminus. a) shows topographic change detected between 17:30 to 18:30 13th August. b) shows topographic change for the same area of bedrock between 17:30 13th August to 21:30 14th August.

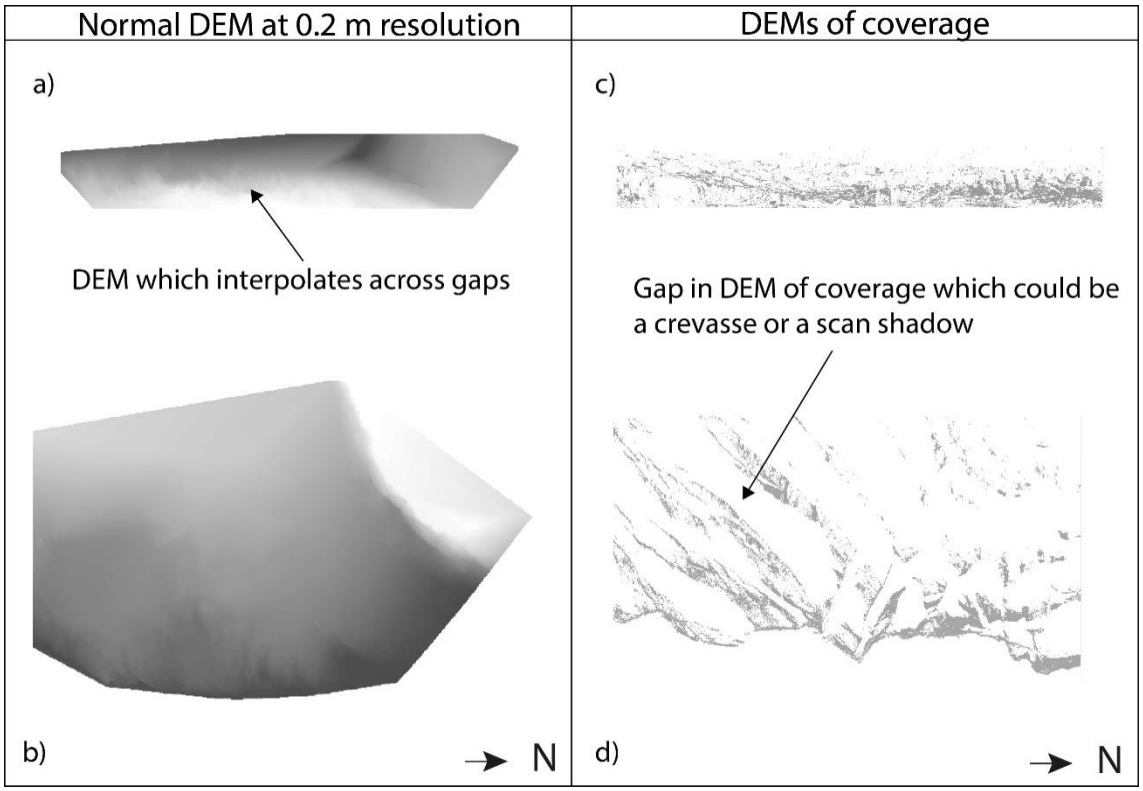

Figure 4.8) Figure showing a) cliff-normal DEM and b) plan-view DEM with holes interpolated. Figures c) cliff-normal DEM of coverage and d) plan-view DEM of coverage, where areas without data i.e. holes have been removed (for full processing steps see Figure 4.9).

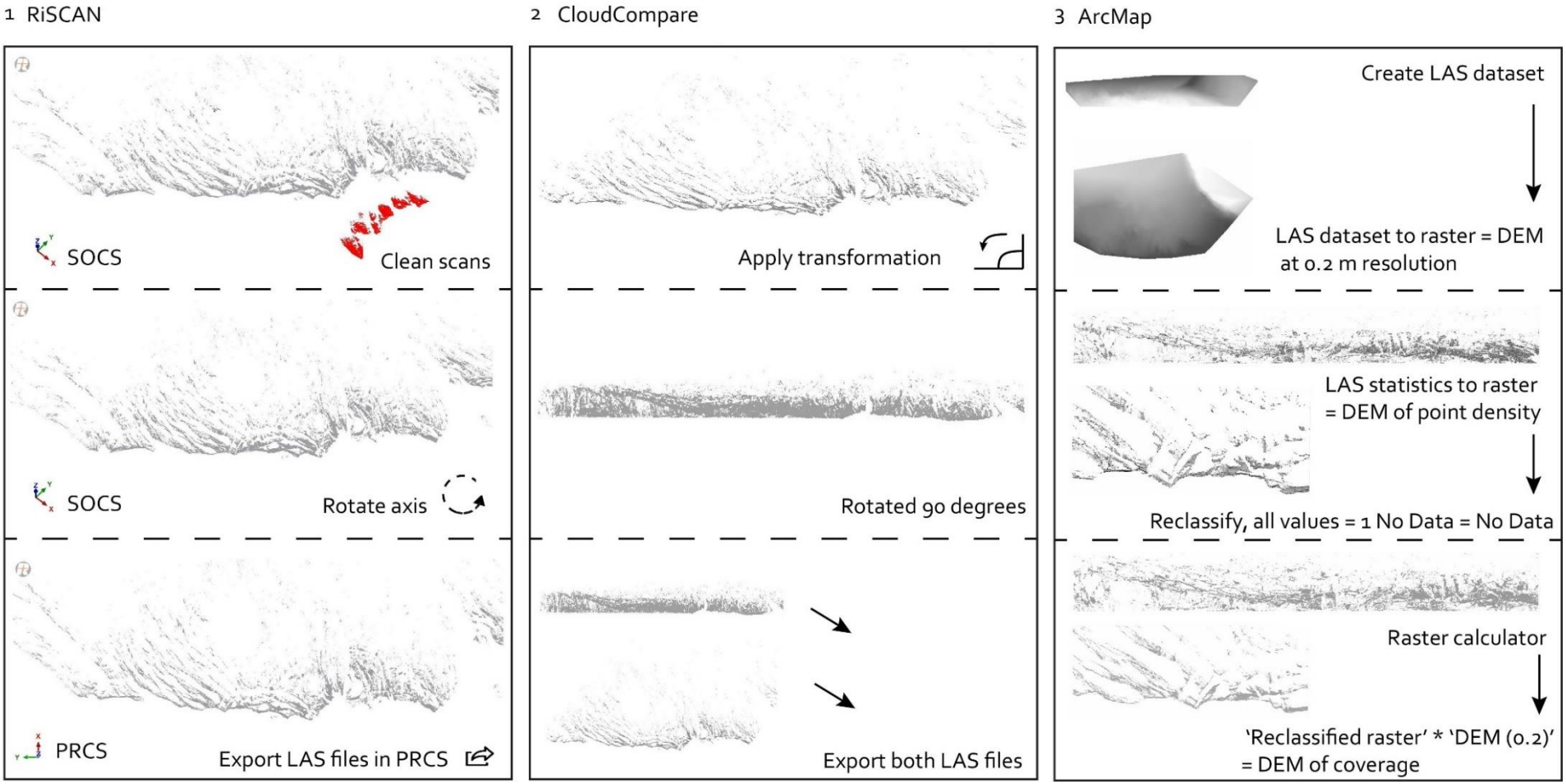

Figure 4.9) Schematic workflow of TLS data processing from raw TLS data to gridded raster data.

4.5 Extracting measurements of glacier change from LiDAR data

In order to address the research questions outlined in *Chapter 1*, a number of measurements of glacier change will be extracted and analysed from the scanning data. A 2.5D raster time–series dataset spanning 28-hours has been produced from 28 individual 3D LiDAR surveys of the ice cliff that describes the cliff topography through time. To examine RQ1 and define the spatial characteristics of calving behaviour at the ice cliff at hourly to sub-hourly timescales, and RQ3, to explore whether observations of the magnitude/frequency of events match those from previous research, change analysis will be performed on this time-series data. The basic principle of change analysis is to compare two or more datasets of the same geospatial extent collected at different times, a common technique used to assess geomorphic change in the geosciences. Change analysis will include change detection from sequential DEMs of Difference (DoDs), 2D vertical swath profiles, and an assessment of cumulative change for elevation up cliff in the form of zonal statistics, all will be performed in ArcMap. For these analyses, the data have been clipped to an Area of Interest (AOI; Figure 4.10). The AOI is 300 m wide and extends 150 m back from the ice cliff, it is located in the area of greatest density within the total point cloud. To help address RQ2 and define the factors controlling the pattern of ice loss at the terminus, velocity measurements will obtained from point cloud data in Cloud Compare using direct cloud-to-cloud comparison (C2C) and mapped onto the glacier terminus.

Figure 4.10) The AOI which is used in change analyses. The AOI is 300 m wide and extends back 150 m from the glacier terminus.

4.5.1 Velocity measurements from direct cloud-to-cloud comparison

Conventionally, satellite data is used in glaciological studies to determine glacier velocities from sequential aerial-view data (Scherler *et al.*, 2008), and some studies have used multi-temporal airborne LiDAR data (Schwalbe *et al.*, 2008). Such studies use a feature tracking method, whereby discrete features such as meltwater channels and crevasses identified on a glacier surface can be tracked in sequential imagery. The displacement of these features is divided by the total time between imagery to derive a velocity vector. In this study, because the data of the glacier surface is obtained in full 3D and the location of each point is provided with precise (± *c.* 0.1 m) *x*, *y* and *z* coordinates, it is possible to calculate the displacement between survey periods in the *x*-axis as the surface velocity assuming that melt in this axis is below the confidence interval (0.11 m).

Using this principle of displacement of points between surveys (Figure 4.11), surface velocity calculations were carried out in Cloud Compare. Using direct cloud-to-cloud (C2C) comparison of two scans, 17:30 on the 13th August and 17:30 on the 14th August, this gave the average velocity for a full 24-hour period. The standard C2C method in Cloud Compare uses a simple nearest neighbour (Hausdorf) approach to measure the distance between point clouds. A gridded raster (0.2 m resolution) of the C2C comparison was exported from Cloud Compare in the ASCII format and velocity maps were then produced in ArcMap using this data. This method is computationally simpler and less time consuming than the feature tracking method. Figure 4.11 shows an overlay of two scanning epochs to demonstrate the displacement which is observed in the TLS data.

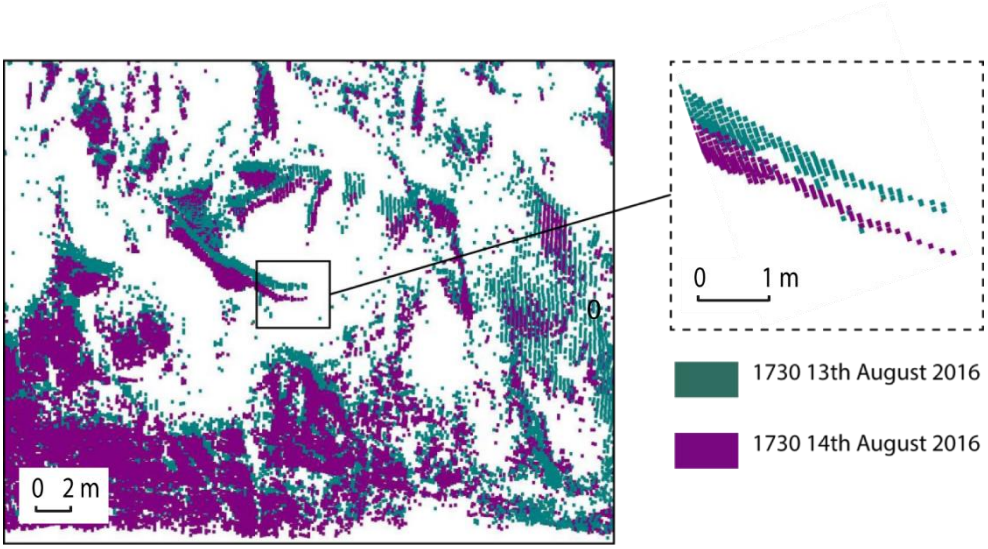

Figure 4.11) Scanned ice structures 24 hours apart showing the displacement observed between two epochs.

4.5.2 Change detection at the ice cliff from 'DEMS of Difference'

Change detection involves the subtraction of two surfaces obtained at different times giving the value of change of a surface between the two surveys. Change detected in consecutive DoDs was cumulatively mapped onto the ice cliff for the period between 15:27 13th August and 21:30 14th August 2016 using the scans listed in Table 4.2. DEMs of Difference are 2.5D rasters that display the difference between two rasters collected at different points in time and are presently the most common method of point cloud comparison used for large scale near-planar geometries in the geosciences (Lague *et al.*, 2013).

Although perhaps a misnomer, the term DoD is the commonly accepted term for this method of change detection. This method has been successfully demonstrated with point cloud data from river beds (Schürch *et al.*, 2011) and rock cliffs (Rosser *et al.*, 2005; Abellán *et al.*, 2010). Two DEMs are subtracted from each other on a pixel by pixel basis (Lague *et al.*, 2013), in this case using the 'Raster Calculator' tool in ArcMap (ESRI, 2017a), in a non-pairwise manner, as to do reduce the error in the method.

After change detection was undertaken, areas of spuriously high change were observed in the data, particularly near the edges of ice structures on the glacier surface. This error could have arisen from the precision of the laser instrument acting on the laser pulse, or the 'smearing' of the pulse across the terrain. This smearing effect results in an increased pulse footprint size which is caused by the incidence angle between the laser pulse vector and the terrain (Schaer *et al.*, 2007). Because a laser scanner never scans the same point twice, an imperceptibly small difference in the incidence angle can result in returns which are near or far, where there are edges (Figure 4.12).

To remove this erroneous change which occurred near sharp edges on the glacier surface, an edge detection technique was performed in ArcMap. This involved using the 'Slope Tool' in Spatial Analyst to create a DEM of slope values. Values above a slope threshold of 65° were reclassified into a binary raster image which was used to mask the areas of error which should be removed from the DoDs. Although this was successful in removing the majority of erroneous change, it does mean that events which did occur near the edges of features are removed from the analysis, and therefore small events could have been underestimated. Finally, the DoDs were clipped to an AOI with a good point density.

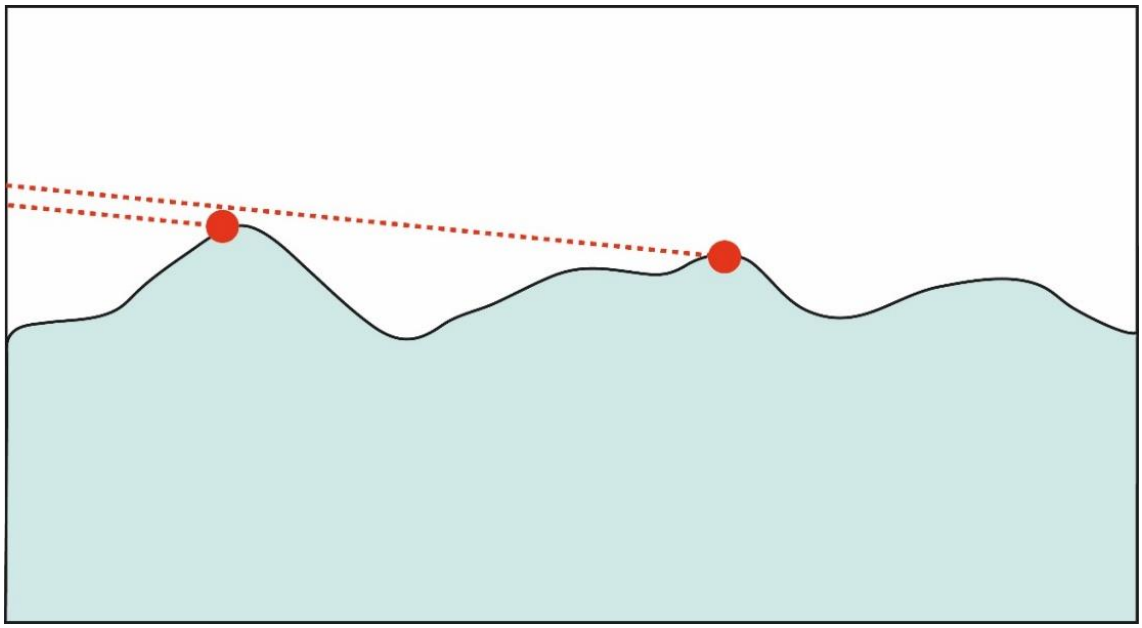

Figure 4.12) Illustration of a laser pulse hitting an edge, and then missing the same edge by a small margin but creating a point of spuriously large change.

4.5.3 Time-series of swath profiles at the ice cliff

In order to access the geometric qualities of change at the ice cliff, three sets of vertical swath profiles were extracted from each raster image. The profiles were spaced evenly across the ice cliff but took into account the point density in the original data (Figure 4.13). Each swath profile was 1 pixel wide (0.2 m). The profiles were extracted from areas with a good point density and minimal scan shadowing in order to justify the quality of the outputs. This may have introduced some level of systematic bias because profiles could be extracted from certain surface configurations. However, this method of selection was necessary due to the quality of the data, and may be something to consider in future studies. The process of profile extraction was batched and involved drawing polyline shapes using the 'Editor' function and then using the 'Densify Tool' to add vertices at 0.2 m intervals along each polyline. The vertices were converted to points using the 'Feature Vertices to Points Tool' which creates a feature class containing points generated from specified vertices or locations of the input features (ESRI, 2017a). Finally, the tool 'Extract Multi-Values to Points' was used to extract the raster values from the surface and these were added as attributes to the profiles using the 'Add XY Coordinates Tool'. This resulted in a 'Table of Attributes' which were exported and edited in Excel before plotting profiles in Matlab.

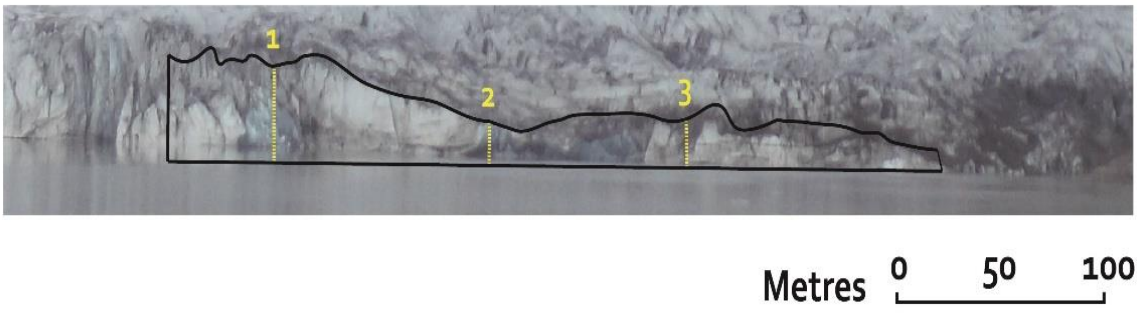

Figure 4.13) The clipped AOI (black line) of the scan data overlaid onto a photo of the calving front of Fjallsjökull on the 13th August. The positions of profiles 1, 2 and 3 are marked by a yellow dashed line. The scale is accurate for the AOI only.

4.5.4 Summary statistics of glacier change measurements

In order to define any general patterns of change for the glacier in plan-view, surface characteristics were summarised. Summary statistics were extracted in ArcMap using the 'Summary Statistics' (ESRI, 2017b) which resulted in the extraction of the statistic variables: Mean, Maximum, Minimum, Standard Deviation of the entire glacier surface within the plan-view AOI.

4.5.5 Statistical patterns of change for height up-cliff

In order to categorise the data in a manner that allowed the investigation of up-cliff changes and to consider patterns within this in space and time (RQ1), the glacier was zoned into 1 m horizontal bands that spanned the width of the AOI (Figure 4.14). These bands were stacked vertically up the ice cliff from the toe, and the summary statistics for each band were obtained using the tool 'Zonal Statistics' in ArcMap. These statistics include the mean, maximum, and standard deviation of difference for each 1 m horizontal band.

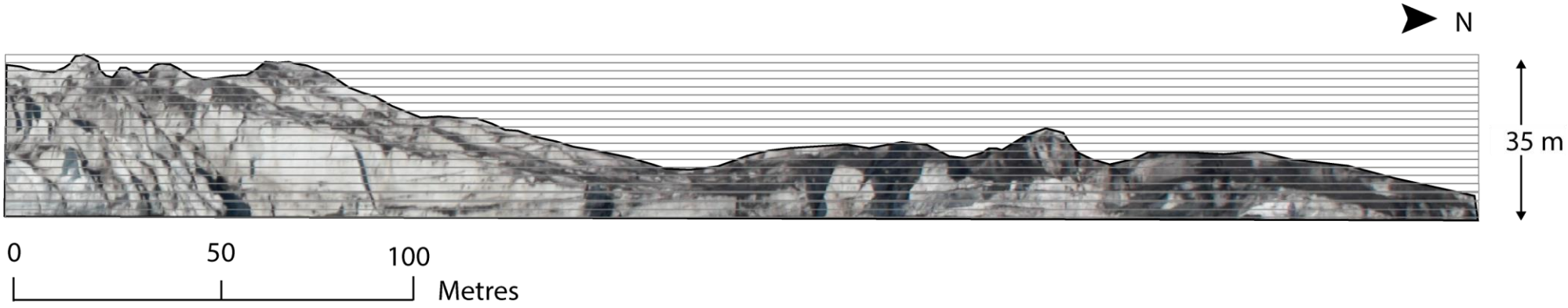

Figure 4.14) Elevational bands used in zonal statistics. The clipped AOI (black line) of the scan data overlaid onto a photo of the calving front of Fjallsjökull on the 13th August. The grey boxes which span the width of the AOI are bands which are used to calculate up-cliff changes. Each band is 1 m high and there are a total of 35 bands.

4.6 Environmental data acquisition and processing

4.6.1 Meteorological data collection

A Davis Vantage Vue Pro automatic weather station was used to collect meteorological variables during the survey period at 10-minute intervals. The data has gaps due to equipment failure (the battery casing was loose and resulted in a power disconnection to logger) and is therefore complemented by a local automatic meteorological station at Kvísker (~6 km away from Fjallsjökull; Figure 3.1) for the same time periods which provides a more consistent dataset. The meteorological data obtained from Kvísker was provided by the Iceland Met Office and is available from: http://en.vedur.is/weather/stations. This data includes wind speed and direction, temperature, precipitation and barometric pressure.

Unfortunately, due to equipment failure the temperature record for our Fjallsjökull weather station was incomplete. A local automatic weather station at Kvísker was located which is operated by the Icelandic Met Office, approximately 6 km away from Fjallsjökull. Table 4.3 presents a comparison of the variables collected at each weather station. It was hoped that the record from Kvísker weather station would be sufficiently similar to fill in the data gaps in the Fjallsjökull record for some of the variables, such as temperature (Claridge & Chen, 2006; Tardivo *et al*., 2012). One of the key differences which may cause variation in weather between the two sites is that Fjallsjökull weather station was directly opposite the glacier and so could therefore be subject to mild katabatic winds. Both weather stations were at similar elevations, and so should not be significantly influenced by thermal gradients with height above sea level.

4.6.2 Lake level and temperature data collection and processing

Relative lake level and temperature were taken at five minute intervals. A Schlumberger bathymetric Micro-Diver was installed at the lake edge in shallow water which recorded the relative level of the water column above the diver as bathymetric pressure (H_2Ocm). A Baro-Diver was also installed nearby above the lake level, which recorded the barometric pressure and was used to compensate the water level measurements.

Table 4.3) Meteorological variables as collected by the two different weather stations.

Variables	Fjallsjökull	Kvísker
Air temperature	degree C°	degree C°
Wind speed	m/s	Mean m/s
Wind direction	N,S,E,W	compass degree
Precipitation	mm	mm
Atmospheric pressure	Mb	Not collected

The two air temperature records were processed so that the intervals of data acquisition matched. This involved down-sampling the Fjallsjökull record to an hourly interval. To assess whether a linear relationship existed between the Fjallsjökull and Kvísker temperature records, a Pearson's correlation test was performed. Although inevitably subject to time dependence, the resulting Pearson's correlation coefficient of the two datasets was 0.7, indicating a close similarity between the records. Therefore, it is highly likely that there is a relatively simple relationship between the two temperature records. A linear regression of the existing data at Fjallsjökull on Kvísker was performed for each time period where data was present for both weather stations. The resulting equations were used as an approach to model the relationship between the two weather stations and thus provide an estimate for the missing values. The whole temperature record was then smoothed using a 5-hour moving average.

4.6.3 Precipitation record

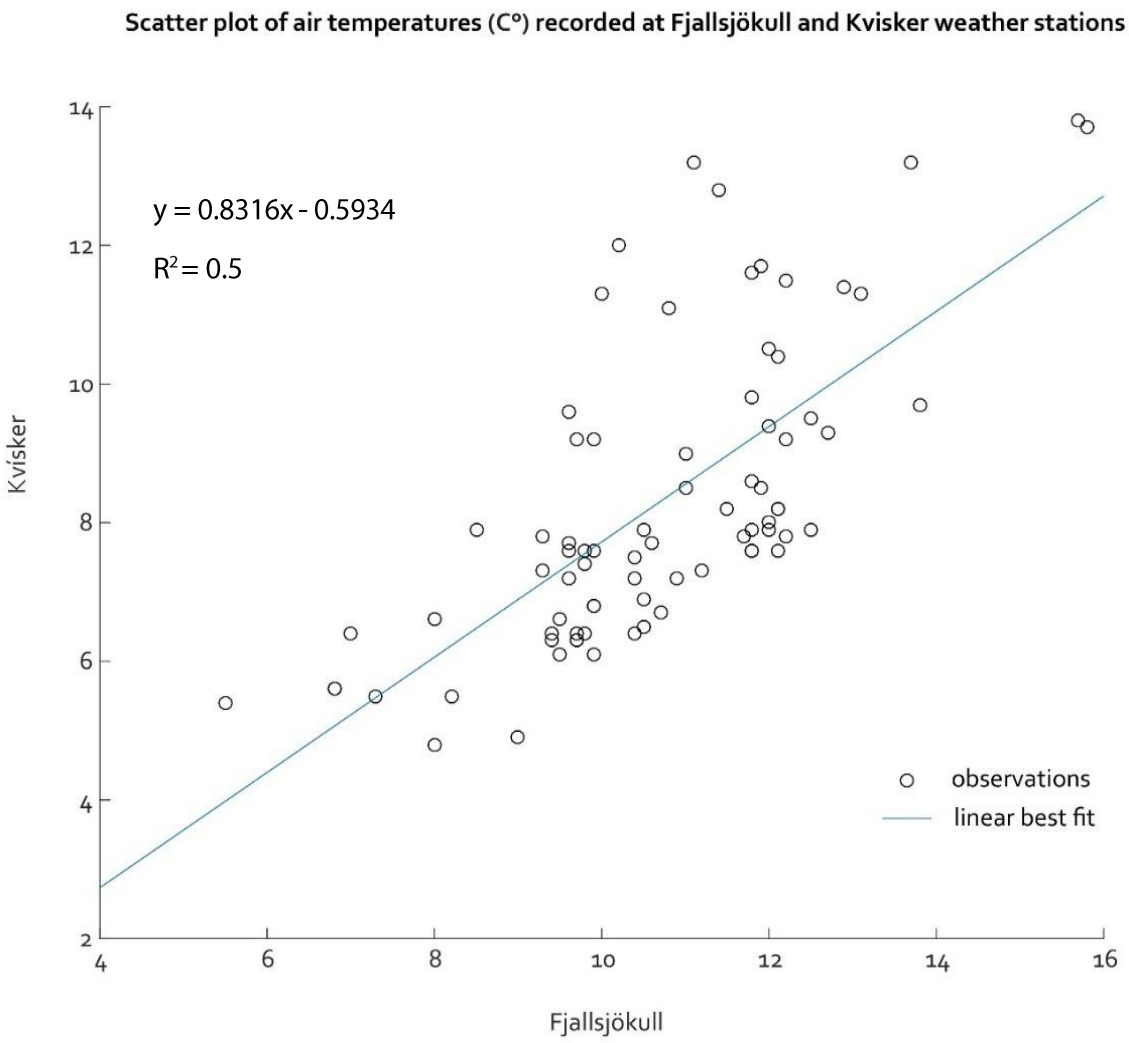

Figure 4.15) Scatter graph showing a linear correlation between the two weather stations at Kvisker and Fjallsjökull.

It was not possible to investigate any correlation between the precipitation record at Fjallsjökull and Kvísker. This is because there were not enough observations of when it was raining at both sites. However, because the sites are very close (~6 km), the precipitation values have been used from the Kvísker weather station, to represent the conditions at Fjallsjökull based on the assumption that the sites are sufficiently close to each other to represent the similar conditions. However, any conclusions drawn from the precipitation data would therefore need to be taken with caution and carefully interpreted.

4.6.4 Wind speed and direction record

Wind speed displayed a relationship between the two weather stations. The wind speed readings at Fjallsjökull are usually lower than those at Kvísker, this could be because the site where the weather station at Fjallsjökull is mounted is sheltered. The wind direction is also notably different at the two stations, which is probably explained by the two different site locations. Therefore, wind speed and direction will not be used in this study.

4.6.5 Summary

The environmental variables which were obtained should provide a valuable insight as to whether the observed calving activity is influenced by air and lake temperature, lake level, or other meteorological variables. This data will be referred to in *Chapter 5*, to investigate potential drivers of calving and whether the activity is likely to be time-dependent or dependent on environmental variables.

4.7 Time-lapse photography of the terminus

4.7.1 Month long time-lapse image dataset

Photographs were obtained at hourly intervals between the 22nd August and 20th September from a single static time-lapse camera system installed on the moraine opposite Fjallsjökull. The aim of this was to provide a qualitative dataset showing the changes at the terminus over part of the ablation season which would provide context to the relatively short scanning survey. The photographs were acquired in *.RAW format in order to reduce noise and to enable post-processing.

4.7.2 Ten day long multi-camera time-lapse dataset

A further dataset between the 13th August and 22nd August was obtained from four static time-lapse camera systems at 10-minute intervals which provided overlapping imagery intended for use in Structure-from-Motion. However, this eventually fell outside the scope of this project, but the images may be used at a later date to compare the SfM and TLS methods.

4.8 Summary of methods and data processing

This chapter details the methods for the automatic monitoring of an ice cliff and its application to the study glacier, Fjallsjökull. The survey design was discussed and the measures taken to obtain the best quality data possible from a complex glacier surface. After survey design, the greatest factor in determining scan quality was inclement weather, with rain not only causing unusable scans due to a reduction in returns, but also eventually causing the failure of the TLS instrument, which is not as rugged as is suggested by the datasheet and technical information provided. The steps taken to process the LiDAR point cloud data were described, with an overview of the data processing including a discussion on the sources of uncertainty which are inherent to laser scanning. The benefits of gridding the sizable LiDAR data files into a raster format, namely computational efficiency and consistency in change analyses were used a justification for this using this processing method in the workflow.

The methods which were used to extract measurements of change from the glacier surface were presented, including, velocity measurements from direct C2C in Cloud Compare, change detection in the form of cliff-normal DoDs which were clipped to an AOI, and a time series of swath-profiles of the ice cliff. In order to consider up-cliff changes at the ice cliff, zonal statistics were undertaken on 35 individual, one metre horizontal bands which extended from the toe to the crest of the ice cliff.

Finally, the approaches used to acquire data of environmental variables were discussed. A continuous meteorological record, including air temperature, precipitation, and wind strength were obtained from a local weather station at Kvísker, which was compared to a more patchy record obtained at the fieldsite. The temperature and level of the lake, Fjallsárlón, were monitored using a bathymetric diver. Photographs of conditions at the ice cliff were also obtained at 10-minute intervals for a ten day period, and hourly for a month after the fieldwork had finished using time-lapse camera systems powered by solar panels. The next chapter will present the results of the study using the methods which have been described.

Chapter 5

Results

This chapter presents the results of the application of automatic TLS monitoring to the ice cliff of Fjallsjökull, a lake-terminating glacier in Iceland. The method which was used in this study was discussed in *Chapter 4*, and involved the use of a Riegl *VZ*-4000 laser scanner mounted 1000 m away from the ice, as well the collection of data pertaining to environmental conditions during the survey. Environmental data collected include air temperature, lake temperature and level, and photographs of the terminus at 10-minute intervals between the 13th August and 22nd August, and at hourly intervals from the 22nd August to the 20th September 2016.

The results demonstrate that TLS can be used as a method to investigate calving at the single event scale and processed LiDAR data is presented which captures the nature of widespread glacier surface movements, velocities and rotational motion coincident and non-coincident with calving. Figure 5.1 provides an overview of the changes which are observed at the glacier terminus. First, *Section 5.1* describes the general glacial characteristics of Fjallsjökull and the macrostructure of the glacier as observed from satellite imagery and TLS data is described in order to contextualise the shorter-term results. Next, patterns in absolute daily velocity will be assessed from a series of velocity maps produced using direct C2C comparison in *Section 5.1.2*. This will be followed by observations of calving activity across the ice cliff using raster based change detection. Data is presented that describes the short term (hourly) movement of and changes to the ice front. Specifically, the pattern of calving events mapped from successive DEMs onto the ice cliff at hourly to sub-hourly timescales (RQ1; *Section 5.1.4*). In order to consider up-cliff patterns of change, the ice cliff is divided in bands from the toe to the crest and the zonal statistics of these up-cliff bands will be presented (*Section 5.6)*.

Environmental variables will be presented which will be important for *Chapter 6*, in discussing whether the changes which occur at the ice cliff are controlled by environmental factors or are time-dependent (RQ2; *Section 5.8*). This will include records of air temperature, lake temperature and level and selected photographs of the terminus which highlight features at the ice cliff such as the presence of a waterline notch. Finally, there will be a summary of the results which are presented.

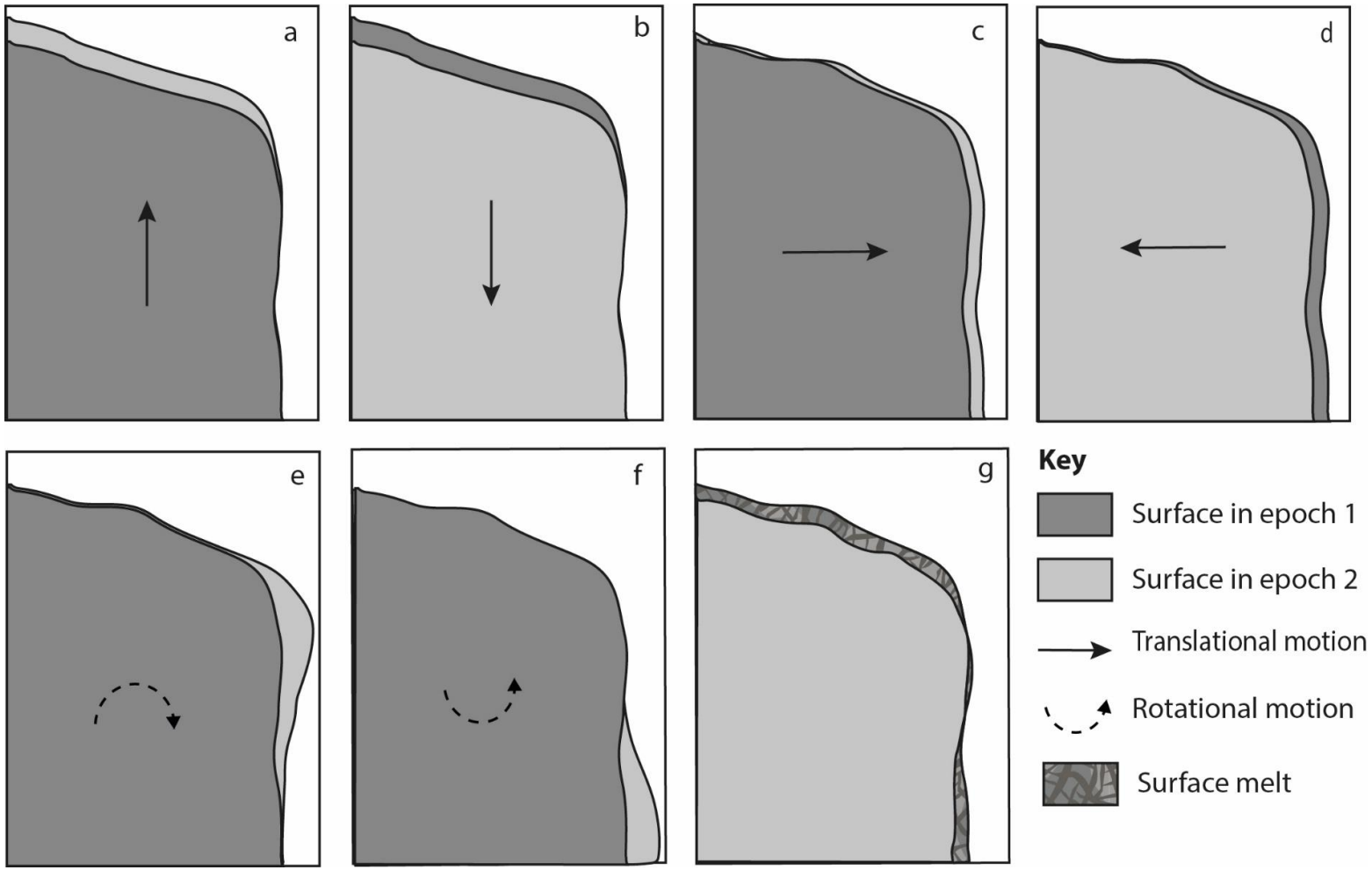

Figure 5.1) Different movement types which may be observed at a glacier surface and which are observed in this study. a) uplift; b) subsidence; c) horizontal translational downstream movement; d) horizontal upstream movement; (e) rotational motion, rotating out from the top of the ice cliff; (f) rotational motion, rotating out from the base of the ice cliff; (g) Surface melt.

5.1 Glacier characteristics

5.1.1 Surface structure of glacier terminus

The maximum freeboard (height of the glacier cliff top above water) of the lake-terminating section of the ice cliff surveyed in this study was measured from the TLS data to be ~35 m above lake level, in places reducing to ~ 7 m. The terminus was not uniform in height and was traversed by jagged surface features resulting from differential melting, and crevasses of unknown depth (Figure 5.2) resulting from the glaciers flow dynamics. The large-scale geometry of the terminus provided an open, unobstructed view of the ice cliff (Figure 5.3). The terminus was arcuate and slightly concave with respect to the viewpoint from the moraine at which the scanner was deployed. The geometry of the terminus has altered with its retreat in recent years (*Chapter 3*), so that the area terminating in what is likely to be the deepest part of the lake (though no recent depth soundings exist) is likely retreating at a faster rate.

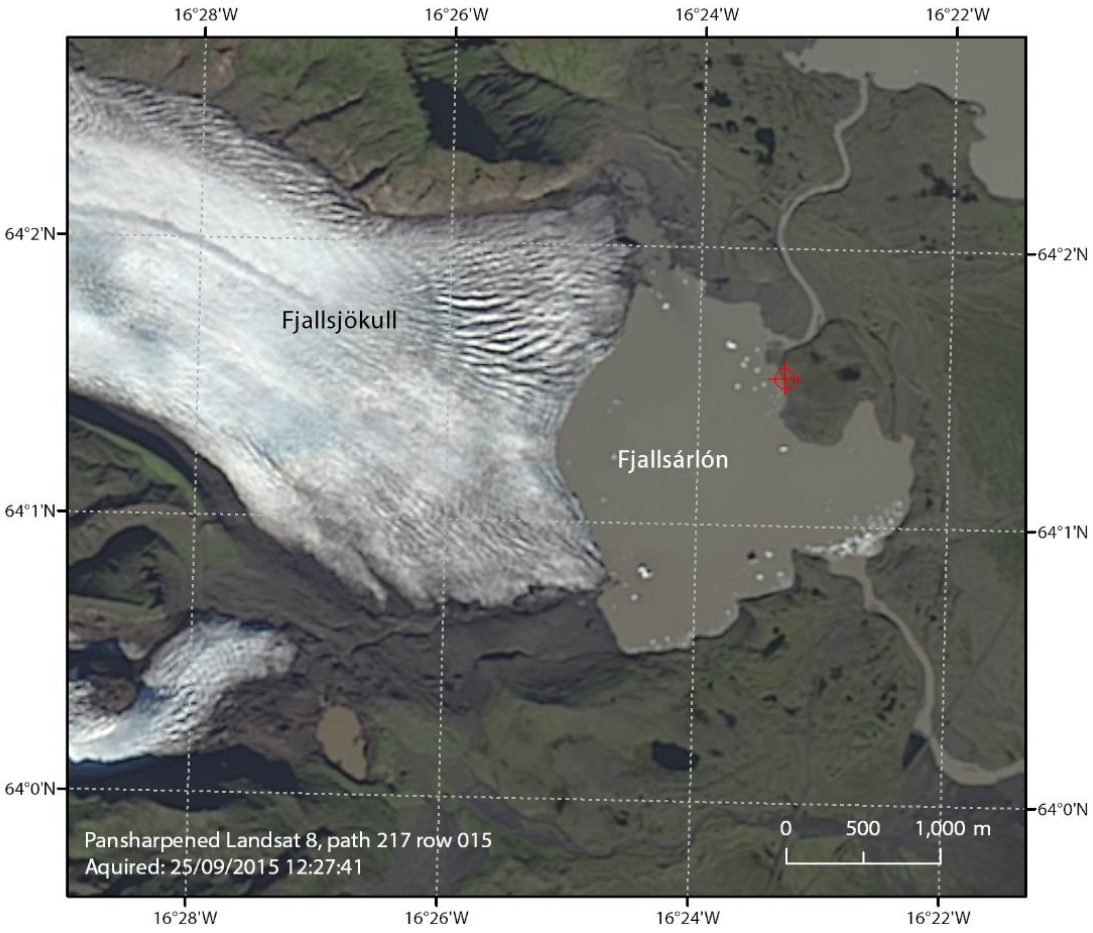

Figure 5.2) Satellite image of Fjallsjökull showing the heavily crevassed surface near the terminus. Red target shows the location of the TLS.

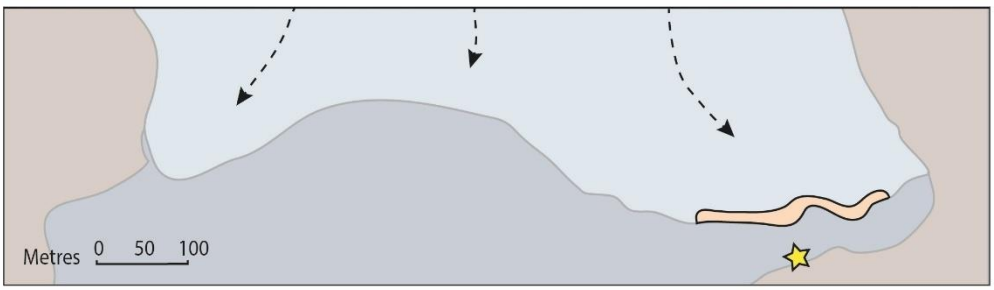

Figure 5.3) Sketch of the large scale geometry of the terminus of Fjallsjökull as of August 23rd May 2016 drawn from Landsat data. Yellow star marks the location of the TLS system. Black dashed arrows are approximate flow lines.

5.1.2 Glacier velocity

Glacier surface velocities were obtained through direct cloud-to-cloud comparison (C2C) in Cloud Compare (see *Section 4.5.1*). Total daily velocities are presented which consider the deformation of the intact glacial ice mass. The mean velocity of the section of terminus monitored at Fjallsjökull was 0.15 m d^{-1} between 17:30 on the 13th August and 17:30 on the 14th August. The highest velocities (1.0 m d^{-1}) were seen in a faster flowing section of the terminus nearer to the glacier centreline, thought to be terminating in the deepest part of the lake. Although velocities were generally consistent across the terminus, at between 0.1-0.2 m d^{-1}, some areas of the ice cliff adjacent to the where a calving event occurred on the 13th August reached 0.6 m d^{-1}, possibly indicating a wider glacier response to calving events. Furthermore, there were some localised velocities of up to 1.0 m d^{-1} in the same area, as observed in the velocity maps, but also in the swath-profiles which appear to be linked to 'flake' calving from the cliff face (Kirkbride & Warren, 1997) and could show the movement of flakes of ice prior to toppling outwards from the ice cliff. Localised velocities of 0.1-0.4 m d^{-1} are observed in areas which also calved during the survey. Figures 5.4 and 5.5 show the velocity characteristics of the terminus in more detail.

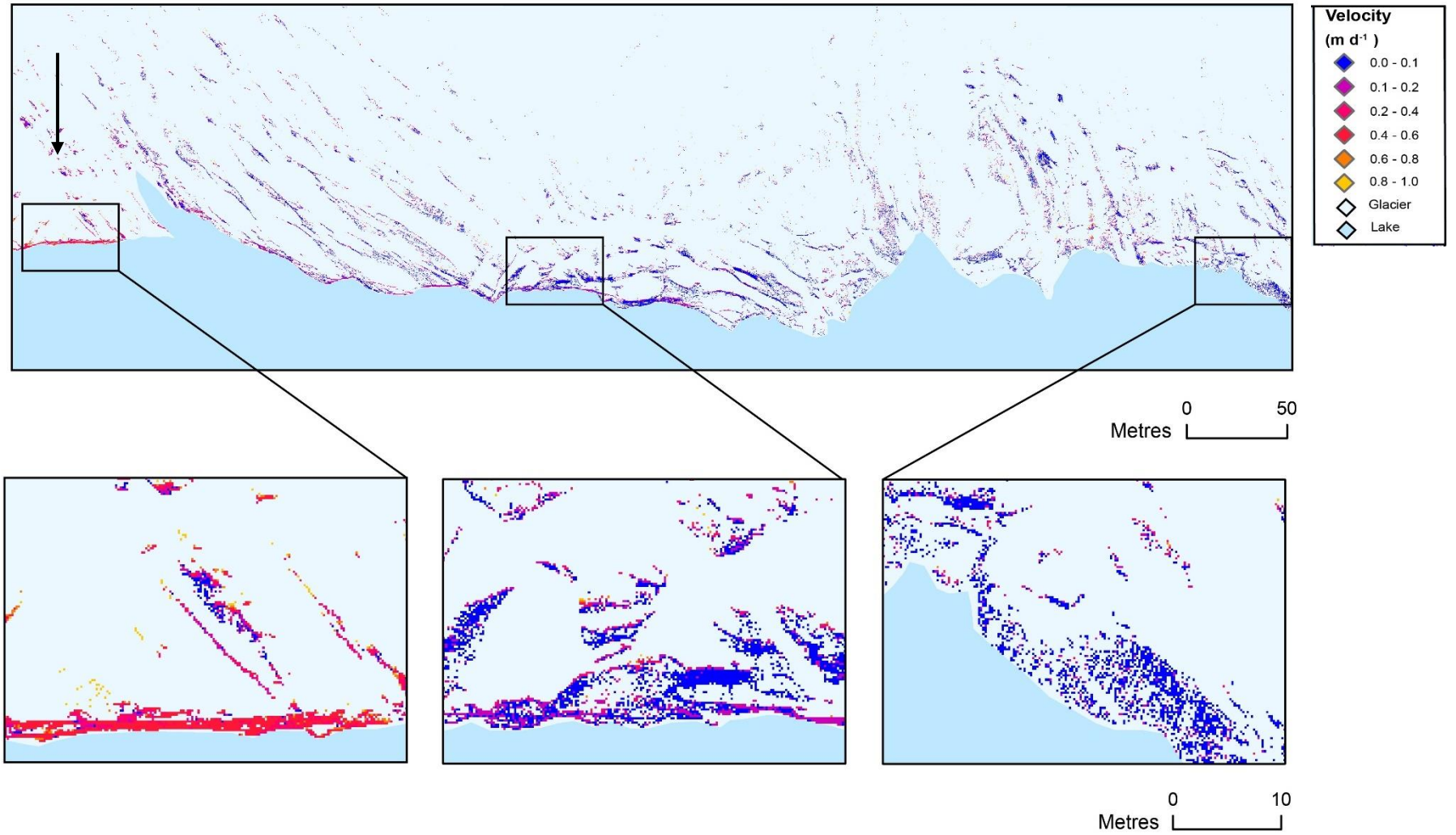

Figure 5.4) Velocity map displaying raster data in plan-view of the terminus. Coloured points show where data between two survey epochs is present. The movement of points is in the *x*-axis, normal to the ice cliff over a period of 24 hours between 13th August 1730 and 14th August 1730. The colour of the points indicates the forward movement of the glacier, expressed in terms of a velocity. The black arrow indicates direction of movement.

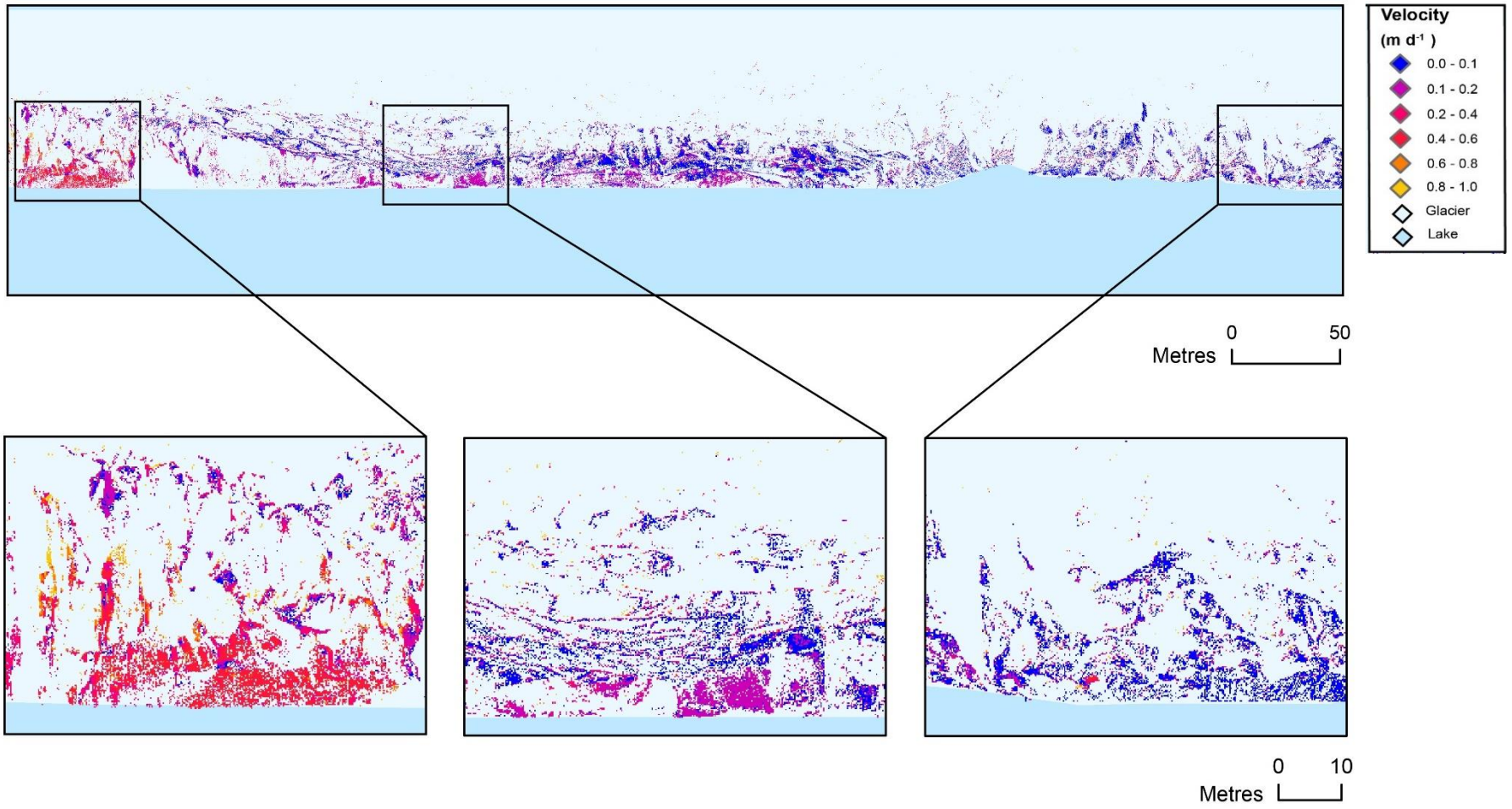

Figure 5.5) Velocity map displaying raster data in cliff-normal elevation view of the terminus. Coloured points show where data between two survey epochs is present. The movement of points is in the *x*-axis, normal to the ice cliff over a period of 24 hours between 13th August 1730 and 14th August 1730. The colour of the points indicates the forward movement of the glacier, expressed in terms of a velocity. The black arrow indicates direction of movement.

5.2 Summary statistics of horizontal change in the x-axis

Table 5.1 shows summary statistics of horizontal change for the AOI of the ice cliff for the *x*-axis prior to the edge detection filter for false change was applied. The greatest loss of ice at -49.8 m $^{d-1}$ corresponds to only one grid cell of change. This indicates the spuriously large change values which are located at the edges of glacial features. The maximum value of positive change is 51.2 m $^{d-1}$ is also only representing one grid cell, which is also highly likely to be false change located at an edge on the glacier surface. These values were removed from subsequent analysis with the implementation of an edge detection filter. The mean change at the ice cliff at -0.7 m $^{d-1}$ (taking into account areas of no data) is likely showing that although the overall motion of the glacier is in the forward direction, much of this is balanced out by the removal of ice at the terminus from the two large calving events which occurred between 17:30 and 18:30 on the 13th August. The standard deviation of 2.9 m $^{d-1}$ is relatively low and indicates that the spread of data points are close to the mean, so that although the range of the changes recorded at the ice cliff are great (-49.8 to 51.2 m $^{d-1}$), the most frequent topographic change is actually relatively low in magnitude. Figure 5.6 is a histogram of topographic change over a 24-hour period between 17:30 13th August and 17:30 14th August.

Table 5.1) Summary statistics of the AOI with change in pixel value between 17:30 13th August and 17:30 14th August.

Minimum (m $^{d-1}$)	Maximum (m $^{d-1}$)	Mean (m $^{d-1}$)
-49.8	51.2	-0.7

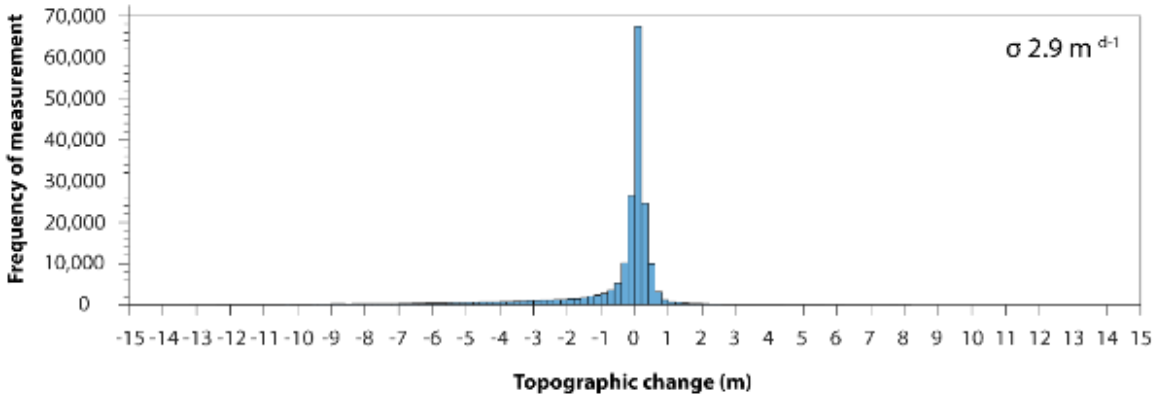

Figure 5.6) Histogram showing topographic change for the clipped AOI between 17:30 13th August and 17:30 14th August. The most frequent change is observed between 0 – 0.2 m indicating that most of this change represents either no change, or forward motion up to 0.2 m.

5.3 Observations from the 2D swath profiles

Three 2D profiles were extracted from 2.5D elevation view DEMs (0.2 m resolution) of the TLS data across the ice cliff of Fjallsjökull for 28 time steps (*Section 4.5.3*). Figure 5.7 shows the position of the profiles overlaid onto the clipped AOI of the ice cliff. Profile 1 is shown in Figure 5.8, profile 2 in Figure 5.9, and profile 3 in Figure 5.10. A further series of 28 individual figures for each profile, one for each time interval is available in Appendix 2, 3 and 4.

Figures 5.8, 5.9, and 5.10 show consecutive profiles over a 24-hour period at intervals of one hour (except 11:47, due to a scanning failure). All three profiles show the progressive forward motion of the glacier over a 24-hour period. Profiles 2 and 3 appear to move forward 5 cm (out of step with the total daily velocity) between 09:30 and 11:47 (even with the lack of scan at 10:30 accounted for). The shape of the cliff as observed on the 50 cm subplots, for all extracted profiles, begins concave with the direction of flow, and ends convex to flow (profile 1 and 3) or flat (profile 2). This change in shape does not correspond to subsidence and uplift of the glacier, but is instead likely due to deformation and the melting of ice at the cliff. All profiles indicate flow of the glacier forward and down.

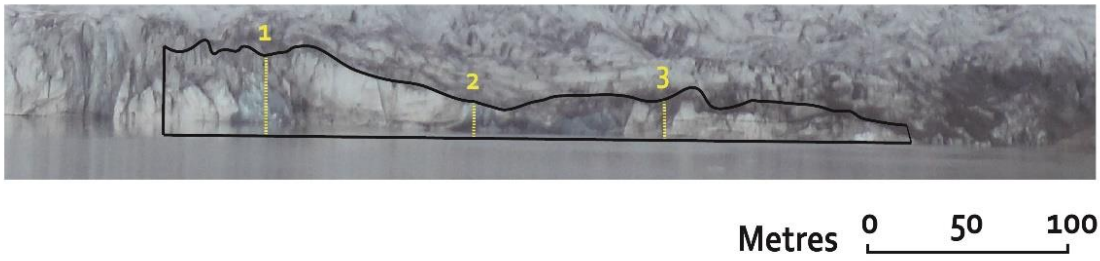

Figure 5.7) The clipped AOI (black line) of the scan data overlaid onto a photo of the ice cliff of Fjallsjökull on the 13th August. The positions of profiles 1, 2 and 3 are marked by a yellow dashed line. The scale is accurate for the AOI.

Profile 1

After the calving event, which is visible from 18:30 onwards on the 13th August, the ice cliff changes to a near-vertical sloping cliff from what had previously been an overhanging geometry (Figure 5.8). Overall, the glacier moves forward by ~40 cm and down by up to 1 m at the top of the ice cliff. There is a section of the cliff at between 17 and 23 m which appears to undergo frequent changes (see also Appendix 3) which are at a greater scale than normal flow; these changes will be discussed in *Section 6.3.3*. The vertical motion, as observed in this profile at the top of the ice cliff, does not show translational movement parallel to the *z*-axis as uniform downward motion in consecutive scans as would be expected from surface melt. Instead, vertical surface change of up to 0.8 m is observed over a couple of hours. This is a widespread phenomenon at the terminus which will be further described in other observations.

Profile 2

After the initial larger calving events on the 13th August, profile 2 (Figure 5.9) is left with an overhanging geometry. Forward motion in this profile follows a sequential pattern of movement which shows that the glacier is moving steadily forward between scans. The overhanging portion of this section of ice cliff begins to bend out from the top of the ice cliff indicating some form of rotational movement originating from the top half of the subaerial ice cliff. Vertical motion at the top of the ice cliff is similar to that observed in profile 1, and does not move steadily downwards as expected, but shows surface uplift at an hourly scale.

Profile 3

Profile 3 has an overhanging geometry (Figure 5.10). Forward motion in this profile follows a steady consecutive pattern, but there does appear to be some rapid motion between 09:30 and 11:47 when the ice cliff moves forward by ~8 cm in the time between scans (missing scan at 10:30 taken into account). Retreat is greater than forward motion in the *x*-axis at the base of the cliff, due to the gradual and persistent nature of this retreat this indicates melt as a mechanism for ice loss, rather than calving at the base of profile 3.

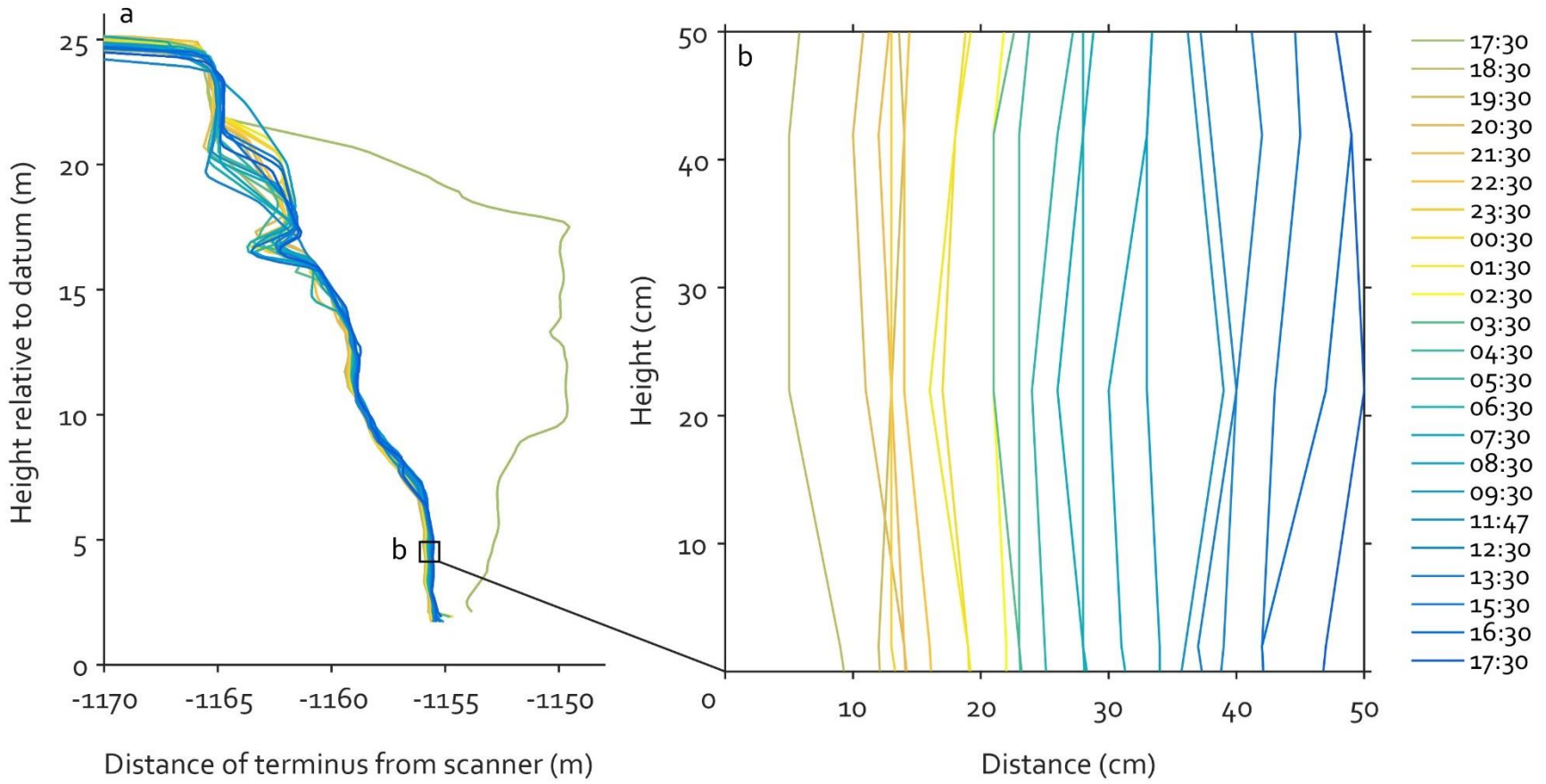

Figure 5.8) a) Profile 1 of the ice cliff at hourly intervals over a period of 24 hours between 13th August 1730 and 14th August 1730. A calving event is seen at 18:30, followed by the steady forward deformation of the ice cliff. An area of spurious change is observed between 15-20 m, which is likely due to a variable point density between scans, or returns from a chaotic and evolving surface. b) Subplot of the ice cliff. The translational motion of the ice cliff is observed, with forward deformation in the order of 0.01– 0.5 m per hour. The profile of this cliff near the toe evolves from being concave to flow to being convex to flow over a 24-hour period indicating the forward bending of ice above the cliff toe.

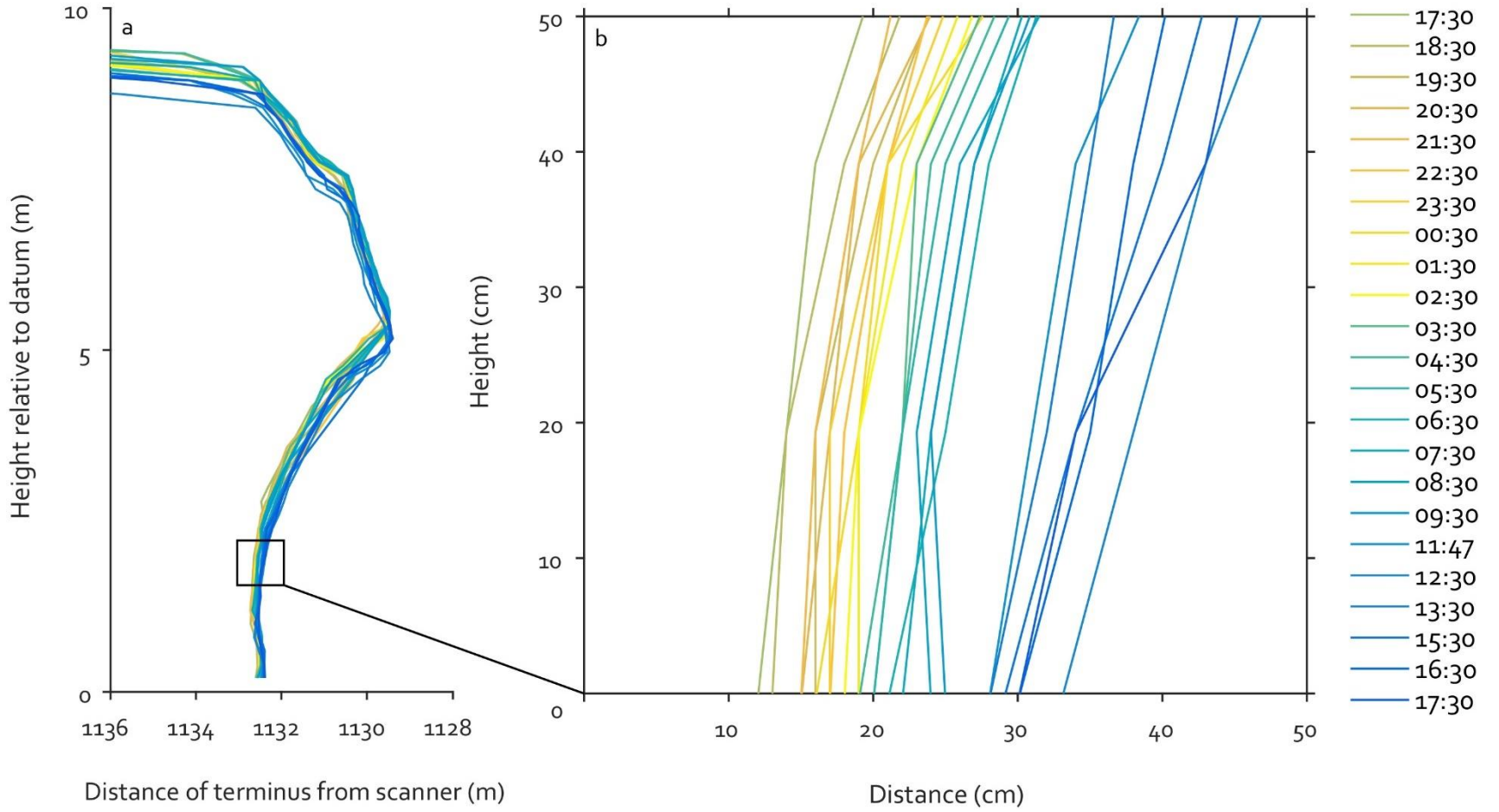

Figure 5.9) a) Profile 2 of the ice cliff at hourly intervals over a period of 24 hours between 13th August 1730 and 14th August 1730. The profile shows rotational deformation of the ice cliff, with the glacier ice deforming forward and down from the crest of the ice cliff. b) Subplot of the ice cliff. The zoomed profile shows that as with profile 1, the glacier ice begins convex to flow (after a calving event) and develops a flatter profile over the 24-hour period.

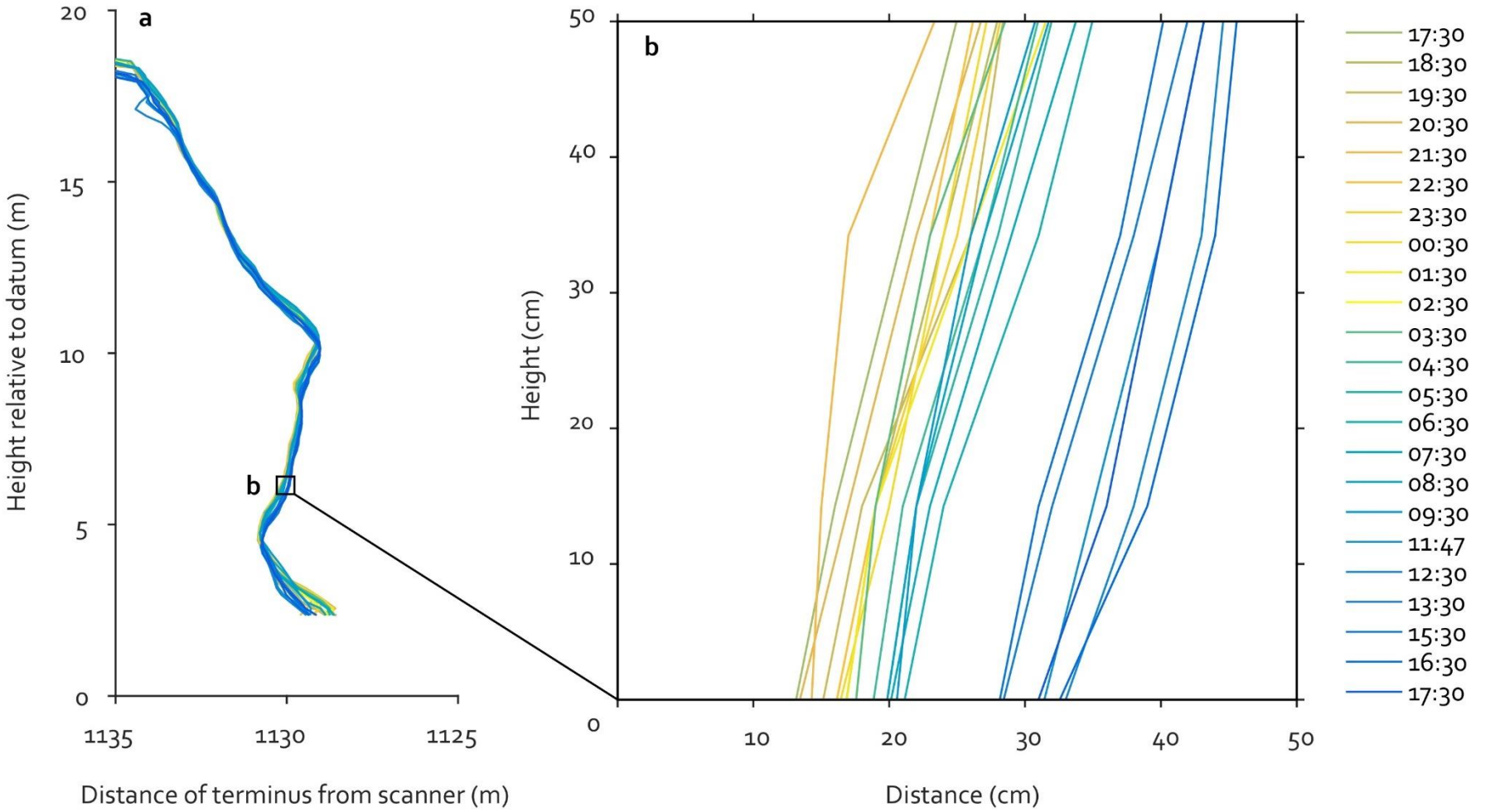

Figure 5.10) a) Profile 3 of the ice cliff at hourly intervals over a period of 24 hours between 13th August 1730 and 14th August 1730. This profile shows a steady surface lowering, and also the forward motion of the ice cliff, though at a lower rate than profile 1 and 2. b) Subplot of the ice cliff. Similarly as with profile 1 and 2, the ice cliff goes from being concave to flow, to convex to flow within 24 hours. The gap in the ice cliff profile between 09:30 and 11:47 is partially due to the gap in data acquisition, but it also appears that forward motion accelerates regardless of this, which coincides with rapid surface lowering (Section 5.7).

5.4 2D Swath profiles through calving events

Figure 5.11 and 5.12 show a profile through two calving events which took place between 16:02 and 18:30 on the 13th August 2016 at Fjallsjökull. The profiles have been extracted from 2.5D raster data (*Chapter 4*) and show the interpolated surface of the LiDAR data. Displaying change analysis in this way is useful for investigating the cross-sectional properties of the calving events. For example, Figure 5.11 shows how this calving event undercuts the ice cliff above, a topographic property which would be challenging to distinguish from DoDs alone (Figure 5.14). Figure 5.11 shows how the calving event occurs from the top-heavy crest, indicating that at the single event scale, these two separate calving events have very different geometries.

5.4.1 Calving at the waterline

Figure 5.12 shows profile 2 through a calving event which took place between 16:02 and 17:30 on the 13th August. Between 15:27 and 16:02 a block of ice undercutting the cliff and which appears to extend underwater is calved. There is no evidence of a waterline notch at the sites which calved in photos or scans, however a notch may have been underwater at the time due to fluctuations in the lake level, and also a waterline notch is visible in photos of the glacier at some points along the width of the ice cliff.

5.4.2 Topple calving and precursory deformation

Prior to calving, the cliff profile (Figure 5.11) shows that between 15:27 and 16:02, the section of ice cliff at 8-14 m in height for profile 1 moves forward by up to 0.5 m, at a rate more than the average velocity (0.15 m d^{-1}). Over the next 28 minutes, between 16:02 and 17:30, the upper 15 m of the block to be calved moves outwards by up to 1 m, with the base of the ice cliff remaining unchanged, indicating the initiation of a toppling failure (Kirkbride & Warren, 1997) with rotational movement. It is likely that a crevasse was located behind the cliff edge which is not visible in data due to TLS operating by line of sight. Figure 5.13 shows precursory deformation observed as a schematic diagram.

5.4.3 Rotation of the ice cliff

Rotation is observed in both profiles (Figure 5.11 and 5.12) prior to calving. With calving event 1 (Figure 5.12), the ice cliff rotates forward from the toe, by ~0.2 m prior to the ice detachment. The crest of the ice cliff, and the surface above and extending back from the terminus lowers by a similar magnitude. With calving event 2 (Figure 5.11) the ice cliff first rotates forward from the toe, observed from about 10 m above datum, and then rotates forward from the crest of the ice cliff. A schematic of this rotation is shown in Figure 5.12.

5.4.4 Readjustment of the terminus after calving

Between 17:30 and 18:30, a block of ice is calved at profile 1. After the calving event the glacier moves vertically up by 0.3 m in Figure 5.11. Similarly, with profile 2, the cliff readjusts and settles at about 20 cm above the level prior to the calving event shown in Figure 5.12.

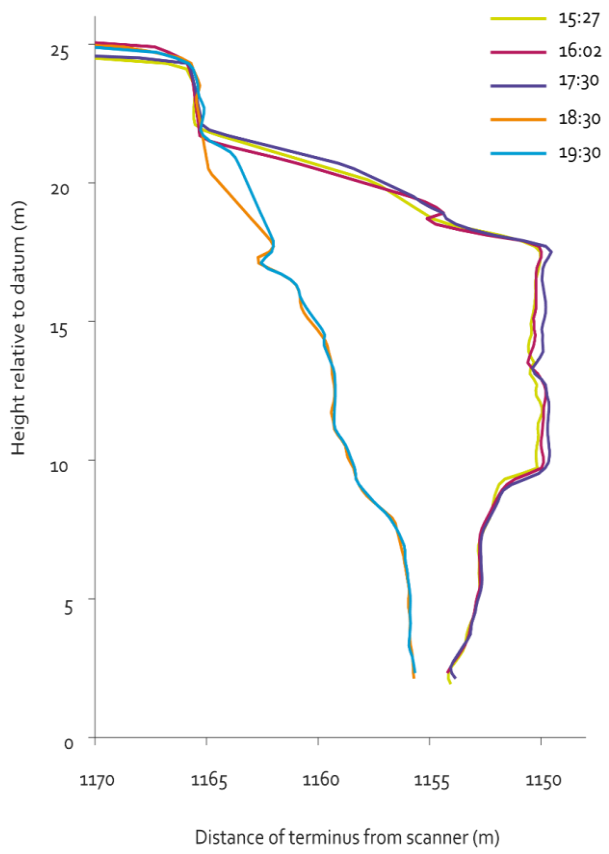

Figure 5.11) Profile 1 through the zone of detachment at hourly to sub-hourly intervals. Precursory deformation and rotation is observed between 15:27 and 17:30 prior to the ice detachment which is visible in the scans from 18:30.

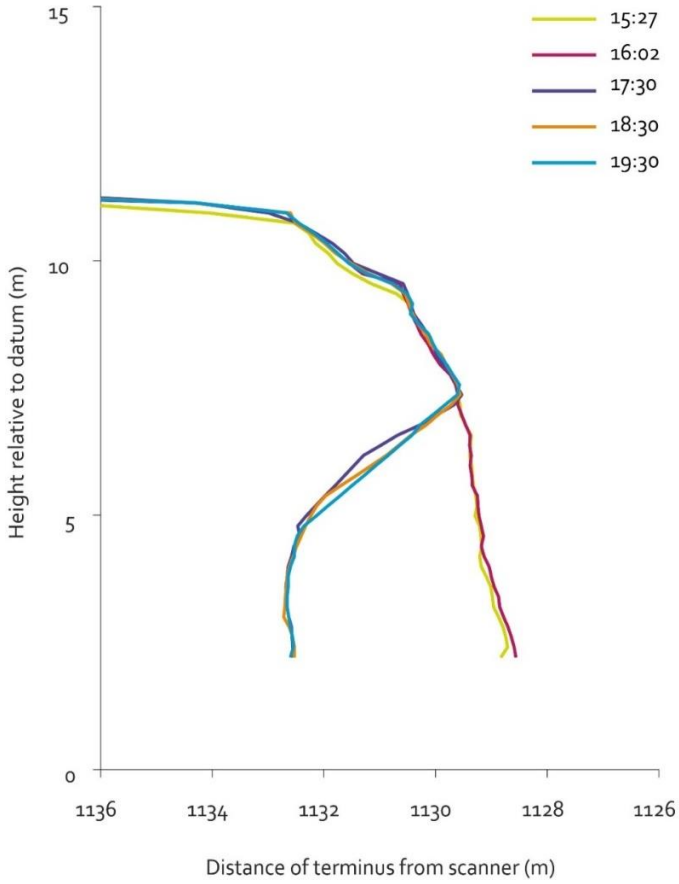

Figure 5.12) Profile 2 through the zone of detachment at sub-hourly to hourly intervals. Rotation from the toe of the ice cliff is observed between 15:27 and 16:02, and forward bending after the calving event that is visible from 17:30 onwards.

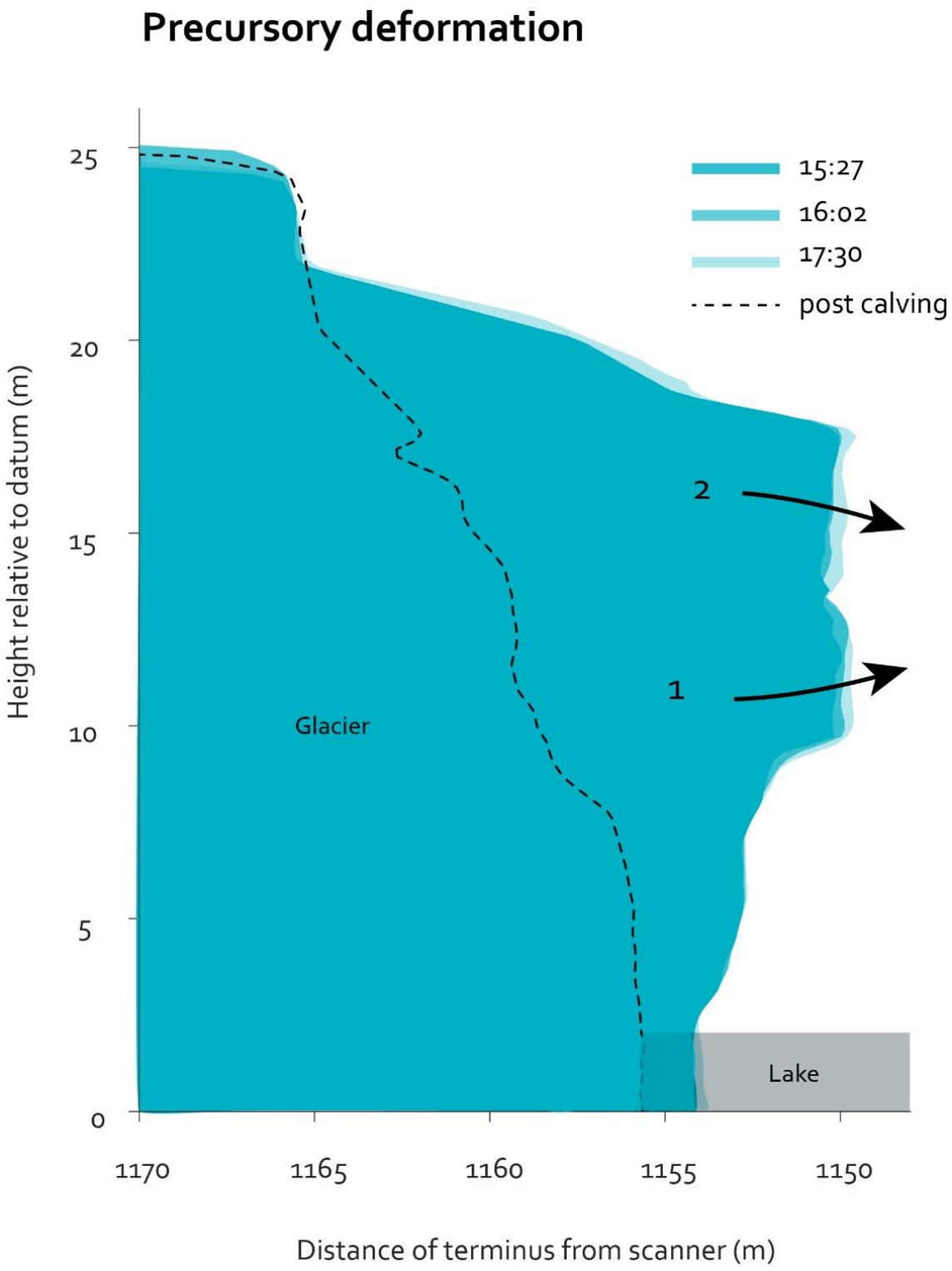

Figure 5.13) A schematic diagram using real data collected at the terminus of Fjallsjökull. The geometry of the terminus is interpolated below the waterline and an area which is likely to be erroneous has been removed for diagrammatic purposes. Heights are relative as opposed to absolute; zero is marked at an arbitrary location. The geometry of the terminus after calving is shown with a black dashed line. The glacier first rotates forward from the toe (15:27-16:02) and then outwards from the crest of the ice cliff (16:02-17:30).

5.5 Observations from 2.5D DEMs of Difference

In order to ascertain the pattern of ice loss at the ice cliff, 2.5D DEMs of Difference (DoDs) were used to assess the pattern of ice loss at the ice cliff of Fjallsjökull between the 13th and 14th August. Hourly to sub-hourly DoDs (Figure 5.14) obtained from sequential laser scans over a 28-hour period show the cumulative pattern of ice loss at the calving face of Fjallsjökull. This method has been used to show patterns of retreat at hard rock cliffs (e.g. Rosser *et al*. 2013). In this section, patterns of calving; the locations of failures and the spatial evolution of failures, in addition to melt driven ice loss, will be presented.

5.5.1 Magnitude/frequency of calving events

Due to the low number of events a magnitude/frequency plot is not given, but the pattern of calving is discussed as follows. The pattern of calving is dominated by two notable (> c. 2.1 x 10^3 m^3) calving events (Figure 5.11 and 5.12) within the AOI. Three large calving events are observed in photography (Figure 5.15), but only two are captured within the LiDAR data. The first of these occurs between 16:02 and 17:30, and the second between 17:30 and 18:30 on 13th August. Prior to both of these calving events, two smaller events (<0.1 x 10^3 m^3 volume visible above waterline only) occur within a period of half an hour of each other and then coalesce with the scars left by the larger events. It may be possible that these two smaller events which are observed above at the waterline, are in fact one subaqueous event, but only two small scars, appearing to be separate events are visible above the water (data of the subaqueous ice cliff would be needed to support this hypothesis). Numerous smaller events (<0.1 x 10^3 m^3) occur but the presence of such events could be underrepresented due to the filtering process used to reduce error in the DoDs (*Chapter 4*). These smaller events tend to be randomly distributed across the calving face. Further to this, subsequent failure over and adjacent to previous failures of ice is also observed.

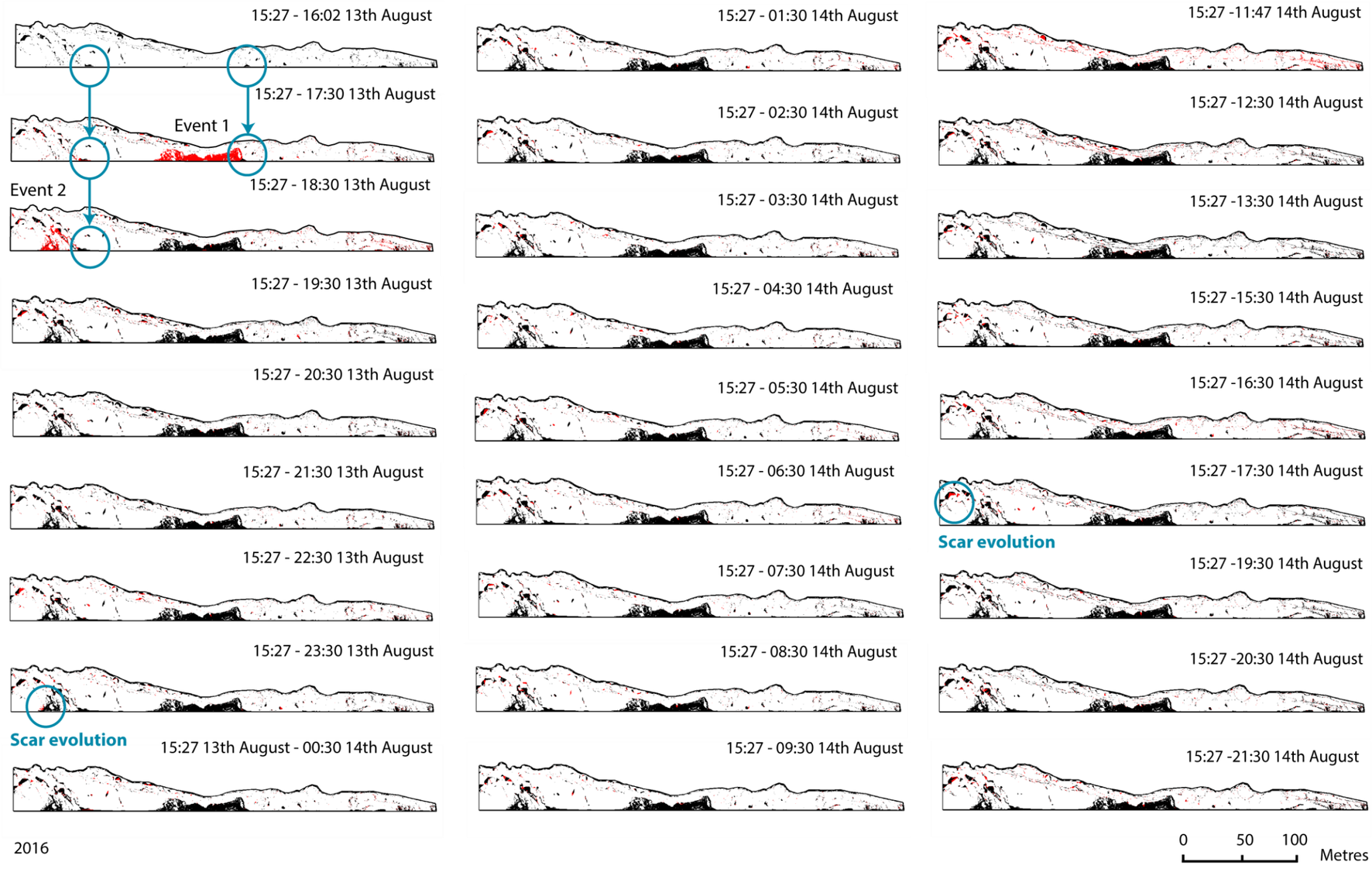

Figure 5.14) DoDs of cumulative change at the ice cliff between 15:27 on the 13th August and 21:30 on the 14th August. Fresh change between scans is highlighted in red, cumulative change is shown in black. Blue circles show the coalescence of sequential failures. With the two larger calving events captured in this dataset, a scar forms at the waterline and then a larger failure propagates up cliff originating from the original scar.

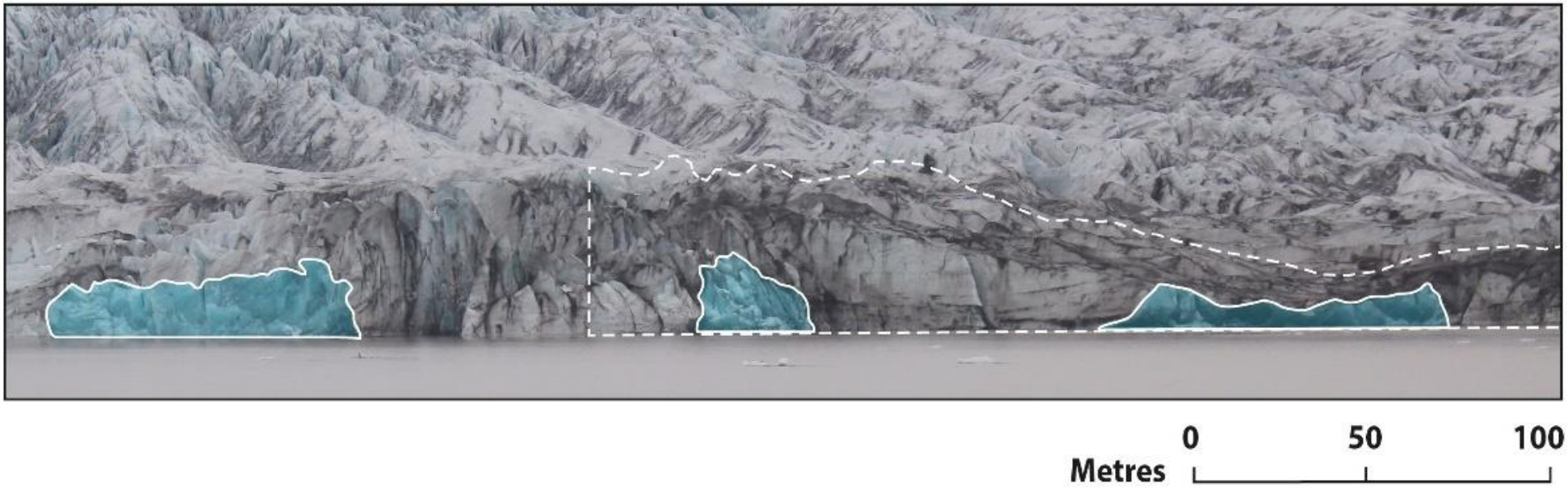

Figure 5.15) The ice cliff of Fjallsjökull at 19:20 on August 13th 2016. The AOI used in the DoDs is shown by a white dashed outline and extends beyond the right of the image. Three calving events are observed in the photo with a white outline and blue fill for emphasis. The scar to the left of the image was not in the AOI of the scans because returns from this part of the ice cliff were too low to give good enough data quality for analysis. The two calving events shown in the image within the AOI are also observed in the DoDs (Figure 5.14).

5.5.2 Spatial distribution of events

The larger calving events are located near to/at the waterline of the subaerial section of the calving face and extend the full height of the calving front. From observing profiles 1 and 2 (Figure 5.11; 5.12), it is likely that the zone of ice detachment extends below the waterline. Smaller events are noted to be widely distributed across the ice cliff and tend to be concentrated in the upper half of the calving face.

5.5.3 Spatial evolution of failures at the calving face

Failures are observed to evolve on sub-hourly to hourly timescales, with larger failures appearing to begin at the waterline with an initially small event, which then propagates up the ice cliff an hour to two hours later (Figure 5.14 blue circles: 15:27-17:30 and 15:27-16:02). Furthermore, there is evidence of scar evolution after larger events (>2.1 x 10^3 m^3), an example of which can be seen at 23:30 (Figure 5.14: blue circle at 15:27 - 23:30).

5.5.4 Melt driven ice loss

Melt driven ice loss at the top of the ice cliff appears to dominate in mid-morning to late-afternoon (11:47 – 16:30) of the 14th as can be seen in Figure 5.14, with widespread and smooth areas of surface change as opposed to defined single events associated with calving. Furthermore, this surface change coincides with a ~2 °C rise in air temperature to 9 °C (Figure 5.23). A reduction in this type of surface change is seen after 16:30 in line with a fall in air temperature of ~2 C at this time (Figure 5.23).

5.6 Zonal statistics of up-cliff change at the ice cliff

In order to consider patterns of change with height up-cliff, the raster data was split into 35 horizontal bands (Figure 4.13), each band was one metre in height and spanned the width of the AOI. The bands were stacked vertically and extended from the toe, to the crest of the ice cliff. Statistics were extracted from these zonal bands and the results are presented below. Patterns which are evident from this data are important in understanding where ice loss is most prevalent, due to calving and melt. Depending on these patterns of ice loss, it may be possible to distinguish why ice loss occurs where it does. For example, the greatest ice loss was seen in the lower third of the ice cliff, near the waterline which suggests that the way the glacier interacts with the lake is important, and that environmental factors such as lake temperature may be driving the ice loss which occurs there. The reasons for the patterns of change which are observed in the zonal statistics are discussed in *Chapter 6*. Zonal statistics were extracted from the 15:27-21:30 13 - 14th August DoD (Figure 5.14) using 1 m up-cliff rectangular polygons. See Table 5.2 below for zonal statistics including area (m), maximum ice loss (m), and mean ice loss (m). Histograms of the vertical up-cliff zonal statistics are also presented.

Table 5.2) Zonal statistics in 1 m vertical bins up ice cliff. Band 1 is at the toe of the ice cliff and band 35 is at the crest of the ice cliff.

Vertical bin (1 m)	Area (m)	Maximum ice loss (m)	Mean (m)
1 (Cliff toe)	364.4	-24.2	-1.4
2	364.3	-24.6	-1.3
3	364.2	-24.6	-1.2
4	364.0	-24.3	-1.1
5	363.9	-22.6	-1.0
6	363.8	-20.9	-0.9
7	361.3	-19.3	-0.9
8	356.6	-19.7	-0.9
9	352	-20.5	-0.8
10	347.3	-20.4	-0.5
11	342.8	-13.0	-0.3
12	337.2	-12.5	-0.3
13	321.9	-12.6	-0.2
14	308	-15.2	0.0
15	286.0	-14.7	0.0
16	262.1	-12.7	-0.1
17	220.3	-15.4	-0.1
18	185.4	-11.3	-0.1
19	155.8	-11.0	-0.2
20	143.9	-12.9	0.0
21	137.7	-12.2	0.1
22	127.8	-13.8	-0.1
23	121.08	-23.8	-0.4
24	118.4	-23.0	-0.7
25	106.6	-22.9	-0.5
26	99.8	-22.2	-0.5
27	97.3	-19.3	-0.4
28	95	-13.6	-0.2
29	93	-25.9	-0.1
30	90.9	-11.2	0.0
31	88.0	-10.3	0.0
32	85.	-5.2	0.0
33	83.6	-15.3	-0.1
34	80.4	-13.1	-0.2
35 (Cliff crest)	66.3	-6.8	0.0

5.6.1 Mean values of ice loss up-cliff

The lower third of the ice cliff accounts for 70% of total volume loss within the AOI. This also correlates to the location in terms of cliff elevation of the two large calving events which are observed after the 17:30 and 18:30 scans. Figure 5.16 shows that the greatest average (mean) change for an elevational band occurs at the very base of the ice cliff near the waterline with a value of -1.4 m (corresponding to ice loss). The magnitude of change reduces gradually with height above water until the middle (elevation) of the ice cliff at 14-15 m where the average change is 0.0 m, indicating that this elevation of the ice cliff is the least active in terms of ice loss. In fact, only 10% of total ice loss occurs in the mid-elevational third of the ice cliff. The volume of ice which is lost from the cliff then increases again between 20-29 m, with the exception of 0.1 m positive change at 21 m, which could be within the mean error (0.11m). The top third of the ice cliff accounts for 20% of mean ice loss. The smallest changes are observed at the very top of the ice cliff between 31 and 35 m.

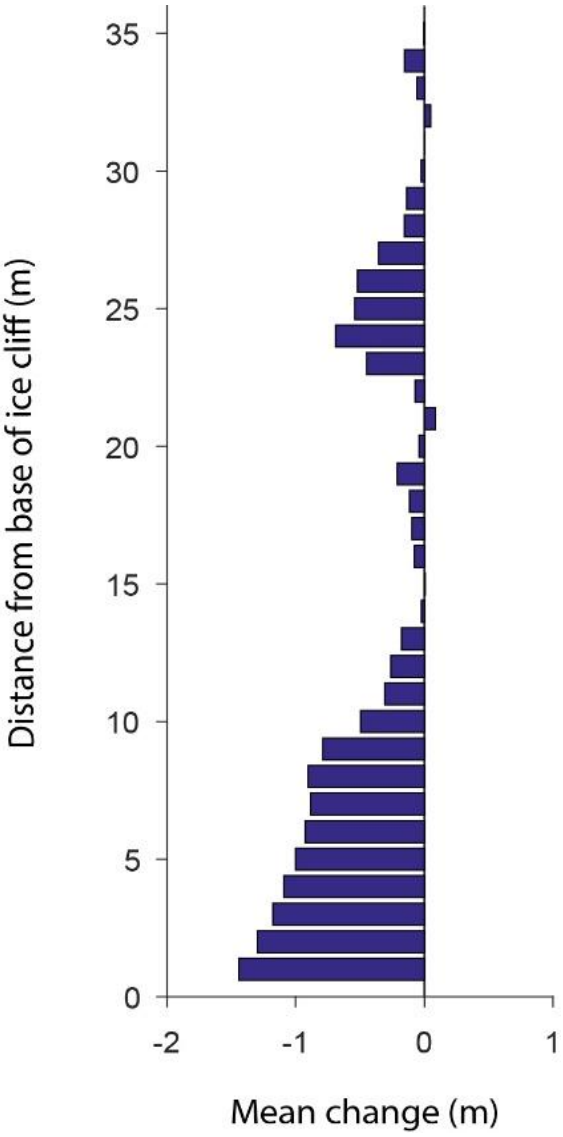

Figure 5.16) Cumulative mean change at the ice cliff between 15:27 on the 13th August and 21:30 on the 14th August. The ice cliff is divided into vertical bins of 1 m, starting at the base of the subaerial ice cliff.

5.6.2 Maximum values of ice loss up-cliff

Figure 5.17 shows that some of the greatest ice losses are seen at the toe of the subaerial ice cliff between 1–4 m above the waterline with up to -24.6 m of change, and then at 23–29 m up-cliff with up to -25.9 m of ice loss. Ice loss is relatively low between 10-20 m where ice the ice loss drops to 11.0 m change which occurs at 19 m above the waterline. The vertical bin with the lowest minimum change is at 32 m above the waterline. There are some spuriously high values, for example minus 25 m of ice at 30 metres above the base of the subaerial ice cliff. These maximum values are likely to incorporate some false change which was missed by the 'false change' filter (*Chapter 4*). This is because when compared to the DoDs, the spatial extent of a calving event, if it were 25 m deep from the terminus, would be expected to be considerable. However, there are no notable changes of this volume observed at the higher elevations of the ice cliff.

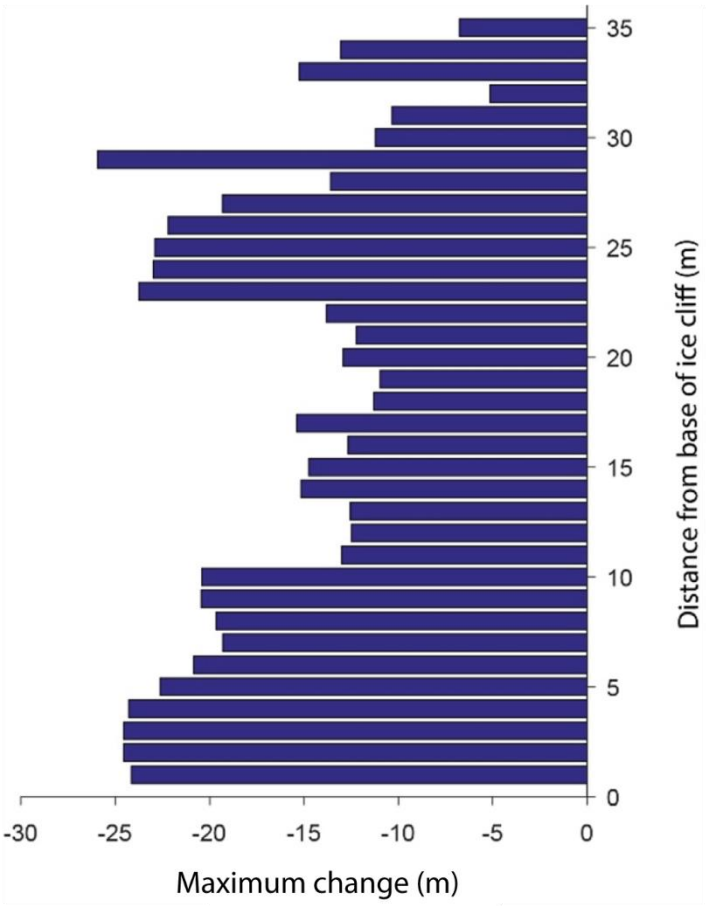

Figure 5.17) Cumulative maximum ice loss at the ice cliff between 15:27 on the 13th August and 21:30 on the 14th August. The ice cliff is divided into vertical bins of 1 m, starting at the base of the subaerial ice cliff.

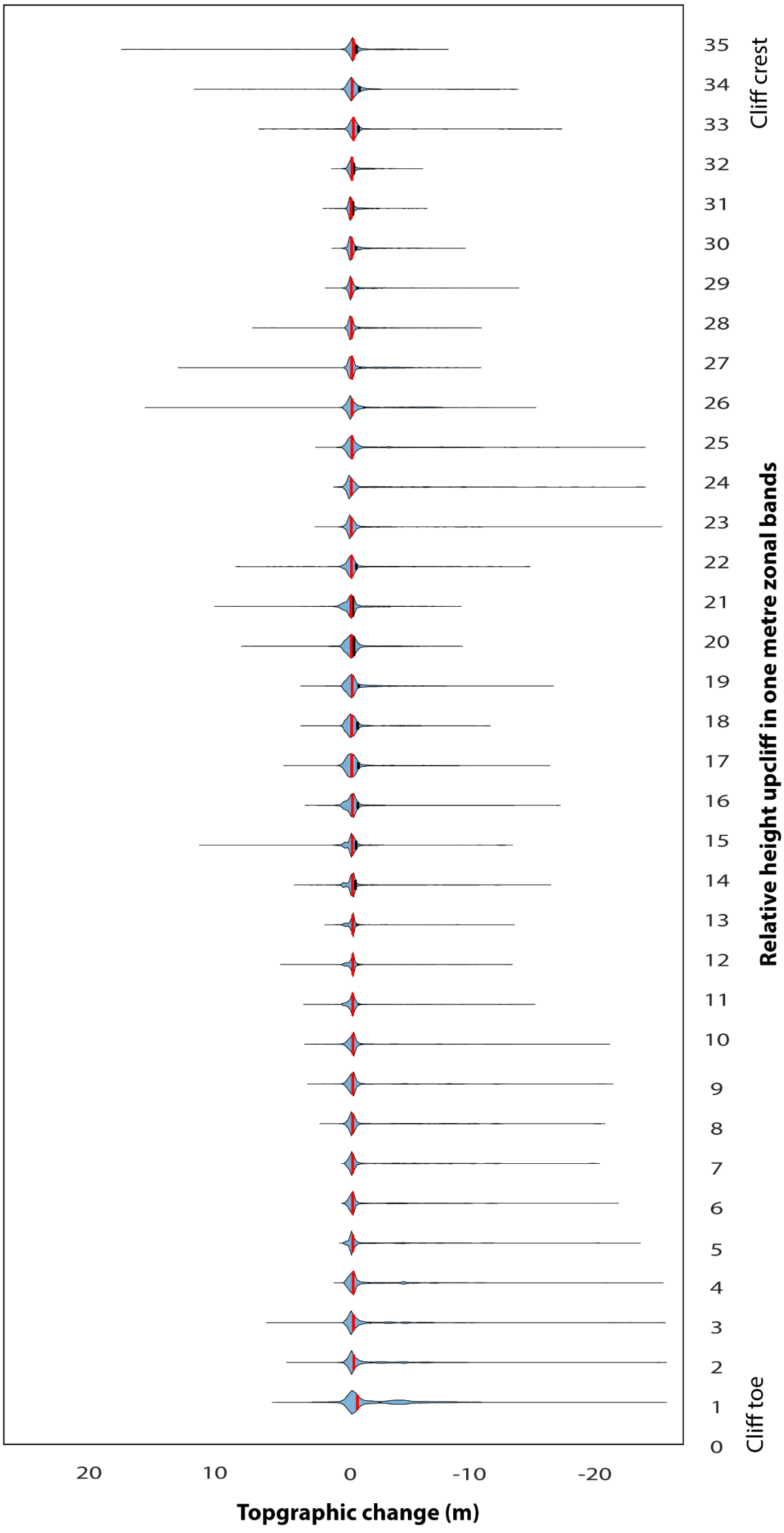

Figure 5.18) Violin plot showing the probability density of topographic change in upcliff bands of 1 metre from the toe to the crest of the ice cliff between 15:27 13th August and 21:30 14th August. The mean for each band is shown as a red line and the median as a black line.

5.6.3 Distribution of topographic change up-cliff

Figure 5.18 is a violin plot showing the distribution of observations of topographic change in one metre bands from the toe of the ice cliff upward to the cliff crest. This figure reveals some interesting trends in the data. At the toe of the ice cliff there is a bi-modal distribution, meaning that although the mean change is -1.4 m, there is still significant forward movement, indicating that the glacier is also moving forward faster at the base of the ice cliff. With height up cliff, a more subdued bi-modal distribution is observed between 2-5 m above the toe. Figure 5.18 indicates that the least active section of the ice cliff in terms of ice loss is between 10-25 m, with ice loss increasing at the very top of the ice cliff in bands 33-35 m. The forward movement of the ice cliff is not uniform with height up cliff over the survey period.

5.7 Vertical displacement at the hourly scale

Widespread surface uplift and rapid subsidence are observed at the glacier terminus across the entire AOI over a diurnal cycle. The key intervals of change are shown in Figure 5.19, the average surface elevation changes across the AOI are displayed in Figure 5.20. The vertical changes show that most of the elevational variability occurred during the day, with a relatively steady elevation held during the night. The average elevation of the glacier is 31.19 m at 15:30 on both days, and rises to 31.52 m at 21:30 on both evenings (Figure 5.20), but the record is too short to confirm if this is a repeating diurnal pattern. The average relative surface appears to rise on both evenings, but the record for the 13th August is seemingly disturbed by the calving events which punctuate (Figure 5.20).

In the early morning of the 14th August, the glacier surface undergoes a rapid (~2 ¼ hour as measured) drop in relative elevation of 0.45 m (average), but up to 0.8 m for some areas of the AOI at some point between 09:30 and 11:47 (Figure 5.19). By 21:30 on the evening of the 14th August, the glacier has again uplifted by an average of 0.55 m across the AOI. The vertical displacement observed does not correspond to any changes in lake level (Figure 5.21), and cannot be explained by ice flux to the terminus for the scale of the displacement observed. The magnitude of the changes, are substantially more than the mean error in the TLS measurements (0.11m).

The melt observed between 11:47 and 13:30 on the 14th August in the DoDs (Figure 5.14) is not distinguishable from the magnitude of vertical surface change observed in Figure 5.20.

This has important implications for high-resolution LiDAR glacier surveys, which will be discussed in *Chapter 6*.

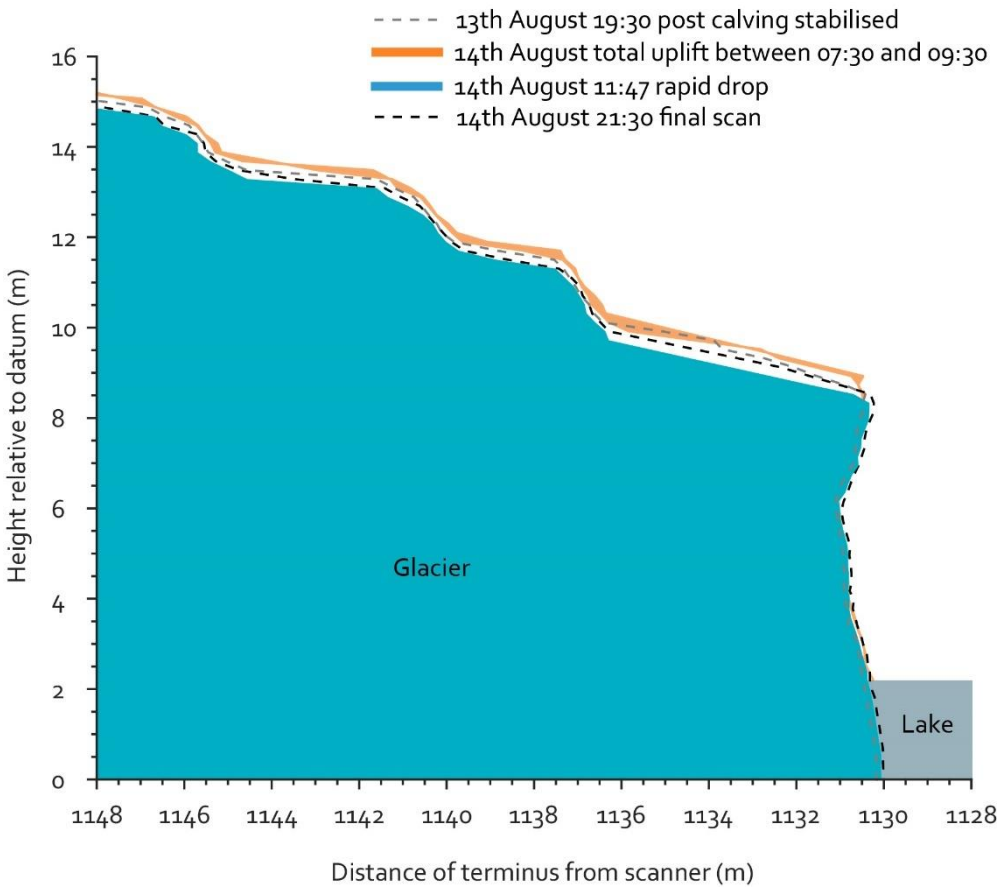

Figure 5.19) Surface uplift at key time intervals for Fjallsjökull on the 13th to the 14th August. Data above the lake are real measurements, geometry of the terminus below lake level is interpolated.

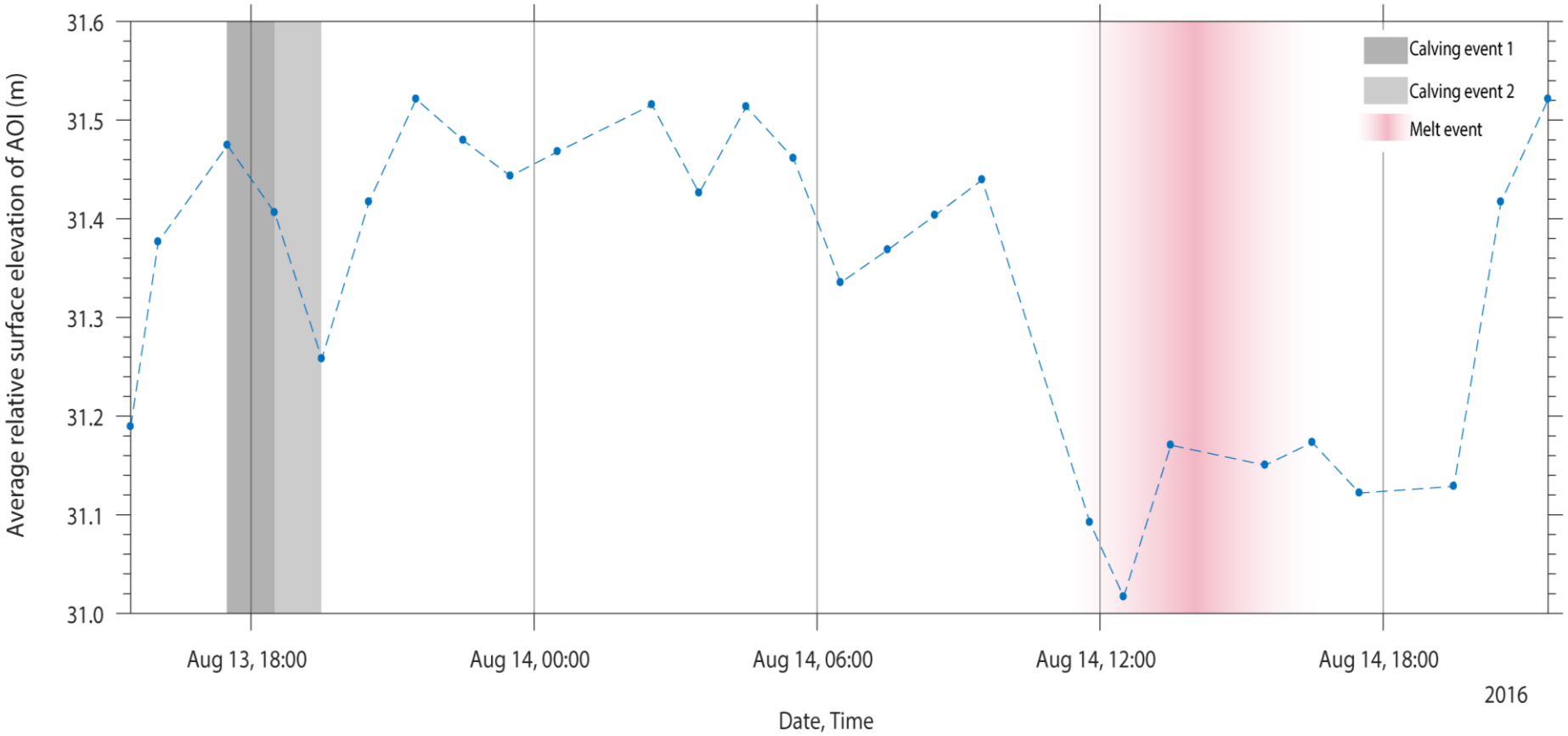

Figure 5.20) Average relative surface elevation over time, between13th – 14th August. Average surface values were extracted from the AOI of plan-view DEMs. Maximum values were used in order to reduce the noise which would be present near overhanging ice cliff geometry at the terminus (Pack *et al.*, 2012). Blue markers show the scan time and the blue dashed line is the linear interpolation between scans. Notable events are draped over the plot, spanning the time between the two scanning events at which they must have occurred. Note, an erroneous data point at 01:30 14th August was removed from the plot.

5.8 Environmental variables and ice loss at the ice cliff

A number of environmental variables were collected during the survey. These included lake level and temperature, time-lapse photographs of the ice cliff and meteorological data. The record of these variables will be presented in turn. The acquisition of this environmental data is important because it will aid the discussion on whether the calving processes observed at the single event scale are driven by environmental factors, are time dependent, or are controlled by internal glacier dynamics (RQ2).

5.8.1 Lake-glacier-interactions

The greatest ice loss is seen at or near the waterline of the ice cliff, but no obvious waterline notch is observed during the scanning survey (Figure 5.21). There also appears to be no link between vertical surface displacement on the hourly scale (Figure 5.20) and the relative lake level (Figure 5.21). An increase in lake-temperature corresponds to the melt observed at the base of profile 3 (Figure 5.10). However, this is also likely to correspond to the increase in air temperature observed in Figure 5.23 in the mid-morning of the 14th August. However, throughout the survey period, air temperatures were consistently greater than the temperatures which recorded were recorded in the lake.

Figure 5.21) Photograph of Fjallsjökull taken on the 14th August 2016, showing that there was no waterline notch at the time of the scanning survey.

5.8.2 Air temperature record

The air temperature record for the survey period is presented in Figure 5.23. Air temperature is an important environmental variable in the case of this study important because it allows the change analysis data such as the DoDs (Figure 5.14) presented earlier in the chapter to be investigated further.

The magnitude of surface elevation changes occur at a greater order of magnitude than surface melt, and therefore melting cannot be quantified in the results (Section 5.7). However, by observing the nature of changes in the DoDs (Figure 5.14) and comparing this to the temperature record, it can be deduced that these changes are most likely due to melting. A widespread, persistent and gradual change is observed in the DoDs at the top of the ice cliff, on the horizontal surface, on the 14th August from 11:47 until 16:30 in the afternoon. During the same period of time the recorded air temperature rises to 14°C as recorded at the Kvísker automatic weather station. It is highly likely that what is observed to be melting in the DoDs (Figure 5.14) is linked to the warm and sunny weather on the morning of the 14th August.

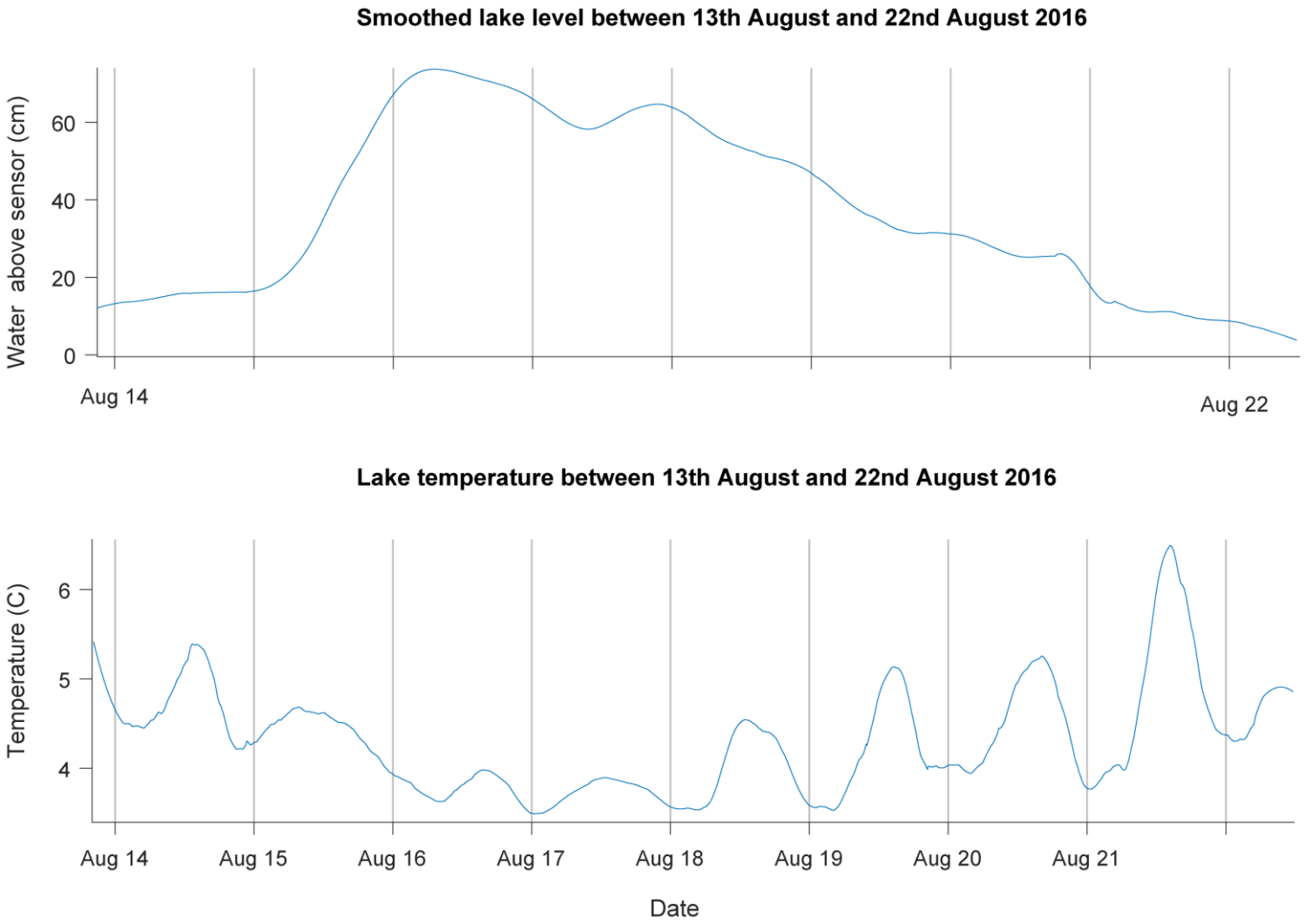

Figure 5.22) Bathymetric diver data for the survey period with grey lines depicting midnight. Both lake level and temperature have been smoothed with a 5% moving average. (a) Smoothed lake level data during the survey period; (b) Water temperature of the lake with diurnal variations evident. The peak water temperature occurs in mid-afternoon and the lowest water temperatures occur around midnight. This pattern is most likely to be explained by increased glacier melt runoff in the late afternoon.

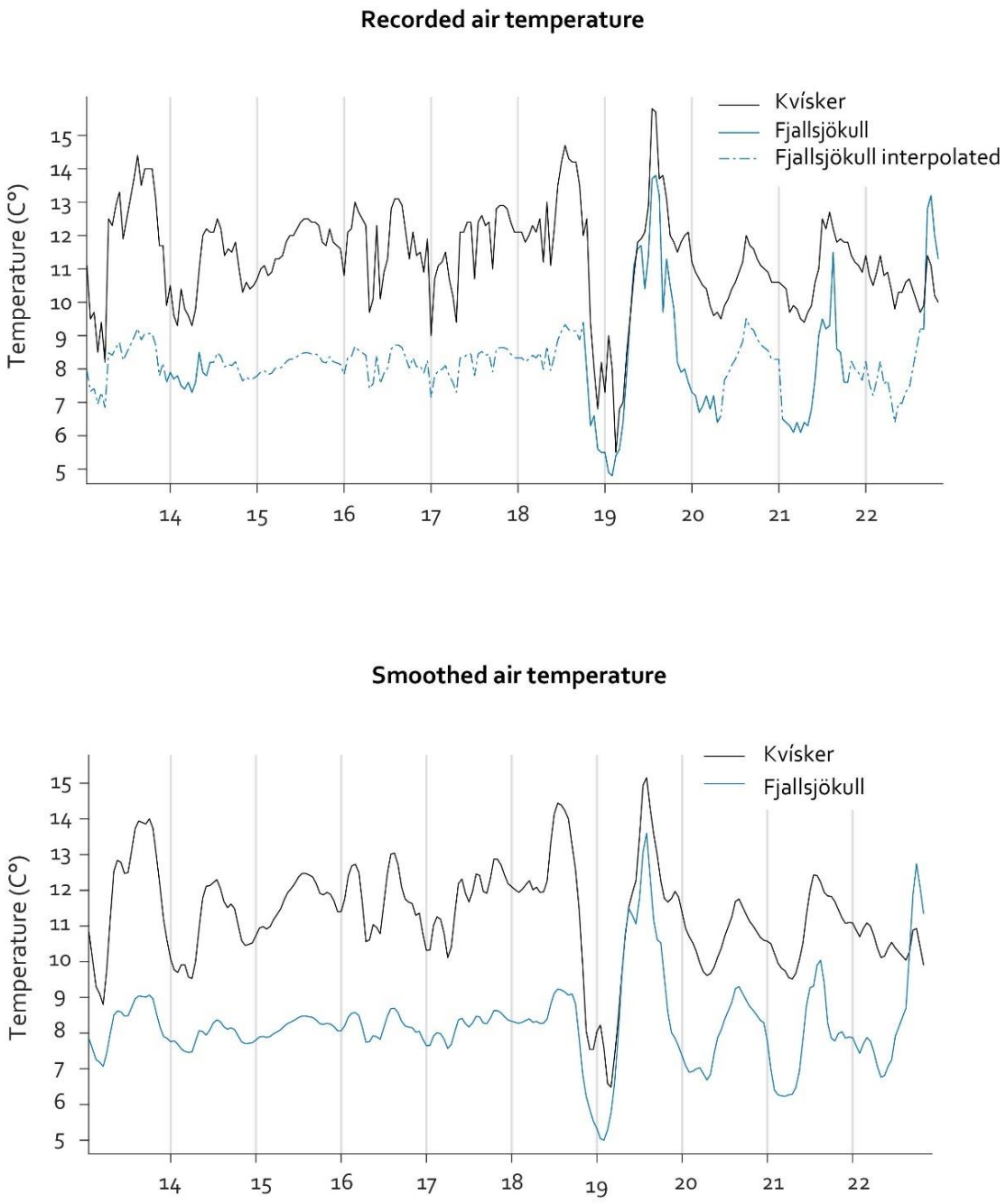

Figure 5.23) Air temperatures on the 13th – 22nd August 2016 at two weather stations; grey vertical grid marks midnight. (a) Recorded air temperatures at Kvísker and Fjallsjökull. Gaps in data collection are filled with linearly regressed interpolation. (b) Smoothed air temperatures using a five-point moving average. The smoothed record for Fjallsjökull uses the interpolated values to provide a continuous record.

5.9 Summary

This chapter has presented the results of the study. First, glacial characteristics such as the surface structure of the glacier and velocities as calculated using the direct C2C comparison method in Cloud Compare were discussed. The mean velocity of the glacier surface was 0.15 m d^{-1} at the time of the scanning survey, with the highest velocities seen nearer the centreline (Figure 5.3 and 5.4).

Next, the spatiotemporal changes at the ice cliff were presented (RQ1). In terms of ice loss, the dominant mode was calving. From observing the DoDs (Figure 5.14) it was shown that events began at the waterline and propagated up-cliff 30-60 minutes later, with the evolution of failures between scans and smaller failures coalescing with subsequent failures. The magnitude/frequency distribution of the calving events which occurred could not be described fully due to the filtering technique which was used to reduce false change in the results. However, it appears that ice loss at the ice cliff was dominated by these two large events (RQ3). The 2D profiles showed the rotational nature and precursory deformation of the failures which occurred at the ice cliff. When considering the cliff in zonal bands with height up-cliff, 70% of total ice volume loss ice loss was focussed at the toe of the ice cliff, and ice loss generally reducing with height up-cliff, though the least active zone was in the middle elevations of the ice cliff.

Some other, perhaps unexpected results which were recorded were the relative surface elevation changes, with uplift and subsidence events of up to 0.8 m occurring on short, hourly timescales. The results then moved on to present environmental variables which will be discussed alongside the results in more detail in *Chapter 6*. In terms of lake-glacier-interactions, it would seem that no waterline notch was present at the time of the survey.

Chapter 6

Discussion

The results of this study (*Chapter 5*) demonstrated that changes at the ice cliff can be mapped near continuously with the implementation of an automatic 3D time-lapse (4D) laser scanner. This chapter will discuss these results and consider how they compare to observations of calving processes discussed in the wider literature. More specifically, the types of motion which are observed and how these are discerned from the LiDAR data will be discussed in Section 6.1, as will the challenges of using TLS to monitor calving, and the considerations that need to be taken when processing LiDAR data obtained from the ice terminus. The spatiotemporal characteristics of calving at hourly to sub-hourly timescales will discussed (Section 6.2) and be compared to the environmental conditions at the time of the survey, and the insight that this gives for drivers of calving processes at the ice cliff also be investigated. Section 6.3 will discuss the methodology, aspects of data quality and offer recommendations for future research in terms of survey design and data processing. Finally, there will be a summary of the topics which have been investigated throughout the discussion.

6.1 Summary of observed motion at the terminus

It is clear that different types of glacier motion are observed over the 28 hour long survey (Figure 5.1). Changes observed at the surface of Fjallsjökull terminus include change either as uplift or subsidence in the *z*-axis (vertical) and change either forwards or backwards in relation to glacier flow in the *x*-axis (horizontal). For horizontal change, both translational and nontranslational (movement that is not uniform or with rotation) are observed coincident and non-coincident with calving events. The different types of motion occur both in alone and simultaneously, making for a complex set of superimposed processes. The details of this observed motion will now be discussed.

6.1.1 Widespread uplift and subsidence of the terminus

A general trend of widespread uplift and at sub-daily intervals, was observed across the entire AOI of the glacier over a diurnal cycle. Further investigation of this record (Figure 5.19) reveals that there are two distinct forms of uplift and subsidence events which are observed at Fjallsjökull. The first example is a gradual change which is not coincident with calving in the AOI. The second example is a more rapid occurrence which appears coincident with calving activity in the AOI. With both examples, such movements could have several origins:

(1) error related to data acquisition or originating from data processing and DEM production that are related to diurnal changes during which scanning was undertaken (Lague *et al.*, 2013; Kromer *et al.*, 2017);

(2) the effects of differential ice flux leading to ice thickening, and thinning, in the AOI (Gabbud *et al.*, 2015);

(3) changes in lake level (Boyce *et al.*, 2007);

(4) torque associated with buoyant forces and readjustment of the terminus after a calving event (Warren *et al.*, 2001; Boyce *et al.*, 2007; Benn *et al.*, 2007b);

(5) sub-glacial meltwater activity, such as the effects of sub-daily hydraulic jacking (e.g. Kulessa *et al.*, 2008);

The mean error (RMSE = 0.11 m) was substantially less than the magnitude of surface uplift, which eliminates the first explanation. An evaluation of the second explanation was undertaken by considering the magnitude of the vertical changes observed in Figures 5.19 and 5.20. If this movement was explained by an ice flux effect, such a change would be expected to coincide with the downstream movement of ice (Figure 6.1). However, these vertical changes do not coincide with any significant downstream displacement of ice in the profiles (Figures 5.8, 5.9 and 5.10), or by a visual analysis of the advection of structural features captured within the point cloud. Both lines of evidence lead to the conclusion that these vertical movements were not the effect of differential ice flux.

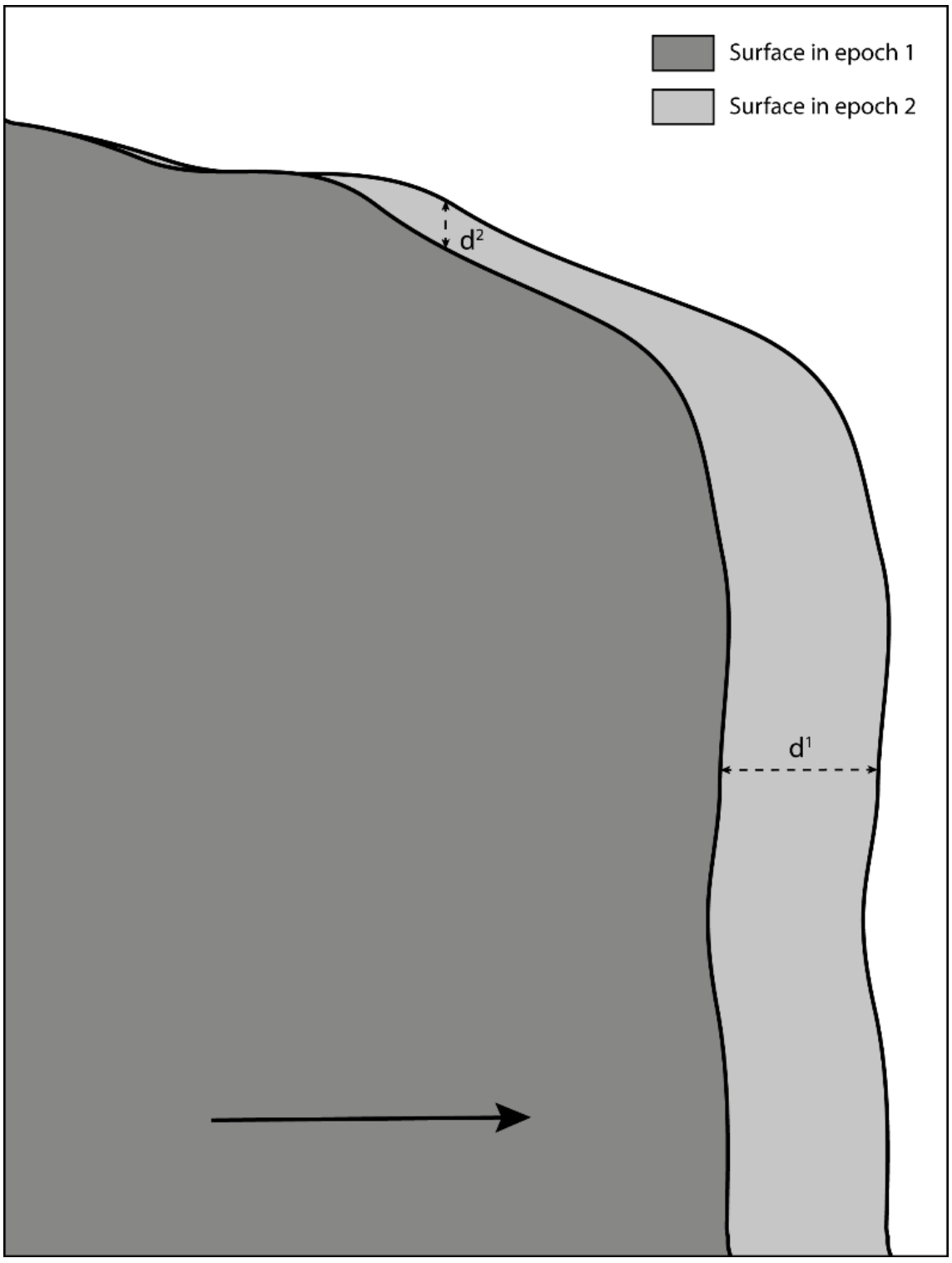

Figure 6.1) Idealised ice cliff showing the effect of ice flux to the terminus. The solid black arrow indicates the direction of glacier flow between the two epochs. The black dashed arrows show the displacement (d^2 vertical and d^1 horizontal) between the two epochs due to ice flux. In this study, the vertical surface elevation changes could not be explained by this effect.

The possibility that changes in lake level (3) might have caused the glacier surface to uplift and subside due to adjusting buoyant forces is not supported. The lake level only rises in the order of <0.1 m over the 28-hour scanning period, which does not correspond to the magnitude of uplift and subsidence (up to 0.8 m) which is recorded across the AOI. For those changes, which are coincident with calving, in the two hours prior and post the detection of the two large calving events on the evening of the 13th, the influence of torque (Figure 6.2) caused by buoyant forces acting on the terminus (4), and thus causing surface elevation changes, is supported by a number of lines of evidence. Firstly, it might be expected that an element of rotational movement would be captured in the record to suggest the upward deflection of the ice cliff around a hinge point (James *et al.*, 2014; Wagner *et al.*, 2016). Indeed, rotational movement around the subaerial base of the ice cliff, likely originating from below the waterline is observed prior to calving (Figure 5.11 and 5.12). Secondly, if calving activity at Fjallsjökull is associated with buoyant forces, it could be expected that the glacier terminus, after losing mass to an ice detachment, would readjust its elevation until a new state of equilibrium is reached. Therefore, the drop in surface elevation (average 0.20 m) which occurs across the AOI after the 16:02 and 17:30 calving events, and the subsequent rise (~0.30 m) of the terminus on the evening of the 13th August could be a record of the ice cliff readjusting to new post-calving conditions. The fact that the rise is greater than the subsidence implies that the mass which was lost due to calving results in increased buoyancy of the terminus after calving (Boyce *et al.*, 2007).

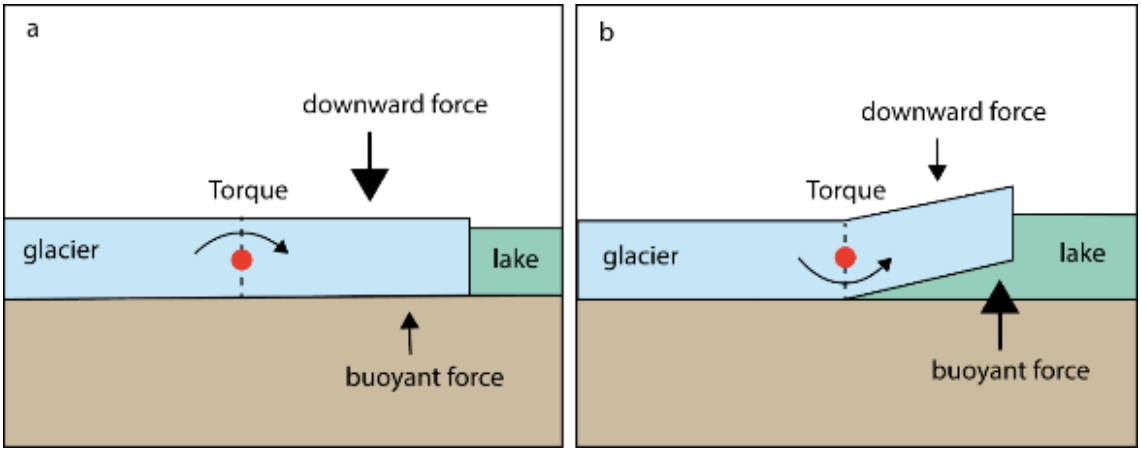

Figure 6.2) Schematic diagram showing the role of buoyant forces and torque at the termini of calving glaciers. a) When glacier ice at the terminus reaches flotation thickness, ice may be held below flotation by torque exerted by the ice front and by the tensile strength of grounded ice to the sides and up-glacier (Van der Veen, 2002); b) when the terminus reaches flotation thickness buoyant forces may exert torque around a pivot point causing upward deflection of the terminus (Boyce *et al.*, 2007).

Subglacial activity (5) could go part of the way to explaining some of the surface elevation changes observed at the terminus which are not coincident with the timing of calving. No significant calving activity was observed in the AOI at this time, but a gradual uplift was observed from the late evening of the 13th August and early morning of the 14th August, which was followed by a rapid drop in surface elevation (average 0.45 m) at some point between 09:30 and 11:47. The vertical changes observed tentatively suggest cyclicity, with most of the elevational variability occurring during the day, and a relatively steady elevation held during the night. The average elevation of the glacier is 31.19 m at 15:30 on both days, and rises to 31.52 m at 21:30 on both days, but the record is too short to confirm if this is a repeating diurnal pattern. However, the results demonstrate that the time of day at which you measure the elevation of the glacier front hold considerable bearing on the result that you will obtain. Therefore, longer-term more epochal monitoring of glaciers is needed to account for this short-term variability.

In support of this explanation, similar sub-daily surface changes were reported from a study which monitored Haut Glacier d'Arolla, a land-terminating glacier in Switzerland, using a Riegl VZ-6000 laser scanner (Gabbud *et al.*, 2015). Measurements from Haut Glacier d'Arolla showed that surface uplift of at least >0.05 m, but more typically ~0.10 m in two hours occurred early in the day after which the glacier surface gradually subsided. The authors suggested that these vertical changes could be due to the measurement of diurnal hydraulic jacking (Kulessa *et al.*, 2008), which had previously only been observed at the seasonal scale (Nienow *et al.*, 1998). This behaviour could be associated with the onset of melting and the localised build-up of subglacial water pressure after partial closure of subglacial channels overnight, and the rapid input of meltwater associated with high levels of insolation and rapid temperature rises. This theory could partly explain the non-calving-coincident changes which are observed at Fjallsjökull. The air temperature record for Kvísker, which is observed to drop by 4°C on the evening of the 13th August, and is followed by a rise in temperature on the morning of the 14th August of up to ~3°C. In order to evaluate the correlation with changes observed, measurements of the subglacial channels using ground-penetrating radar, or subglacial water pressure measured from boreholes coupled with repeat LiDAR surveys would be required.

Taken together, the most likely causes of the widespread uplift and subsidence would be the role of torque and buoyant forces at the termini of calving glaciers, which is well documented in literature on calving glaciers and does support the nature of changes observed at Fjallsjökull (Boyce *et al.*, 2007; Warren *et al.*, 2001). Only a ~300 m section of the ice cliff was used in

analysis, whereas the dynamics of the surface must to some degree be influenced by the full 3D movement and flow of the entire glacier terminus. Notably, the ice cliff was also active to the left of the survey area (Figure 5.15). This means that the glacier could have been readjusting to calving events which occurred to the south of the AOI which were not within the period of the survey. Furthermore, although it is possible to speculate that changes in subglacial water pressure might also be the cause of some of these changes at the ice cliff, it is not possible to demonstrate this unequivocally without further data from the bed of the glacier. In this case, some of the ideas presented above cannot be accepted or rejected, but need further evidence to be fully investigated. There is also no data on where the grounding line is located at the time of the study. It is possible that the terminus of the glacier could be lightly grounded, or partially floating, which could also impact on the uplift and subsidence activity observed at Fjallsjökull.

6.1.2 Rotational motion in the ice cliff coincident and non-coincident with calving

The results have showed that rotation is observed at the terminus. This occurs whereby the toe of the cliff moves forward, but the crest of the cliff moves back relatively, and *vice versa* (Figure 6.3). Both examples of rotation are observed prior to failure. Rotation forward from the toe of the subaerial ice cliff occurs prior to both calving events recorded in the 17:30 and 18:30 scans (the speed at which this process occurs is discussed in Section 6.2.4). This movement is not explained by the advection of surface roughness features (Section 6.1.3), and is greater in magnitude than the RMSE value of the survey (0.11 m), and is therefore assumed to be a true measurement of rotational glacier terminus motion. This rotation could be showing the influence of a hinge mechanism with buoyant forces lifting the glacier up at the terminus (e.g. Wagner *et al.*, 2016). Forward rotation occurs coincident with calving, whereby rotational movement forward from the top of the ice cliff is observed immediately prior to the calving event observed in the scan at 17:30, but in this case it has been interpreted to show the forward toppling of flakes of ice. This observation is supported by photographs which show jagged and narrow vertical segments of ice in this part of the AOI. There is also evidence of forward rotation from the top of the ice cliff in successive profiles which is non-coincident with calving which could indicate forward bending above the waterline, or a surface display of the internal velocity profile.

6.1.3 Translational horizontal motion forward and backward relative to flow

Overall, the movement of the glacier forward or downstream is translational, as would be expected from past observations at ice cliffs (Kirkbride & Warren, 1997). That the 2D profiles of the ice cliff presented in *Chapter 5* follow this translational pattern provides convincing evidence that the errors which are associated with the laser scanning method are indeed less than the motion which can be detected in the *x*-axis. Non-translational change is also observed in the profiles in the *x*-axis, but accompanied by vertical changes (Figure 6.4). When only taking into consideration a small section of a profile, this could appear to be reverse motion of the glacier ice, or melt of the ice surface backwards into the ice cliff when in fact it is the orthogonal movement of surface roughness features (Figure 6.4).

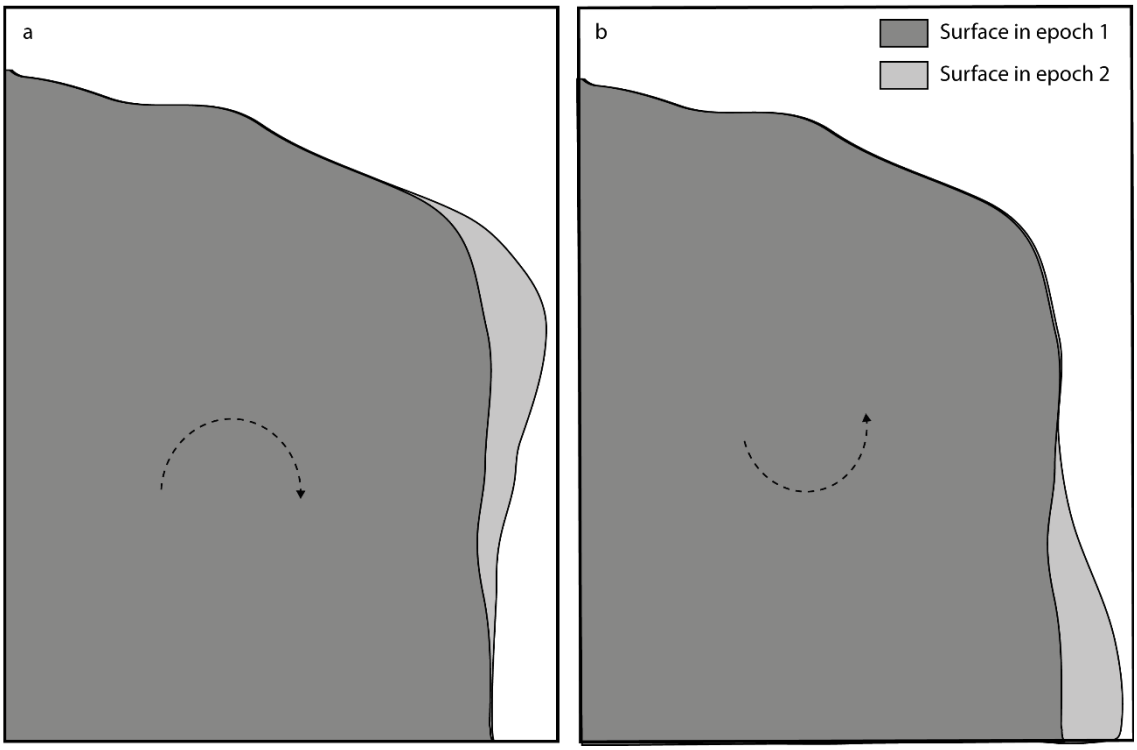

Figure 6.3) Idealised ice cliff showing rotation in two different directions as observed in this dataset. a) The crest of the cliff moves forward, but the toe of the cliff moves backward relatively; b) the toe of the cliff moves forward, but the crest of the cliff moves backward relatively.

6.1.4 Summary

A variety of changes are seen at the terminus from analysis of the LiDAR data, many of which occur simultaneously and are therefore challenging to unravel. However, the key changes which are observed are:

- Widespread uplift and subsidence of the terminus likely due to buoyant forces and perhaps subglacial hydrological activity.

- Rotational motion in the ice cliff coincident with the timing of calving and is observed to occur in two directions. Rotation from the toe of the ice cliff (Figure 6.3b) is interpreted to be an expression of buoyant forces causing the upward deflection of the glacier surface as ice is calved. Rotation from the crest of the ice cliff (Figure 6.3a) is interpreted to be the stretching and outwards toppling of flakes of ice as this area of the cliff fails.

- Rotational motion of the ice cliff which is non-coincident with calving is also observed. In this case, rotation from the toe of the ice cliff (Figure 6.3b) is interpreted to be an expression of the internal glacier velocity profile. When not coincident with calving, rotation from the crest of the ice cliff (Figure 6.3a) is understood to show the forward bending of the glacier in between periods of calving activity.

- Translational horizontal motion is recorded in the dataset. When this movement is forward it is interpreted to represent glacier deformation, and when it is backward relative to flow direction (and without a rotational element) it is interpreted to be melting of the glacier surface.

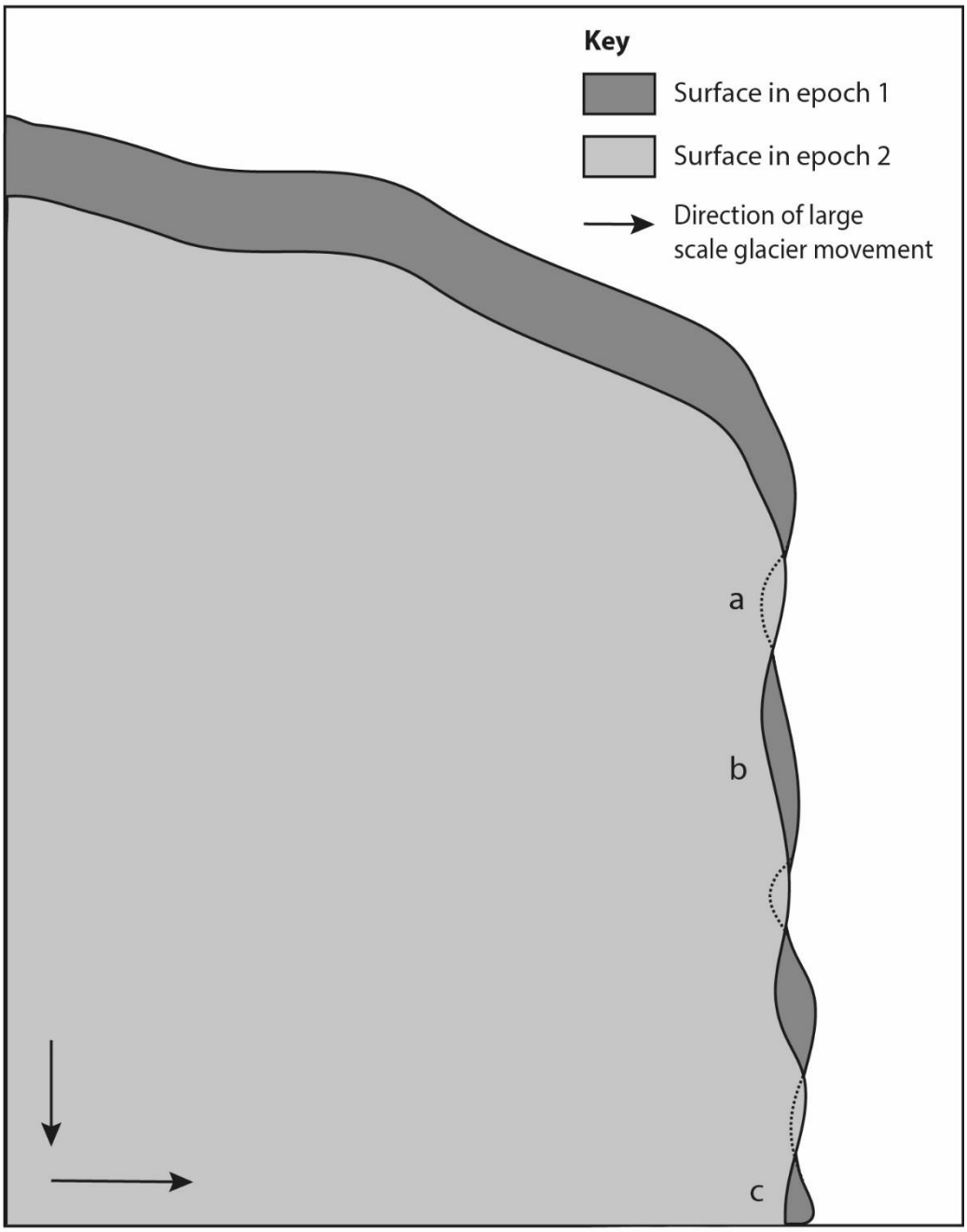

Figure 6.4) An ice cliff showing large-scale movement both forward in the *x*-axis and downward in the *z*-axis. Some examples highlight the importance of considering the surface roughness features on the ice cliff show. a) What could be interpreted as forward motion greater than the true large scale glacier movement, with the advection of a surface roughness feature vertically up or down; b) what could be interpreted as non-translational motion, because of the simultaneous downward and forward motion which does not appear parallel due to the morphology of the ice cliff; c) what could be interpreted to be rotational movement from the base of the ice cliff when not taking into account vertical and horizontal motion occurring simultaneously and the advection of prominent morphology.

6.2 Spatiotemporal characteristics of ice loss at hourly to sub-hourly timescales

6.2.1 Modes of ice loss at the ice cliff of Fjallsjökull

The results obtained from sequential laser scans showed that calving is the dominant mode of ice loss at the subaerial ice cliff of Fjallsjökull over a diurnal cycle. A gradual and persistent change is observed coincident with a rise in air temperature on the morning of the 14th August, indicating melting. It is not possible within the scope of this study to calculate the volume of ice loss attributed with surface melt because the magnitude of associated elevation change is less than the hourly to sub-hourly vertical fluctuations which are recorded across the glacier surface (discussed further in 6.3.5).

6.2.2 General pattern of ice loss at the ice cliff of Fjallsjökull

Cumulative patterns of calving over the survey period (Figure 5.14) display the incremental nature of ice detachment across the ice cliff face. The majority of ice loss in terms of volume can be attributed to two relatively large calving events which occurred on the 13th August. The lower third of the ice cliff, where these two large calving events occurred, accounted for 70% of total ice volume loss within the AOI. Smaller and more frequent ice detachments were observed over the rest of the survey, and were widely distributed across the width of the AOI. However, only 10% of total ice loss occurred in the middle (elevational) third of the ice cliff. The top third of the ice cliff accounted for 20% of mean ice loss, but when comparing this to the DoDs it is likely that a proportion of this activity corresponds to melt rather than calving activity.

Some of the change in the DoDs occurs in the same location as supraglacial debris (Figure 6.5), and also coincides with warm (14°C maximum recorded at Kvísker) and sunny weather on the 14th August. The presence of a thin layer of debris (up to 0.5 cm) is known to increase surface melt on glacier ice, particularly on warm and sunny days due to the lowering in albedo and the increased absorption of insolation to the glacier surface (Östrem, 1959). Therefore, due to the nature of these changes, the most likely explanation is the differential melting of the glacier surface where there is supraglacial debris. Furthermore, ice loss of this nature is not

detected on the vertical ice cliff which is consistent with previous observations which suggest that melt rates of the subaerial vertical ice cliff could be up to 50% lower than the near-horizontal glacier ice at the top of the cliff and further upstream (Haresign & Warren, 2005; Kirkbride & Warren, 1997). Unfortunately, melt cannot be quantitatively distinguished from the data in a reliable way because vertical surface elevation changes occur across the entire AOI which are not due to melting and are of a much greater magnitude. A plot scale study operated on the glacier of surface melt would be required to investigate this further.

Spatial patterns of calving are presented in *Chapter 5* as DoDs with cumulative change (black) and new (within epoch) change (red) in Figure 5.14. Change detection data can be displayed in a variety of ways, and in this study it was decided to display the calving scars on successive individual AOIs for clarity (e.g. Rosser *et al.,* 2007). Such methods are commonly used in the geosciences, particularly for landslide and rockfall monitoring. Alternatively, change at rock cliffs has been presented as colour coded age maps (Vann Jones *et al.*, 2015), but this can have the disadvantage of masking smaller events which are overlaid by larger events during the survey. By displaying each interval separately, it was possible to distinguish the pattern of what could be precursory, smaller ice detachments, and to assess the scar evolution across the face of the ice cliff.

The DoD technique suffers from two major drawbacks (Lague *et al.*, 2013). Firstly, it cannot operate properly on fully 3D areas because a DEM is unable to incorporate overhanging geometry and density information decreases proportionally to surface steepness (Lague *et al.*, 2013). This means that although the overall geometry of the ice cliff is planar due to the rotation of the point cloud, when analysed in this projection there are features which pose a problem for the DEM, such as a waterline notch, the roofs of undercuts and steeply inclined surfaces. Secondly, representing a 3D surface in 2D, unless it is perfectly flat will always result in a loss of information. This is because surface roughness causes occlusions and a DEM will interpolate across this, from which error may arise. The ice cliff at Fjallsjökull was a very rough surface and because of this, when a true change occurs between epochs, the occlusion pattern can change which may introduce artificially large surface changes in places which are then visible from the scanner position (Girardeau-Montaut, 2015; Zeibak & Filin, 2007).

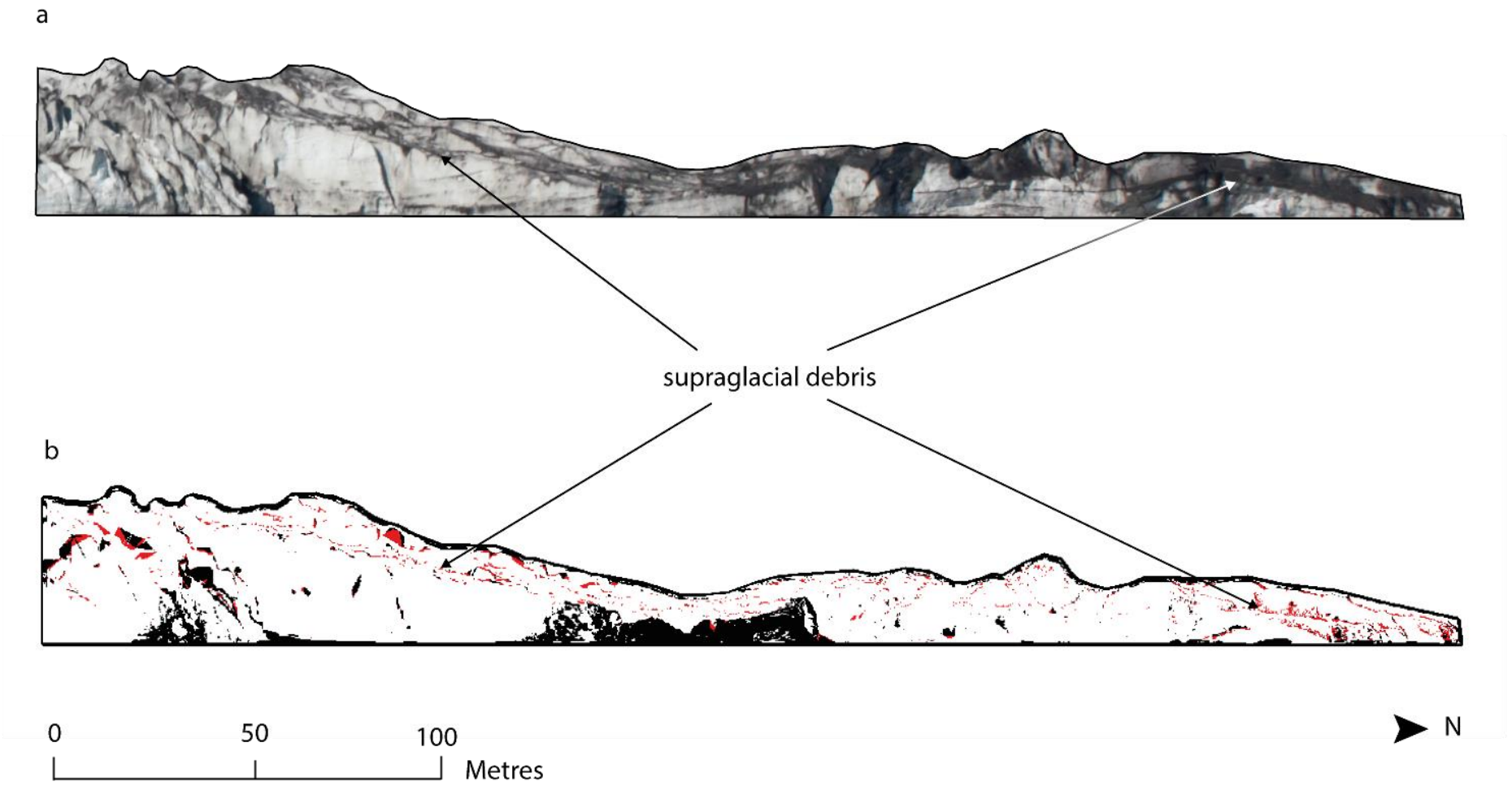

Figure 6.5) a) Cropped photograph taken on 13th August 2017 at 12:00 clipped to the AOI. Note the supraglacial debris which is concentrated on the top of the glacier and is not so dense on the vertical wall of the ice cliff; b) A DoD clipped to the AOI of the ice cliff for 15:27 13th August -11:47 14th August. Areas of ice loss are focussed largely where there the debris is located in photograph (a). Some examples of supraglacial debris have been indicated with arrows in both the photograph and DoD.

6.2.3 Incremental failure at the waterline and up-cliff propagation

Calving events occurred across the ice cliff face, but the two largest events which occurred mid-afternoon on the 13th August appeared to begin with a small failure (<10 m^3) at the waterline which then propagates up-cliff between 30 to 60 minutes later (Figure 5.14). Analysis of the lower third (11 m) of the ice cliff showed that two thirds of total ice loss occurred in this area. Previous studies of lake-terminating glaciers (Kirkbride & Warren, 1997) have identified that the smallest and most frequent calving events tend to occur within about 2-5 m of the waterline and have noted the incremental nature of calving over a number of days or weeks. Kirkbride & Warren (1997) noted that the events occurring near the waterline commonly remove small aprons and pedestals of frozen ice breccia left after large calving events. However, the results of this study indicate that the events which occur in this lower zone of the ice cliff may in fact be precursors, or triggers to larger failures which propagate up-cliff over relatively short timescales only visible with high frequency data, rather than only acting to remove left over ice. It is possible that these events continue below the waterline, and the small zone of calving observed above the waterline is an aerial extension of a primarily subaqueous event. Data of the subaqueous ice cliff would be needed to support this hypothesis. A similar process of progressive failure is observed in hard rock cliffs (Rosser *et al.*, 2013) but this has not been investigated as a process of retreat at such short timescales in ice cliffs because the temporal resolution of surveys is usually too coarse (Petlicki *et al.*, 2015) or the monitoring methods use only semi-quantitative methods, such as human observers, which may overlook such small events.

6.2.4 Sub-hourly to hourly precursory deformation prior to calving

The ice cliff of Fjallsjökull appears to exhibit precursory deformation prior to discrete calving events. This behaviour has been observed in previous studies (e.g. Kirkbride & Warren, 1997). However, although the results from Kirkbride & Warren (1997) and this study both present data from lake-terminating glaciers, the rates of deformation at the ice cliff prior to calving at Fjallsjökull are greater than those which have been measured in other datasets. Kirkbride and Warren (1997) show an averaged ice cliff motion of 0.03 m h^{-1} (originally cited to be 24.6 mm h^{-1} by Kirkbride & Warren, 1997) of the ice cliff of Maud Glacier in the day prior to calving. However at Fjallsjökull, the ice cliff is observed to deform by up to 2.00 m h^{-1} in the immediate hour prior to calving (original data showed that one metre of deformation measured between

17:30 and 18:30, see Section 5.2.4; Figure 5.13) at a rate more than the average velocity (0.15 m d^{-1}/ 0.006 m h^{-1}).

This study has shown that an ice cliff can deform at a rate two magnitudes greater than previous studies have shown in the hours immediately prior to a calving event. These results support the application of a sub-hourly to hourly resolution when studying calving processes, because it may be the case that the values of cliff deformation prior to calving presented in Kirkbride & Warren (1997) were underestimated due to the use of methods available at the time of the study. The values reported in Kirkbride & Warren (1997) may be lower because they were also averaged over a longer timescale, with only an interval of 24 hours available, and based on the assumption and that the deformation rate would be steady during this interval, when instead it speeds up prior to calving. It is also most likely that pre-failure deformation in ice is non-linear, similarly as implied by the dataset collected here from a rock cliff failure (e.g. Rosser *et al.,* 2007).

6.2.5 Calving and the role of environmental variables and time-dependent processes over short-timescales?

Calving is often described as stochastic, with the timing of calving events randomly distributed through time and showing high variability and a non-linear response to environmental variables (Åström *et al.*, 2014; Chapuis & Tetzlaff, 2014). However, data from this study (although limited to only 28 hours) show that the large events occur in the late afternoon of a warm day. The presence of a waterline notch has been suggested as a driver of calving, particularly in a cyclical process of events at the ice cliff (Petlicki *et al.*, 2015; Sugiyama *et al.*, 2016; Kirkbride & Warren, 1997) and they have been observed on other Icelandic glaciers such as Breiðamerkurjökull (Benn *et al.*, 2007b). There was no waterline notch observed in the morphology captured in the laser scanning survey. The lack of a persistent waterline notch can probably be explained by the changes in lake level. Robertson *et al.* (2012) suggested that periods of constant water level and warm surface water temperatures adjacent to ice cliffs are required to allow thermo-erosional notches to develop vigorously. Over a 24-hour period between the 15th and 16th of August, 100 mm of rain was recorded at the Kvísker weather station. Alongside this precipitation, there was a rise in lake level at Fjallsárlón of 0.5 m over 12 hours on the 15th August, which gradually dropped by the same value between the 16th an 21st August (Figure 5.22). The temperature of the surface water in the lake was also reduced during this time, fluctuating between 3°C and 5°C (Figure 5.22). The constantly changing water level

in the lake and thus the changing waterline level at the ice cliff would have reduced the focus or concentration of thermo-erosion at a discrete elevation, which alongside lower surface water temperatures may have led to a lesser development of a waterline notch. A modest waterline notch was observed at Fjallsjökull on the 22nd August, but it was not visible in across the entire AOI. The limited presence of this notch might suggest that there were perhaps localised differences in buoyancy across the terminus at the time it was photographed. Alternatively, a notch may have caused failures irregularly across the ice cliff and was not present because it had not yet had a chance to redevelop (Figure 6.6).

Precipitation does seem to have an effect on the frequency of calving activity although unfortunately this is not quantifiable in this study due to the duration of data captured. Interestingly, from audio observations at the time of rain and fog, the number of calving events heard from Fjallsjökull seemed to, at least anecdotally increase. Furthermore, visual observations showed bergy bits and growlers in the lake the day after the storm on the night of the 15th August. However, to investigate whether there is a relationship between rain and fog, and calving activity, another method such as infrasound would need to be used because laser scanning, nor Structure-from-Motion will acquire data of sufficient quality under these conditions. This was evident by the presence of more bergy bits and growlers in the lake after periods of rain and fog (Figure 6.7). This relationship would be challenging to investigate in

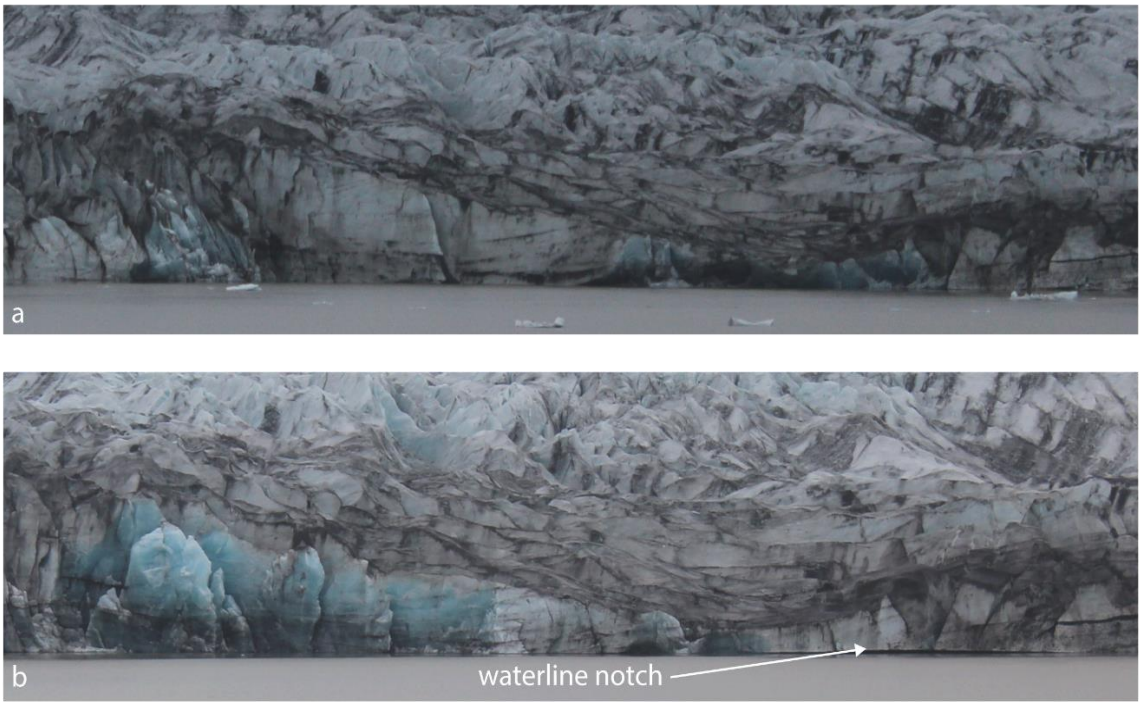

Figure 6.6) a) Photograph of the ice cliff on 14th August at 20:40, note that there is not a waterline notch; b) Photograph of the ice cliff on 22nd August at 08:10, a waterline notch is visible highlighted by a white arrow, but does not extend across the entire terminus.

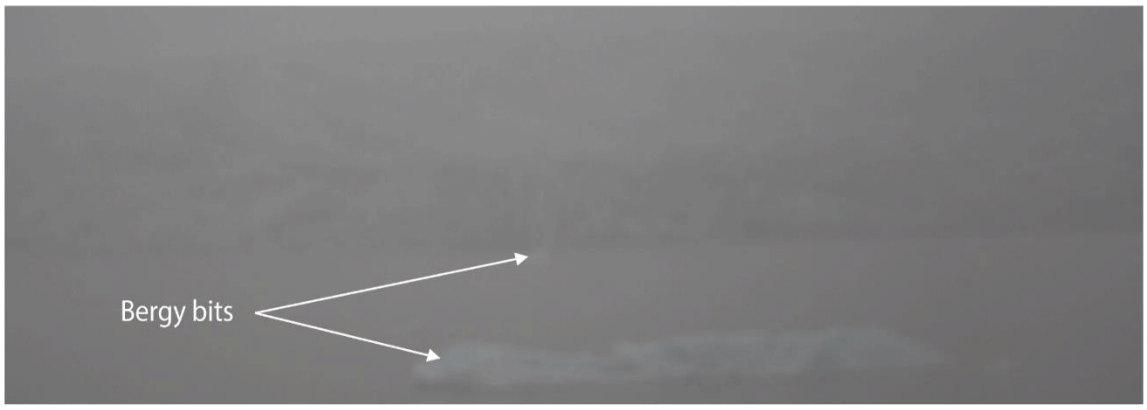

Figure 6.7) Photograph of Fjallsárlón on the 15th August at 20:50. Two bergy bits have been highlighted with white arrows. It is difficult to discern the ice in the lake and the ice cliff, demonstrating how the adverse had on data acquisition.

future studies because it will require a different method of monitoring at the ice cliff. Laser scanning and photography-based imaging are reliant upon visibility (e.g. no fog) and line of sight, and the terminus is obscured during such weather by the poor visibility. The application of audio monitoring (e.g. infrasound) and analysis could be used as a method to investigate this in the future. Given the scale of this study, the role of time-dependent processes would seem to be of importance, with repeat LiDAR at the ice cliff suggesting a progressive nature of failures through time. The two large events are actually composed of multiple events constituting failures over previous failures, with a smaller event originating at the waterline and then propagating up cliff 30-60 minutes later. Alongside this, the results show precursory deformation prior to calving, which is likely to be an expression of internal deformation of the ice, and time-dependent glacier processes such as glacier velocity, and the changing balance of stress at the ice cliff over time.

6.3 Methodology, data quality, and recommendations for future research

This study has demonstrated that a new generation of long-range terrestrial laser scanners such as the *VZ*-4000, are now sufficiently sensitive to obtain reflections from a relatively specular glacier surface at a distance of *c.*1000 m. Where reflections are obtained, the point cloud has an average point spacing of 0.15 m, but coverage is not this dense across the entire survey area (Figure 6.8). Acquisition of spatially rich data at the ice cliff can be obtained automatically and near continuously at hourly to sub-hourly intervals and at a high spatial resolution (<1.0 m). The time taken to acquire a single scan of a 1400 m section of the terminus was 36 minutes, of which a ~300 m section of the ice cliff (the clipped AOI) was used in further

analysis. This data can be used to observe calving processes at the single event scale from successive sub-metre DEMs and to investigate the spatiotemporal relationships between patterns of change and potential calving mechanisms. Although the aims of this study have been met, there have been a number of challenges with the acquisition, processing and subsequent analysis of the data obtained, which will now be discussed for the benefit of future work in this rapidly evolving field.

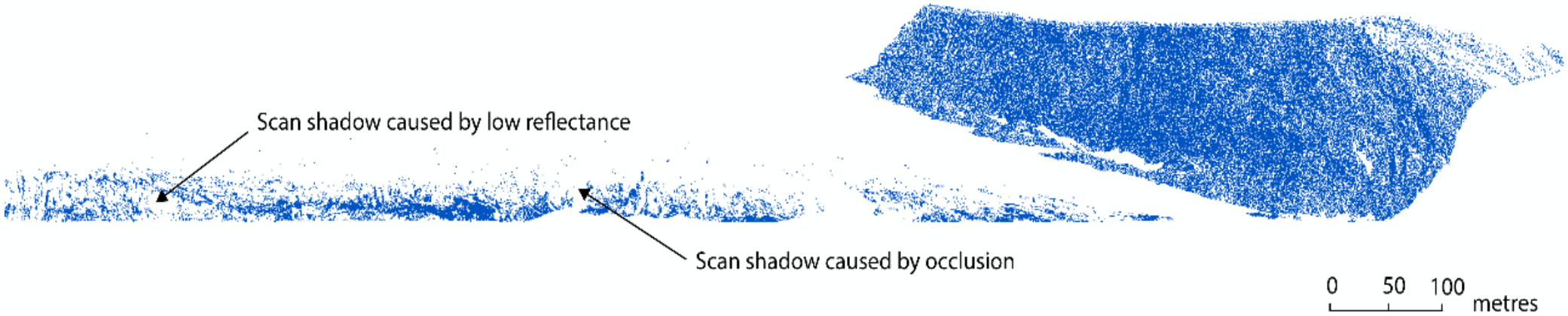

Figure 6.8) Filtered full extent of a LiDAR point cloud of Fjallsjökull with a mountain to the right of the glacier. The point cloud density is greater for the rock surface, and although the point cloud of the glacier area has an average point spacing of 0.15 m, the coverage is not this dense across the entire survey area. Black arrows point to areas of the point cloud which have scan shadows.

6.3.1 Risks to data acquisition using the Riegl VZ-4000

The original intentions of this study were to obtain a week-long, hourly interval LiDAR dataset of the ice cliff. However, this was not possible due to a fatal system error to the scanner after 28 hours of scanning at the fieldsite due to water ingress. Although marketed to operate under challenging conditions such as rain and snow (Riegl Data Sheet, 2015), in reality the VZ-4000 is not as rugged as one might consider. In the case of this study, although the scanner was mounted underneath a tent porch in order to offer protection from the elements, this was not sufficient and resulted in water damage and a costly repair to the instrument. Fortunately, the data were able to be recovered from the instrument before a complete system failure. It was subsequently discovered that when the GPS antenna is attached to the VZ-4000, a small gap is present which had allowed long term water ingress to access the internal components of the laser scanner over a period of months, resulting in its ultimate demise at 04:30 in the morning of the 15th August 2016. Inclement weather such as rain and fog led to poor scan quality and these scans could not be used in the study (Figure 6.9). A similar effect is seen in other TLS studies, whereby the point density is reduced significantly with a high rain intensity (Kromer *et al.*, 2017).

6.3.2 Survey design considerations for a continuous or near continuous TLS survey

The power supply for a laser scanner in a continuous, or near continuous survey, is of vital importance in the planning stage. The *VZ*-4000 operates using intelligent power supply management, and the scanner can be connected to three independent external power sources simultaneously for uninterrupted operation (Riegl Data Sheet, 2015). In this study, the

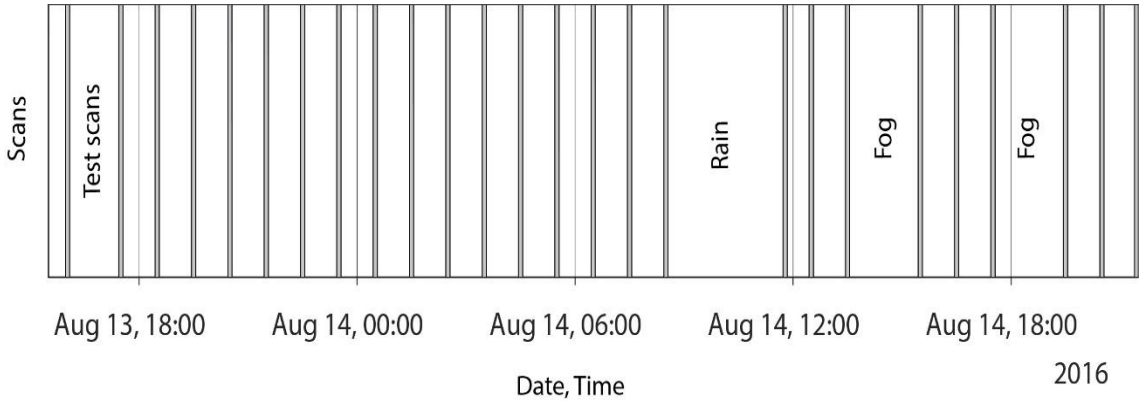

Figure 6.9) Scans collected and the effect of inclement weather of data acquisition. Rain and fog caused data quality to be too poor to use, when this was the case scans were discarded and not used in the study.

VZ-4000 was powered using two batteries and a petrol fuelled generator (Honda 1000i) which were hot-swapped, meaning that the power source was switched without any interruption to operation. The laser scanner would swap to a secondary power source, which was either the second battery or the generator, when the first battery had been discharged of power; and the discharged battery would then be charged while the scanner operated off one of the alternative power sources. The wide external voltage supply range of 11-32 V DC managed any fluctuations in voltage. A permit was obtained from the local authority to undertake work at Fjallsjökull, which included the use of a generator. In some situations this may not be appropriate as it was 53 to 59 decibels when in operation and might constitute a disturbance depending on the location of the fieldsite.

6.3.3 Operating TLS data acquisition from a single scan position

In order to meet the aims of the study, it was necessary to operate the laser scanner from a single scan position. In TLS surveys with multiple scan positions, which tends to be standard practise to overcome occlusion, scan positions are normally overlapping and captured from different angles to the target surface to increase the coverage of the point clouds. Therefore in methodological terms, operating a survey from a single scan position has both advantages and disadvantages for the quality of the data acquired. Increased precision was possible and the data could be acquired at high frequency intervals (sub-hourly to hourly intervals) because the scanner did not need to be moved between surveys (Gabbud *et al.*, 2015). However, this method meant that the choice of vantage point was particularly important in order to reduce the number of occlusions and areas of poor coverage caused by acute angles of incidence.

In particular, error was present at sharp edges and where the angle of incidence was particularly acute, mostly at the edges of the scan pattern (Figure 6.10). This edge effect necessitated the need of an edge detection filter, in order to remove erroneous points from the point cloud prior to analysis. The threshold values for this filter needed to be carefully assessed, so that the maximum amount of false change, and the minimum amount of real change were removed from the dataset. However, it was inevitable that areas of real change were removed from the dataset in this process because these were also located in areas which meet the threshold defined. Furthermore, it was necessary to include areas of stationary bedrock, as fixed objects, within the scanned area in order to ascertain the level of error associated with the survey and the change detection data.

6.3.4 Combining SfM and TLS for improved glacier monitoring

Structure-from-Motion and TLS have both been demonstrated to produce dense point clouds in geoscience applications. Structure-from-Motion has now reached a point where the density of a point cloud is comparable to TLS (Westoby *et al.*, 2012) and much cheaper to operate. However, when SfM is used in change detection applications, issues of shadowing and inconsistent geometry in model reconstruction remain challenging (Fonstad *et al.*, 2013). For similar studies in the future it would be beneficial to operate a combined survey. One of the main drawbacks which has been highlighted in this study, is that although the Riegl *VZ*-4000 is marketed to acquire data from ice at up to ~1000 m, in fact the data can be patchy in coverage. This is because in reality glacier ice, particularly at the glacier terminus can be a complex surface, which leads to acute angles for the laser scanner, and is also often highly unreflective or totally specular. If a survey were to combine TLS for the accuracy of measurements, and SfM to provide an improved coverage, with both point clouds co-registered, it would give a much more complete glacier survey, with the limitation that SfM could only be acquired in daylight hours. The result would be a denser dataset, for which a fuller magnitude/frequency relationship could be described.

6.3.5 The importance of high-resolution sub-daily measurements

Glaciological studies are emerging which apply TLS as a method to investigate glacier surface changes at very high spatial resolutions. Smith *et al.* (2016) present observed topographic changes of the glacier surface of Kårsaglaciären with a three day scanning interval. In light of the results from this study, and that of Gabbud *et al.* (2015), however, an interval of three days may not be appropriate when investigating such small scale surface changes as those observed here. The authors assume that the glacier is vertically stable during the survey, but vertical changes can occur over a couple of hours at a greater order of magnitude than normal levels of surface melt. Therefore, glaciological studies using TLS should take this into account when drawing conclusions based on intervals which are further than an hour apart. Furthermore, because the surface elevation changes in the present study hint at a cyclical pattern, it could be important that the measurements are taken at the same time of day if the interval is daily.

6.3.6 Glacier velocity calculations from TLS

Because the movement observed in the scans which is downstream is mostly translational, velocities were able to be calculated using direct C2C comparison in Cloud Compare. This method was used to calculate change between two epochs as a representation of glacier surface velocity. It is worth pointing out than this method does not account for melt backwards at the ice cliff which might be expected, but also, in reality no melt was observed on the vertical ice cliff (Section 6.2.2). Direct C2C comparison is the simplest and fastest method of direct 3D point cloud comparison and does not require gridding of the data as with DoDs (Girardeau-Montaut, 2015). However, this method is sensitive to the clouds roughness, outliers and point spacing (Lague *et al.*, 2013). The displacement of such surface roughness features could affect the velocity calculations which were performed in Cloud Compare, but it is assumed that this effect is not sufficiently frequent within this dataset to constitute a major source of error, though it would be worth considering in future studies.

6.3.7 What can be learned from hillslope and rockslope studies?

The use of LiDAR at such high spatial and temporal resolutions is a relatively immature application within glaciology, particularly for studying ice cliffs. However, many techniques for the acquisition, processing, and analysis of LiDAR data are already well-developed for monitoring hillslope and rockslope activity. This study has demonstrated that a new generation of laser scanners capable of monitoring calving activity at the ice cliff, and the processes which are observed would not be visible from satellite data. This is because events can incrementally undercut the ice cliff, which then moves forward and so the calving occurs in what is essentially in a blind spot. In photography spanning a month over the ablation season, ice loss was therefore dominated by small-scale events and there were no events large enough that they would have been greater than the pixel size of pan-sharpened Landsat data (15 m) for example. Within coastal studies a similar problem of monitoring the incremental nature of hard rock coastline retreat has been challenged using TLS monitoring (Rosser *et al.*, 2005; Lim *et al.*, 2010). Perhaps this is of even more importance at an ice cliff because glaciers move forward due to ice flux to the terminus whereas this does not happen in rock, which

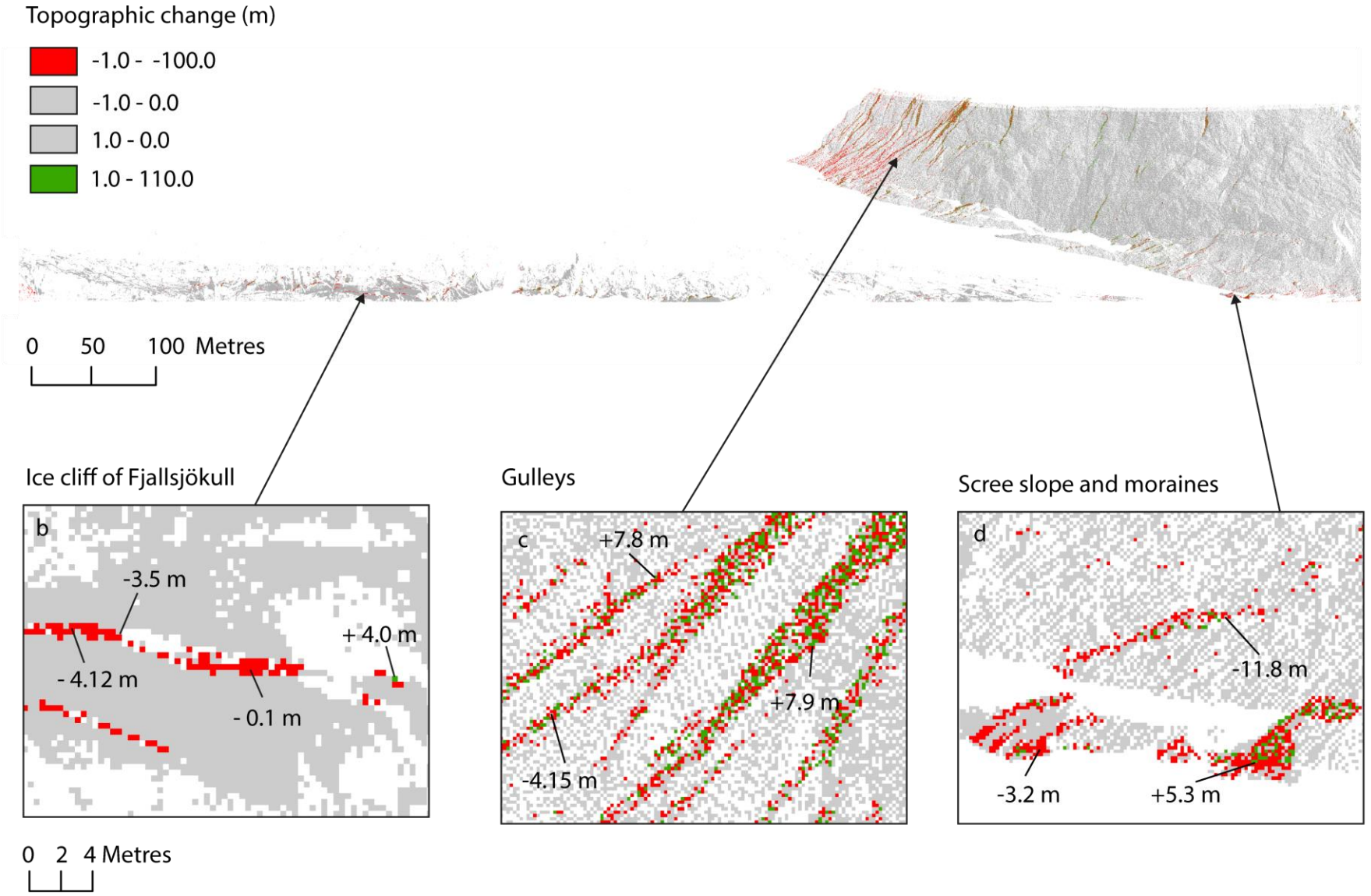

Figure 6.10) a) A DoD of the entire scanning area for 17:30 – 18:30 13th August without clipping or the use of the edge filter. Spuriously high and low change values are displayed and are located near edges and for areas which have acute angles to the scanner look view; b) shows mostly values of false ice loss at the tope edges of the ice cliff, the values were removed using an edge filter in ArcMap during processing; c) False change at the edge of gullies on the mountainside, the data was therefore clipped to an AOI which included only the glacier terminus; c) False change observed on moraines and a scree slope, this area was also clipped from the dataset which was used in final analyses.

means that undercutting events may be missed entirely from satellite monitoring.

In terms of LiDAR analysis, DoDs are currently the most common method of point cloud comparison in the geosciences (Lague *et al.*, 2013) because the technique is very fast and computationally efficient. In this study, the two point clouds are gridded to generate DEMs which are differentiated on a pixel-by-pixel basis. Although this method is commonly used on large scale near planar geometry areas of interest such as river beds (e.g. Wheaton *et al.*, 2009; Schürch, *et al.*, 2011) and rock cliffs (e.g. Rosser *et al.*, 2005; Abellán *et al.*, 2010), ice cliffs can be complex surfaces, with crevasses, overhangs, and flakes of ice all of which create for a challenging surface to capture using TLS.

A method which has not presently been applied to an ice cliff is the Multiscale Model to Model Cloud Comparison (M3C2) algorithm. This method of point cloud comparison is available through Cloud Compare and offers a simplified comparison of complex 3D point clouds, with the additional benefit of detecting very small surface changes and assessing whether they are statistically significant (Lague *et al.*, 2013). The M3C2 method does not require gridding or meshing of the point cloud and operates in full 3D whilst also estimating its local accuracy. The M3C2 method has been demonstrated with success on active landslides (Kromer *et al.*, 2017), river channels (Lague *et al.*, 2013) and thermokarst (Barnhart & Crosby, 2013) and rockfalls (Williams *et al.*, in review). Kromer *et al.* (2017) used an automated terrestrial laser scanning (ATLS) system with automatic near-real-time change detection processing to monitor an active landslide in France. Applying a similar method at an ice cliff would improve future studies because the point cloud comparison would be more accurate and the processing time would be reduced which would allow the understanding, modelling and prediction of previously imperceptible changes at a glacier terminus, enabling the processes of calving to be more thoroughly understood.

6.4 Summary

This study has demonstrated the use of an automated near-real-time TLS system to monitor the ice cliff of the terminus at Fjallsjökull, Iceland. Figure 6.11 summarises the key findings and processes which can be measured using the method described in this thesis. The scanner collected data automatically and the data were processed on return from fieldwork. The results have shown that widespread areas of a glacier can undergo sub-metre vertical changes on sub-hourly timescales, and that these changes make it impossible to distinguish melt using

current methods. Rotational motion of the ice cliff is observed both coincident and non-coincident with calving, but needs to be assessed carefully because the advection of surface roughness features can give rise to false rotational motion if the data are not interpreted correctly. Ice loss is dominated by calving over the survey period and although melt is likely to be detected it cannot be quantified. The majority of ice loss occurs in the lower third of the ice cliff, and events begin with a smaller failure at the waterline that then propagates up cliff 30-60 minutes later. The data show no correlation between calving and air temperature, lake level or temperature at this scale, though the dataset is relatively short (28 hours). It seems that calving at this timescale is a time-dependent process which is capable of evolving over minutes to hours, with new failures occurring over past failures. The presence of a waterline notch is seemingly inhibited by rapid changes in lake level caused by extreme weather over the survey period, and therefore a waterline notch does not seem to be a key driver of calving on the 13th August.

There are inherent risks and uncertainties with laser scanning surveys, such as the ruggedness of the instrument and whether it is suitable for the conditions. The weather conditions can greatly affect the quality of the data, with an increase in rain intensity causing a decrease in point density within the LiDAR data. In terms of the method, it was necessary to operate the laser scanner from a single scan position, which led to occlusions in the data and error located at the edges of sharp features. Although the quality of the data can be somewhat improved by carefully locating this single scan position so that the surface is captured with the best possible coverage, it can never be negated when only using one scan position. Improvements to the method could therefore be introduced with the use of two laser scanners acquiring data in tandem, or by combining TLS with SFM to provide better coverage particularly at complex glacier surfaces. Future studies would also benefit from applying the M3C2 algorithm to improve the accuracy of point cloud comparisons and produce local accuracy statistics.

What can be measured using LiDAR to monitor the ice cliff of a lake-terminating glacier?

Rates of pre-failure deformation

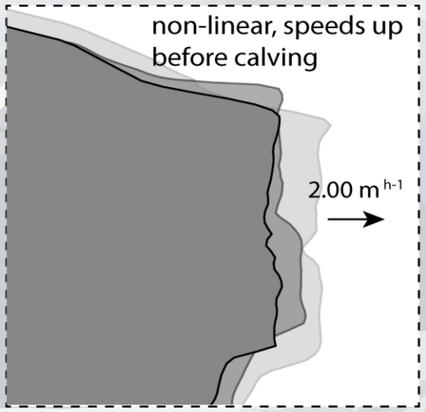

Incremental nature of calving

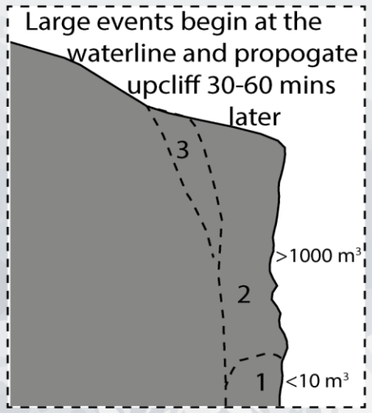

Upcliff patterns of total ice loss

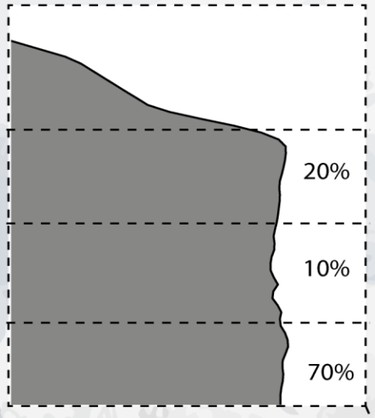

Surface melt where there is debris

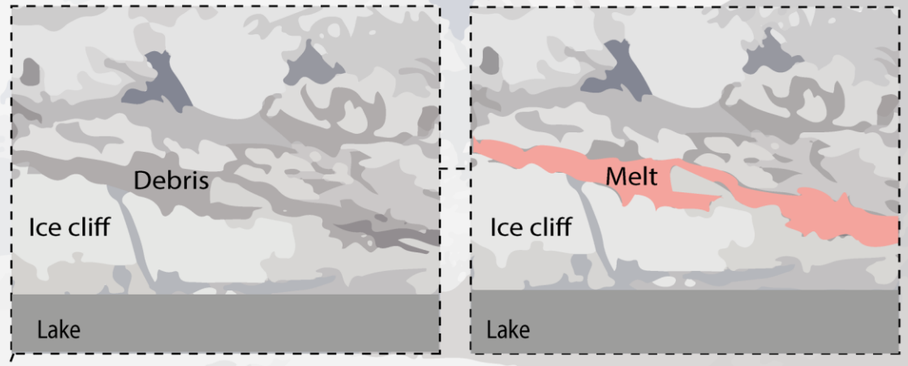

Melt cannot be quanitified due to upsidence and subsidence which occurs at greater magnitudes across widespread areas of the glacier.

Centimetre-scale upsidence and subsidence

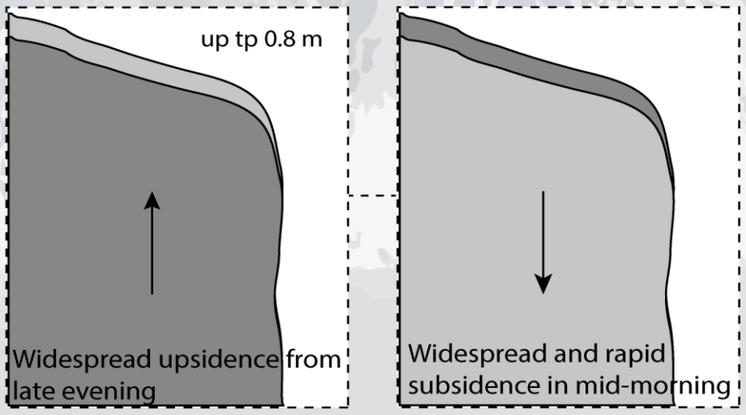

Rotation of ice

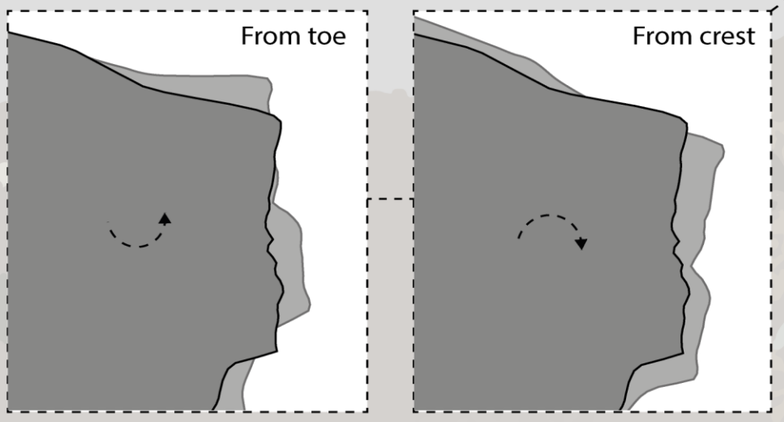

A note on limitations and data quality

* LiDAR data of the ice cliff every hour
* Average point spacing 0.15 m but patchy coverage
* 800 -1000 metres away from ice cliff
* 300 m wide AOI of sufficient quality for analysis
* Single scan position requires a filter for false change
* Does not work in heavy rain or fog weather

Automated near real-time TLS

Riegl VZ-4000

Figure 6.11) A summary diagram of the processes which can be measured and mapped using automated near real-time terrestrial laser scanning at the terminus of a lake-terminating glacier.

Chapter 7

Conclusions

With the progressive increase in the number and volume of ice-marginal lakes worldwide expected to continue in line with future climate change (Richardson & Reynolds, 2000; Stokes *et al.*, 2006; Schomacker, 2010; Trüssel *et al.*, 2013; Carrivick & Quincey, 2014) it is important to understand the processes of calving which occur at these glacier termini. The onset of calving at previously land based termini can lead to enhanced rates of retreat (Pelto *et al.*, 2013) and plays a crucial role in glacier dynamics (Schomacker, 2010). However, the processes which occur at glacier ice cliffs at the single event scale are still not fully understood (Chapuis & Tetzlaff, 2014), constituting a gap in fundamental glaciological knowledge (Van der Veen, 2013) and therefore, how well these processes can be represented in models of calving (Bassis, 2011). To address this challenge, this thesis has investigated calving processes at the single event scale, using high frequency (hourly) time-series terrestrial laser scanning.

This study aimed to monitor the ice cliff of a lake-terminating glacier near-continuously, at hourly to sub-hourly intervals and at a high spatial resolution (<1.0 m), and observe calving processes at the single event scale for at least one diurnal cycle. A suitable fieldsite was located at Fjallsjökull in Iceland, and the method for the automatic monitoring of the glacier using a Riegl VZ-4000 laser scanner was presented. The analysis of the LiDAR data which was acquired has allowed the following key conclusions to be drawn, under the caveat that they are limited to only a 300 m section of a ~1000 m ice margin and over a relatively short one and a half day period.

1. **Very long range terrestrial laser scanners such as the Riegl *VZ*-4000 can be used to automatically monitor glacier dynamics, specifically short-term phenomenon at unrivalled spatiotemporal resolutions.** This study has demonstrated that the processes of calving can be observed and quantified at sub-hourly intervals using TLS.

2. **The dominant mode of ice loss at the subaerial ice cliff during the study period was by calving, no melt was recorded at the vertical face.** Ice loss over the 28-hour period was dominated by two large calving events. Melting is thought to be observed at the top of the ice cliff on the horizontal surface of the glacier at the crest of the cliff, but unfortunately it cannot be quantified because surface elevation changes occur

which are of a greater order of magnitude. However, it is worth noting that there was no melt modelling, or empirical data to test an alternative hypothesis. The time period over which these measurements were made is very short and therefore, given the stochastic nature of calving, it is possible though unlikely (because further activity was evident anecdotally in the field that these were the only two calving events in a week. The area over which these calculations were made were small in comparison to the overall area of the ice face, and may well be under- or over-representative of calving activity across the calving front.

3. **Strong patterns were observed in ice loss with elevation above the waterline.** 70% of all ice loss occurred in the bottom third of the ice cliff, with the first metre above the waterline undergoing the greatest retreat during the survey period. Only 10% of ice loss occurred in the middle elevational third of the ice cliff, and the top third accounted for 20%. It is likely that at least some of the 20% of ice loss which is observed in the top third of the ice cliff was due to melting. If this is the case, the general trend of ice loss would reduce with height up cliff from the toe.

4. **Pre-failure deformation was greater than observed in previous studies and is likely to be non-linear in rate through time.** The ice cliff deformed by up to 2.00 m h^{-1} in the immediate hour prior to calving, at a rate more than the average velocity (0.15 m d^{-1}/ 0.006 m h^{-1}) and sped up prior to calving implying that this deformation at the glacier ice cliff is a non-linear process.

5. **Rotation of ice is recorded coincident with vertical surface elevation fluctuations around the time of calving, implying that rotation due to torque and buoyant forces were captured in the dataset.** Rotation from the toe of the ice cliff is observed prior to both large calving events. After calving, the glacier readjusts and the relative surface elevation uplifts to a level that is greater than the pre-calving level. This process implies that after calving the glacier may sit higher in the water due to buoyant forces.

6. **Rotation forward and down from the crest of the ice cliff is recorded in between calving events indicating the forward bending of the ice cliff.** The ice cliff shows forward bending during a period of no calving activity within the AOI.

In light of the results, this thesis has addressed RQ1, by investigating the spatial characteristics of calving behaviour at the ice cliff at hourly to sub-hourly timescales. This was achieved

through the extraction of DEMs of Difference (DoDs), 2D swath profiles at three intervals along the width of the AOI and by performing zonal statistics on elevational bands from the toe to the crest of the ice cliff. From these results, it was discovered that the height of the ice cliff which was subject to the greatest calving activity was a one metre zone above the waterline, and that the bottom third of the ice cliff accounted for 70% of total ice loss. Furthermore, the incremental nature of calving events at the single event scale was quantified, with failures beginning at the waterline at propagating up-cliff 30-60 minutes later. In addition, failures also appeared to evolve over the following 24-hours immediately after the initial failure. In addressing RQ2, it appears that the temporal pattern of ice loss over a diurnal cycle is a time-dependent process, but that environmental conditions may have more of an influence on where the failures occur, with most of the failures originating at the waterline. Unfortunately, the full magnitude/frequency distribution (RQ3) could not be described because it was necessary to filter the dataset due to an effect which occurred at sharp edges, whereby spuriously large values of change were recorded. However, this is an important finding with regard to future studies because operating a TLS survey over complex glacier surfaces requires careful planning and processing in order to be able to rely on results. In spite of this, the two large events which occurred on the 13th August appeared to dominate the pattern of ice loss, and although smaller events were recorded they were not actually that numerous in the dataset.

In future, studies of a similar nature would benefit from operating a combined TLS and SfM survey to provide better coverage particularly at complex glacier surfaces. Furthermore, applying the M3C2 algorithm to the LiDAR data would improve the accuracy of point cloud comparisons and produce local accuracy statistics.

In conclusion, this study has demonstrated that monitoring an ice cliff with time-lapse TLS is a viable method from which spatiotemporal processes of calving can be observed, quantified, and mapped near continuously at a safe distance from glacier termini and at unrivalled resolutions. The results acquired from such studies will be valuable for studying the impacts of proglacial lake growth and development, and in modelling calving processes at the ice cliff.

References

Abellán, A., Calvet, J., Vilaplana, J. & Blanchard, J. (2010). Detection and spatial prediction of rockfalls by means of terrestrial laser scanner monitoring. *Geomorphology*. 119 (3–4). p.p. 162–171.

Abellán, A., Oppikofer, T., Jaboyedoff, M., Rosser, N.J., Lim, M. & Lato, M.J. (2014). Terrestrial laser scanning of rock slope instabilities. *Earth Surface Processes and Landforms*. 39 (1). p.p. 80–97.

Abellán, A., Penna, I., Daicz, S., Carrea, D., Derron, M.-. H., Jaboyedoff, M., Riquelme, A.J. & Tomas, R. (2015). Can we use ice calving on glacier fronts as a proxy for rock slope failures? *EGU General Assembly Conference Abstracts*. 17. p.p. 11825.

Aðalgeirsdóttir, G., Jóhannesson, T., Björnsson, H., Pálsson, F. & Sigurðsson, O. (2006). Response of Hofsjökull and southern Vatnajökull, Iceland, to climate change. *Journal of Geophysical Research: Earth Surface*. 111 (F3). p.p. 1–15.

Åström, J.A., Vallot, D., Schäfer, M., Welty, E.Z., O'Neel, S., Bartholomaus, T.C., Liu, Y., Riikilä, T.I., Zwinger, T., Timonen, J. & Moore, J.C. (2014). Termini of calving glaciers as self-organized critical systems. *Nature Geoscience*. 7 (12). p.p. 874–878.

Åström, J., Riikila, T. & Tallinen, T. (2013). *A particle based simulation model for glacier dynamics*. 7. p.p. 1591–1602.

Barnhart, T. & Crosby, B. (2013). Comparing two methods of surface change detection on an evolving thermokarst using high-temporal-frequency terrestrial laser scanning, Selawik River. *Remote Sensing*. 5 (6). p.p. 2813–2837.

Bartholomaus, T.C., Amundson, J.M., Walter, J.I., O'Neel, S., West, M.E. & Larsen, C.F. (2015). Subglacial discharge at tidewater glaciers revealed by seismic tremor. *Geophysical Research Letters*. 42 (15). p.p. 6391–6398.

Bassis, J.N. (2011). The statistical physics of iceberg calving and the emergence of universal calving laws. *Journal of Glaciology*. 57 (201). p.p. 3–16.

Bassis, J.N. & Jacobs, S. (2013). Diverse calving patterns linked to glacier geometry. *Nature*

Geoscience. 6 (10). p.p. 833–836.

Bater, C.W. & Coops, N.C. (2009). Evaluating error associated with lidar-derived DEM interpolation. *Computers & Geosciences*. 35 (2). p.p. 289–300.

Benn, D.I. & Evans, D.J.A. (2010). *Glaciers & Glaciation*. Second Edi. Abingdon: Hodder Education.

Benn, D.I., Hulton, N.R.J. & Mottram, R.H. (2007a). 'Calving laws', 'sliding laws' and the stability of tidewater glaciers. *Annals of Glaciology*. 46 (1996). p.p. 123–130.

Benn, D.I., Warren, C.R. & Mottram, R.H. (2007b). Calving processes and the dynamics of calving glaciers. *Earth-Science Reviews*. 82. p.p. 143–179.

Bindschadler, R. (1983). The Predicted Behavior of Griesgletscher, Wallis, Switzerland, and its Possible Threat to a Nearby Dam. *Annals of Glaciology*. 4 (1). p.p. 295–295.

Björnsson, H. (2017). *The Glaciers of Iceland: A Historical, Cultural and Scientific Overview*. C. O'Cofaigh (ed.). Reykjavik: Atlantis Advances in Quaternary Science.

Bond, G.C. & Lotti, R. (1995). Iceberg discharges into the North Atlantic on millennial time scales during the last glaciation. *Science; Feb.* (267). p.p. 1005–1010.

Boyce, E.S., Motyka, R.J. & Truffer, M. (2007). Flotation and retreat of a lake-calving terminus, Mendenhall Glacier, southeast Alaska, USA. *Journal of Glaciology*. 53 (181). p.p. 211–224.

Brown, C., Meier, M. & Post, A. (1982). *Calving speed of Alaska tidewater glaciers, with application to Columbia Glacier: Geological Survey Proffesional Paper 1258-C*. Washington D.C.

Budd, W., Jacka, T. & Morgan, V. (1980). Antarctic iceberg melt rates derived from size distributions and movement rates. *Annals of Glaciology*.

Carlson, A.E., LeGrande, A.N., Oppo, D.W., Came, R.E., Schmidt, G.A., Anslow, F.S., Licciardi, J.M. & Obbink, E.A. (2008). Rapid early Holocene deglaciation of the Laurentide ice sheet. *Nature Geoscience*. 1 (9). p.p. 620–624.

Carr, J.R., Bell, H., Killick, R. & Holt, T. (2017). Exceptional retreat of Novaya Zemlya's

marine-terminating outlet glaciers between 2000 and 2013. *The Cryosphere Discuss., in review*. p.p. 1–36.

Carrivick, J.L. & Quincey, D.J. (2014). Progressive increase in number and volume of ice-marginal lakes on the western margin of the Greenland Ice Sheet. *Global and Planetary Change*. 116. p.p. 156–163.

Carrivick, J.L. & Tweed, F.S. (2013). Proglacial lakes: character, behaviour and geological importance. *Quaternary Science Reviews*. 78. p.p. 34–52.

Chapuis, A., Rolstad, C. & Norland, R. (2010). Interpretation of amplitude data from a ground-based radar in combination with terrestrial photogrammetry and visual observations for calving monitoring of Kronebreen, Svalbard. *Annals of Glaciology*. 51 (55). p.p. 34–40.

Chapuis, A. & Tetzlaff, T. (2014). The variability of tidewater-glacier calving: Origin of event-size and interval distributions. *Journal of Glaciology*. 60 (222). p.p. 622–634.

Claridge, D.E. & Chen, H. (2006). Missing data estimation for 1–6 h gaps in energy use and weather data using different statistical methods. *International Journal of Energy Research*. 30 (13). p.p. 1075–1091.

Conforti, D., Deline, P., Mortara, G. & Tamburini, A. (2005). Terrestrial Scanning Lidar Technology applied to study the evolution of the ice-contact image lake (Mont Blanc, Italy). *Commission VI, WG VI/4*. p.p. 1–5.

Cook, S., Rutt, I.C., Murray, T., Luckman, A., Zwinger, T., Selmes, N., Goldsack, A. & James, T.D. (2014). Modelling environmental influences on calving at Helheim Glacier in eastern Greenland. *The Cryosphere*. 8. p.p. 827–841.

Cuffey, K. & Paterson, W. (2010). *The physics of glaciers*. Fourth Edi. Oxford.

Cutler, P.M., Mickelson, D.M., Colgan, P.M., Macayeal, D.R. & Parizek, B.R. (2001). Influence of the Great Lakes on the dynamics of the southern Laurentide ice sheet: Numerical experiments. *Geology*. 29 (3). p.p. 1039–1042.

ESRI (2017a). *Feature Vertices To Points—Data Management toolbox | ArcGIS Desktop*. [Online]. 2017. Available from: http://pro.arcgis.com/en/pro-app/tool-reference/data-

management/feature-vertices-to-points.htm. [Accessed: 8 June 2017].

ESRI (2017b). *Summary Statistics—Help | ArcGIS for Desktop*. [Online]. 2017. Available from: http://desktop.arcgis.com/en/arcmap/10.3/tools/analysis-toolbox/summary-statistics.htm. [Accessed: 8 June 2017].

Evans, D.J.A. & Twigg, D.R. (2002). The active temperate glacial landsystem: a model based on Breiðamerkurjökull and Fjallsjökull, Iceland. *Quaternary Science Reviews*. 21 (20). p.p. 2143–2177.

Fischer, M., Huss, M., Kummert, M. & Hoelzle, M. (2016). Application and validation of long-range terrestrial laser scanning to monitor the mass balance of very small glaciers in the Swiss Alps. *The Cryosphere*. 10 (3). p.p. 1279–1295.

Fonstad, M.A., Dietrich, J.T., Courville, B.C., Jensen, J.L. & Carbonneau, P.E. (2013). Topographic structure from motion: a new development in photogrammetric measurement. *Earth Surface Processes and Landforms*. 38 (4). p.p. 421–430.

Funk, M. & Röthlisberger, H. (1989). Forecasting the effects of a planned reservoir which will partially flood the tongue of Unteraargletscher in Switzerland. *Annals of Glaciology*. 13. p.p. 76–81.

Gabbud, C., Micheletti, N. & Lane, S.N. (2015). Lidar measurement of surface melt for a temperate Alpine glacier at the seasonal and hourly scales. *Journal of Glaciology*. 61 (229). p.p. 963–974.

Girardeau-Montaut, D. (2015). *CloudCompare version 2.6.1. user manual*. p.p. 181.

Glowacki, O., Deane, G.B., Moskalik, M., Blondel, P., Tegowski, J. & Blaszczyk, M. (2015). Underwater acoustic signatures of glacier calving. *Geophysical Research Letters*. 42 (3). p.p. 804–812.

Hannesdóttir, H., Björnsson, H., Pálsson, F., Adalgeirsdóttir, G. & Gudmundsson, S. (2015). Changes in the southeast Vatnajokull ice cap, Iceland, between 1890 and 2010. *Cryosphere*. 9 (2). p.p. 565–585.

Haresign, E. & Warren, C. (2005). Melt rates at calving termini: a study at Glaciar León, Chilean Patagonia. *Geological Society, London, Special*. 242. p.p. 99–109.

Heinrich, H. (1988). Origin and Consequences of Cyclic Ice Rafting in the Northeast Atlantic Ocean During the Past 130,000 Years. *Quaternary Research*. 29 (2). p.p. 142–152.

Hengl, T. (2006). Finding the right pixel size. *Computers & Geosciences*. 32 (9). p.p. 1283–1298.

Hill, B.T. (2000). *Database of ship collisions with icebergs*. Ottawa.

Hodge, R. & Brasington, J. (2009). In situ characterization of grain-scale fluvial morphology using Terrestrial Laser Scanning. *Earth Surface Processes*. 34 (7). p.p. 954–968.

Holdsworth, G. (1973). Ice calving into the proglacial Generator Lake, Baffin Island, NWT, Canada. *Journal of Glaciology*. 12 (65). p.p. 235–250.

Howarth, P.J. & Price, R.J. (1969). The Proglacial Lakes of Breiðamerkurjökull and Fjallsjökull, Iceland. *The Geographical Journal*. 135 (4). p.p. 573.

Howat, I.M., Joughin, I., Tulaczyk, S. & Gogineni, S. (2005). Rapid retreat and acceleration of Helheim Glacier, east Greenland. *Geophysical Research Letters*. 32 (22).

Hughes, T.J. (1986). The Jakobshavns Effect. *Geophysical Research Letters*. 13 (1). p.p. 46–48.

IPCC (2013). *Summary for Policymakers. In: Climate Change 2013: The Physical Science Basis. Contribution of Working Group I to the Fifth Assessment Report of the Intergovernmental Panel on Climate Change*. T. F. Stocker, G.-K. D. Qin, M. Plattner, S. K. Tignor, J. B. Allen, A. Nauels, Y. Xia, V. Bex, & P. M. Midgley (eds.). Cambridge: Cambridge University Press.

James, T.D., Murray, T., Selmes, N., Scharrer, K. & O'Leary, M. (2014). Buoyant flexure and basal crevassing in dynamic mass loss at Helheim Glacier. *Nature Geoscience*. 7 (8). p.p. 593–596.

Jóhannesson, T., Björnsson, H., Magnússon, E., Gudmundsson, S., Pálsson, F., Sigurdsson, O., Thorsteinsson, T. & Berthier, E. (2013). Ice-volume changes, bias estimation of mass-balance measurements and changes in subglacial lakes derived by lidar mapping of the surface of Icelandic glaciers. *Annals of Glaciology*. 54 (63). p.p. 63–74.

Kirkbride, M.P. (1993). The temporal significance of transitions from melting to calving termini at glaciers in the central Southern Alps of New Zealand. *The Holocene*. 3 (3). p.p. 232–240.

Kirkbride, M.P. & Warren, C.R. (1997). Calving processes at a grounded ice cliff. *Annals of Glaciology*. 24. p.p. 116–121.

Kohler, J. (2008). *How close should boats come to the fronts of Svalbard's calving glaciers?*

Krimmel, R. (1997). *Documentation of the retreat of Columbia Glacier, Alaska.*

Kromer, R.A., Abellán, A., Hutchinson, D.J., Lato, M., Chanut, M.-A., Dubois, L. & Jaboyedoff, M. (2017). Automated terrestrial laser scanning with near-real-time change detection – monitoring of the Séchilienne landslide. *Earth Surface Dynamics*. 5 (2). p.p. 293–310.

Kulessa, B., Booth, A.D., Hobbs, A. & Hubbard, A.L. (2008). Automated monitoring of subglacial hydrological processes with ground-penetrating radar (GPR) at high temporal resolution: scope and potential pitfalls. *Geophysical Research Letters*. 35 (24). p.p. 1–5.

Lague, D., Brodu, N. & Leroux, J. (2013). Accurate 3D comparison of complex topography with terrestrial laser scanner: Application to the Rangitikei canyon (NZ). *ISPRS Journal of Photogrammetry and*. 82. p.p. 10–26.

Lim, M., Rosser, N.J., Allison, R.J. & Petley, D.N. (2010). Erosional processes in the hard rock coastal cliffs at Staithes, North Yorkshire. *Geomorphology*. 114 (1–2). p.p. 12–21.

Lingle, C.S., Post, A., Herzfeld, C.A., Molnia, B.F., Krimmel, R.M. & Roush, J.J. (1993). Bering Glacier surge and iceberg-calving mechanism at Vitus Lake, Alaska, U.S.A. *Journal of Glaciology*. 39 (133). p.p. 722–727.

Lüthi, M.P. & Vieli, A. (2016). Multi-method observation and analysis of a tsunami caused by glacier calving. *The Cryosphere*. 10. p.p. 995–1002.

Macayeal, D.R., Abbot, D.S. & Sergienko, O. V (2011). Iceberg-capsize tsunamigenesis. *Annals of Glaciology*. 52 (58). p.p. 51–56.

Meier, M. & Post, A. (1987). Fast tidewater glaciers. *Journal of Geophysical Research: Solid Earth*. 92 (B9). p.p. 9051–9058.

Meier, M.F. (1994). *Columbia Glacier during rapid retreat: interactions between glacier flow and*

iceberg calving dynamics. In: Reeh, N. (Ed.). Copenhagen.

Meier, M.F. (1997). *The iceberg discharge process: observations and inferences drawn from the study of Columbia Glacier. Byrd Polar Res. Cent. Rep, 15, pp.109-114.*

Meier, M.F., Dyurgerov, M.B., Rick, U.K., O'Neel, S., Pfeffer, W.T., Anderson, R.S., Anderson, S.P. & Glazovsky, A.F. (2007). Glaciers Dominate Eustatic Sea-Level Rise in the 21st Century. *Science*. 317 (5841).

Mogridge, G.R. & Jamieson, W.W. (1980). Wave Impact Pressures on Composite Breakwaters. *Coastal Engineering Proceedings.* 1 (17). p.p. 1829–1848.

Moore, J.C., Grinsted, A., Zwinger, T. & Jevrejeva, S. (2013). Semiempirical and process-based global sea level projections. *Reviews of Geophysics.* 51 (3). p.p. 484–522.

Mountain Research Initiative (2016). *Evidence of a GLOF breaching a moraine-dammed proglacial lake in Peru.*

Murray, T., Nettles, M., Selmes, N., Cathles, L.M., Burton, J.C., James, T.D., Edwards, S., Martin, I., O'Farrell, T., Aspey, R., Rutt, I. & Bauge, T. (2015a). Reverse glacier motion during iceberg calving and the cause of glacial earthquakes. *Science.*

Murray, T., Selmes, N., James, T.D., Edwards, S., Martin, I., O'Farrell, T., Aspey, R., Rutt, I., Nettles, M. and Baugé, T. (2015b). Dynamics of glacier calving at the ungrounded margin of Helheim Glacier, southeast Greenland. *Journal of Geophysical Research: Earth Surface,* 120 (6), p.p.964-982.

Nguyen, H.T., Fernandez-Steeger, T.M., Wiatr, T., Rodrigues, D. & Azzam, R. (2011). Use of terrestrial laser scanning for engineering geological applications on volcanic rock slopes – an example from Madeira island (Portugal). *Natural Hazards and Earth System Science*. 11 (3). p.p. 807–817.

Nick, F.M., van der Veen, C.J. & Oerlemans, J. (2007). Controls on advance of tidewater glaciers: Results from numerical modeling applied to Columbia Glacier. *Journal of Geophysical Research: Earth Surface.* 112 (3).

Nick, F.M., Van Der Veen, C.J., Vieli, A. & Benn, D.I. (2010). A physically based calving model applied to marine outlet glaciers and implications for the glacier dynamics.

Journal of Glaciology. 56 (199). p.p. 781–794.

Nienow, P., Sharp, M. & Willis, I. (1998). Seasonal changes in the morphology of the subglacial drainage system, Haut Glacier d'Arolla, Switzerland. *Earth Surface Processes and*. 23. p.p. 825–843.

Norman, E.C., Rosser, N.J., Brain, M.J., Petley, D.N. & Lim, M. (2013). Coastal cliff-top ground motions as proxies for environmental processes. *Journal of Geophysical Research: Oceans*. 118 (12). p.p. 6807–6823.

O'Leary, M. (2011). *Frontal processes on tidewater glaciers*.

O'Neel, S. (2000). *Motion and calving at LeConte Glacier, Alaska*.

O'Neel, S., Echelmeyer, K.A. & Motyka, R.J. (2003). Short-term variations in calving of a tidewater glacier: LeConte Glacier, Alaska, U. S. A. *Journal of Glaciology*. 49 (167). p.p. 587–598.

O'Neel, S., Larsen, C. & Rupert, N. (2010). Iceberg calving as a primary source of regional-scale glacier-generated seismicity in the St. Elias Mountains, Alaska. *Journal of Geophysical*. 115 (F4). p.p. 1–12.

Orheim, O. (1985). *Iceberg discharge and the mass balance of Antarctica, Glaciers, Ice Sheets and Sea Level: Effect of a CO2-Induced Climatic Change*.

Östrem, G. (1959). Ice melting under a thin layer of moraine, and the existence of ice cores in moraine ridges. *Geografiska Annaler*. 41 (4). p.p. 228–230.

Pack, R.T., Blonquist, K. & Carter, B. (2012). LiDAR bare-earth modeling of overhanging cliffs - extending 2.5-D LiDAR classifiers to handle 3D surface classification problems. *ASPRS Annual Conference*. p.p. 1–10.

Pelto, M., Capps, D., Clague, J.J. & Pelto, B. (2013). Rising ELA and expanding proglacial lakes indicate impending rapid retreat of Brady Glacier, Alaska. *Hydrological Processes*. 27 (21). p.p. 3075–3082.

Pelto, M. & Warren, C. (1991). Relationship between tidewater glacier calving velocity and water depth at the calving front. *Annals of glaciology*. 15. p.p. 115–118.

Pesci, A., Loddo, F. & Conforti, D. (2007). The first terrestrial laser scanner application over Vesuvius: High resolution model of a volcano crater. *International Journal of Remote Sensing*. 28 (1). p.p. 203–219.

Petlicki, M., Cieply, M., Jania, J.A., Prominska, A. & Kinnard, C. (2015). Calving of a tidewater glacier driven by melting at the waterline. *Journal of Glaciology*. 61 (229). p.p. 851–863.

Pollard, D. (1984). Some Ice-Age Aspects of a Calving Ice-Sheet Model. In: *Milankovitch and Climate*. Dordrecht: Springer Netherlands, p. 541–564.

Reeh, N. (1968). On the calving of ice from floating glaciers and ice shelves. *Journal of Glaciology*. 7 (50). p.p. 215–232.

Richardson, S.D. & Reynolds, J.M. (2000). An overview of glacial hazards in the Himalayas. *Quaternary International*. 65. p.p. 31–47.

Riegl Data Sheet (2015). *Riegl VZ-4000*. (23-03–2015).

Robertson, C.M., Benn, D.I., Brook, M.S., Fuller, I.C. & Holt, K.A. (2012). Subaqueous calving margin morphology at Mueller, Hooker and Tasman glaciers in Aoraki/Mount Cook National Park, New Zealand. *Journal of Glaciology*. 58 (212). p.p. 1037–1046.

Röhl, K. (2006). Terminus disintegration of debris-covered, lake-calving glaciers. *Unpublished PhD thesis, University of Otago, New*.

Rosser, N.J., Brain, M.J., Petley, D.N., Lim, M. & Norman, E.C. (2013). Coastline retreat via progressive failure of rocky coastal cliffs. *Geology*. 41 (8). p.p. 939–942.

Rosser, N.J., Petley, D.N., Lim, M., Dunning, S.A. & Allison, R.J. (2005). Terrestrial laser scanning for monitoring the process of hard rock coastal cliff erosion. *Quarterly Journal of Engineering Geology and Hydrogeology*. 38 (4). p.p. 363–375.

Rott, H., Stuefer, M., Siegel, A., Skvarca, P. & Eckstaller, A. (1998). Mass fluxes and dynamics of Moreno Glacier, Southern Patagonia Icefield. *Geophysical Research Letters*. 25 (9). p.p. 1407–1410.

Ryan, J.C., Hubbard, A.L., Box, J.E., Todd, J., Christoffersen, P., Carr, J.R., Holt, T.O. & Snooke, N. (2015). UAV photogrammetry and structure from motion to assess calving

dynamics at Store Glacier, a large outlet draining the Greenland ice sheet. *Cryosphere*. 9 (1). p.p. 1–11.

Sayag, R. & Worster, M.G. (2013). Elastic dynamics and tidal migration of grounding lines modify subglacial lubrication and melting. *Geophysical Research Letters*. 40 (22). p.p. 5877–5881.

Scambos, T.A., Hulbe, C., Fahnestock, M. & Bohlander, J. (2000). The link between climate warming and break-up of ice shelves in the Antarctic Peninsula. *Journal of Glaciology*. 46 (154). p.p. 516–530.

Scambos, T., Fricker, H.A., Liu, C.-C., Bohlander, J., Fastook, J., Sargent, A., Massom, R. & Wu, A.-M. (2009). Ice shelf disintegration by plate bending and hydro-fracture: Satellite observations and model results of the 2008 Wilkins ice shelf break-ups. *Earth and Planetary Science Letters*. 280 (1). p.p. 51–60.

Scherler, D., Leprince, S. & Strecker, M. (2008). Glacier-surface velocities in alpine terrain from optical satellite imagery—Accuracy improvement and quality assessment. *Remote Sensing of Environment*. 112 (10). p.p. 3806–3819.

Schomacker, A. (2010). Expansion of ice-marginal lakes at the Vatnajökull ice cap, Iceland, from 1999 to 2009. *Geomorphology*. 119 (3). p.p. 232–236.

Schulson, E.M. & Hibler, W.D. (1991). The fracture of ice on scales large and small: Arctic leads and wing cracks. *Journal of Glaciology*. 37 (127). p.p. 319–322.

Schürch, P., Densmore, A. & Rosser, N. (2011). Detection of surface change in complex topography using terrestrial laser scanning: application to the Illgraben debris-flow channel. *Earth Surface*. 36. p.p. 1847–1859.

Schwalbe, E., Maas, H.-G., Dietrich, R. & Ewert, H. (2008). Glacier velocity determination from multi temporal terrestrial long range laser scanner point clouds. *The International Archives of the Photogrammetry, Remote Sensensing and Spatial Information Sciences*. 37. p.p. 457–462.

Sikonia, W. (1982). *Finite element glacier dynamics model applied to Columbia Glacier, Alaska: Geological Survey Proffesional Paper 1258-B*. Washington D.C.

Skvarca, P., De Angelis, H., Naruse, R., Warren, C.R. & Aniya, M. (2002). Calving rates in fresh water: new data from southern Patagonia. *Annals of Glaciology*. 34 (1). p.p. 379–384.

Smith, M.W. (2014). Roughness in the Earth Sciences. *Earth-Science Reviews*. 136. p.p. 202–225.

Smith, M.W., Quincey, D.J., Dixon, T., Bingham, R.G., Carrivick, J.L., Irvine-Fynn, T.D.L. & Rippin, D.M. (2016). Aerodynamic roughness of glacial ice surfaces derived from high-resolution topographic data. *Journal of Geophysical Research: Earth Surface*. 121 (4). p.p. 748–766.

Stokes, C., Gurney, S. & Shahgedanova, M. (2006). Late-20th-century changes in glacier extent in the Caucasus Mountains, Russia/Georgia. *Journal of*. 52 (176). p.p. 99–109.

Stokes, C.R. & Clark, C.D. (2004). Evolution of late glacial ice-marginal lakes on the northwestern Canadian Shield and their influence on the location of the Dubawnt Lake palaeo-ice stream. *Palaeogeography, Palaeoclimatology, Palaeoecology*. 215 (1). p.p. 155–171.

Sugiyama, S., Minowa, M., Sakakibara, D., Skvarca, P., Sawagaki, T., Ohashi, Y., Naito, N. & Chikita, K. (2016). Thermal structure of proglacial lakes in Patagonia. *Journal of Geophysical Research: Earth Surface*. 121 (12). p.p. 2270–2286.

Tardivo, G., Berti, A., Tardivo, G. & Berti, A. (2012). A Dynamic Method for Gap Filling in Daily Temperature Datasets. *Journal of Applied Meteorology and Climatology*. 51 (6). p.p. 1079–1086.

Telling, J., Lyda, A., Hartzell, P. & Glennie, C. (2017). Review of Earth science research using terrestrial laser scanning. *Earth-Science Reviews*. 169. p.p. 35–68.

Theakstone, W. (1989). Further catastrophic break-up of a calving glacier: observations at Austerdalsisen, Svartisen, Norway, 1983-87. *Geografiska Annaler. Series A. Physical Geography*. 71 (3). p.p. 245–253.

Theakstone, W.H. & Knudsen, N.T. (1986). Recent Changes of a Calving Glacier, Austerdalsisen, Svartisen, Norway. *Geografiska Annaler. Series A, Physical Geography*. 68 (4). p.p. 303.

Tinti, S., Maramai, A. & Cerutti, A. (1999). The Miage Glacier in the Valley of Aosta (Western Alps, Italy) and the extraordinary detachment which occurred on August 9, 1996. *Physics and Chemistry of the Earth, Part A:*. 24 (2). p.p. 157–161.

Trüssel, B.L., Motyka, R.J., Truffer, M. & Larsen, C.F. (2013). Rapid thinning of lake-calving Yakutat Glacier and the collapse of the Yakutat Icefield, southeast Alaska, USA. *Journal of Glaciology*. 59 (213). p.p. 149–161.

Vann Jones, E.C., Rosser, N.J., Brain, M.J. & Petley, D.N. (2015). Quantifying the environmental controls on erosion of a hard rock cliff. *Marine Geology*. 363. p.p. 230–242.

Vaughan, D.G., Comiso, J.C., Allison, I., Carrasco, J., Kaser, G., Kwok, R., Mote, P., Murray, T., Paul, F., Ren, J., Rignot, E., Solomina, O., Steffen, K. & Zhang, T. (2013). Observations: Cryosphere. *Climate Change 2013: The Physical Science Basis. Contribution of Working Group I to the Fifth Assessment Report of the Intergovernmental Panel on Climate Change*. p.p. 317–382.

Van der Veen, C.J. (2002). Calving glaciers. *Progress in Physical Geography*. 26 (1). p.p. 96–122.

Van der Veen, C.J. (1999). Crevasses on glaciers. *Polar Geography*. 23 (3). p.p. 213–245.

Van der Veen, C.J. (2013). *Fundamentals of glacier dynamics*. Boca Raton: CRC Press.

Van der Veen, C.J. (1996). Tidewater calving. *Journal of Glaciology*. 42 (141). p.p. 375–385.

Venteris, E.., Whillan, I.M. & Van der Veen, C.J. (1997). Effect of extension rate on terminus position, Columbia Glacier, Alaska, U.S.A. *Annals of Glaciology*. 24. p.p. 49–53.

Vieli, A., Funk, M. & Blatter, H. (2001). Flow dynamics of tidewater glaciers: a numerical modelling approach. *Journal of Glaciology*. 47. p.p. 595–606.

Vieli, A., Funk, M. & Blatter, H. (2000). Tidewater glaciers: frontal flow acceleration and basal sliding. *Annals of Glaciology*. 31 (1). p.p. 217–221.

Vieli, A., Jania, J. & Kolondra, L. (2002). The retreat of a tidewater glacier: observations and model calculations on Hansbreen, Spitsbergen. *Journal of Glaciology*. 48 (163). p.p. 592–

600.

Wagner, T.J.W., James, T.D., Murray, T. & Vella, D. (2016). On the role of buoyant flexure in glacier calving. *Geophysical Research Letters*. 43 (1). p.p. 232–240A.

Wainwright, D. (2014). *Calving Front Dynamics : External Forces that Lead to Specific Sized Calving Events*.

Walter, F., O'Neel, S., McNamara, D., Pfeffer, W.T., Bassis, J.N. & Fricker, H.A. (2010). Iceberg calving during transition from grounded to floating ice: Columbia Glacier, Alaska. *Geophysical Research Letters*. 37 (15). p.p. 1–5.

Warren, C., Benn, D., Winchester, V. & Harrison, S. (2001). Buoyancy-driven lacustrine calving, Glaciar Nef, Chilean Patagonia. *Journal of Glaciology*. 47 (156). p.p. 135–146.

Warren, C., Greene, D. & Glasser, N. (1995). Glaciar Upsala, Patagonia: rapid calving retreat in fresh water. *Annals of glaciology*. 21. p.p. 311–316.

Warren, C.R. & Kirkbride, M.P. (2003). Calving speed and climatic sensitivity of New Zealand lake-calving glaciers. *Annals of Glaciology*. 36 (1). p.p. 173–178.

Weertman, J. (1973). Can a water-filled crevasse reach the bottom surface of a glacier. *IASH Publ*. p.p. 139–145.

Westoby, M.J., Brasington, J., Glasser, N.F., Hambrey, M.J. & Reynolds, J.M. (2012). 'Structure-from-Motion' photogrammetry: A low-cost, effective tool for geoscience applications. *Geomorphology*. 179. p.p. 300–314.

Wheaton, J.M., Brasington, J., Darby, S.E. & Sear, D. a. (2009). Accounting for uncertainty in DEMs from repeat topographic surveys: improved sediment budgets. *Earth Surface Processes and Landforms*. 156 (December 2009).

Whillans, I.M. & Van Der Veen, C.J. (1997). The role of lateral drag in the dynamics of Ice Stream B, Antarct...: Ingenta Connect. *Journal of Glaciology*. 43 (7). p.p. 231–237.

Williams, J.G., Rosser, N.J., Hardy, R.J., Brain, M.J. & Afana, A.A. (2017). Optimising 4D Approaches to Surface Change Detection: Improving Understanding of Rockfall Magnitude-Frequency. *Earth Surface Dynamics Discussions., in review*. p.p. 1–36.

Wolman, M.G. & Miller, J.P. (1960). Magnitude and Frequency of Forces in Geomorphic Processes. *The Journal of Geology*. 68 (1). p.p. 54–74.

Zeibak, R. & Filin, S. (2007). Change detection via terrestrial laser scanning. *IAPRS Volume XXXVI*. 3 (52). p.p. 430–435.

Appendices

Appendix 1 Riegl *VZ*-4000 datasheet © RIEGL LMS, www.riegl.com.

Max. Measurement Range RIEGL VZ® -4000

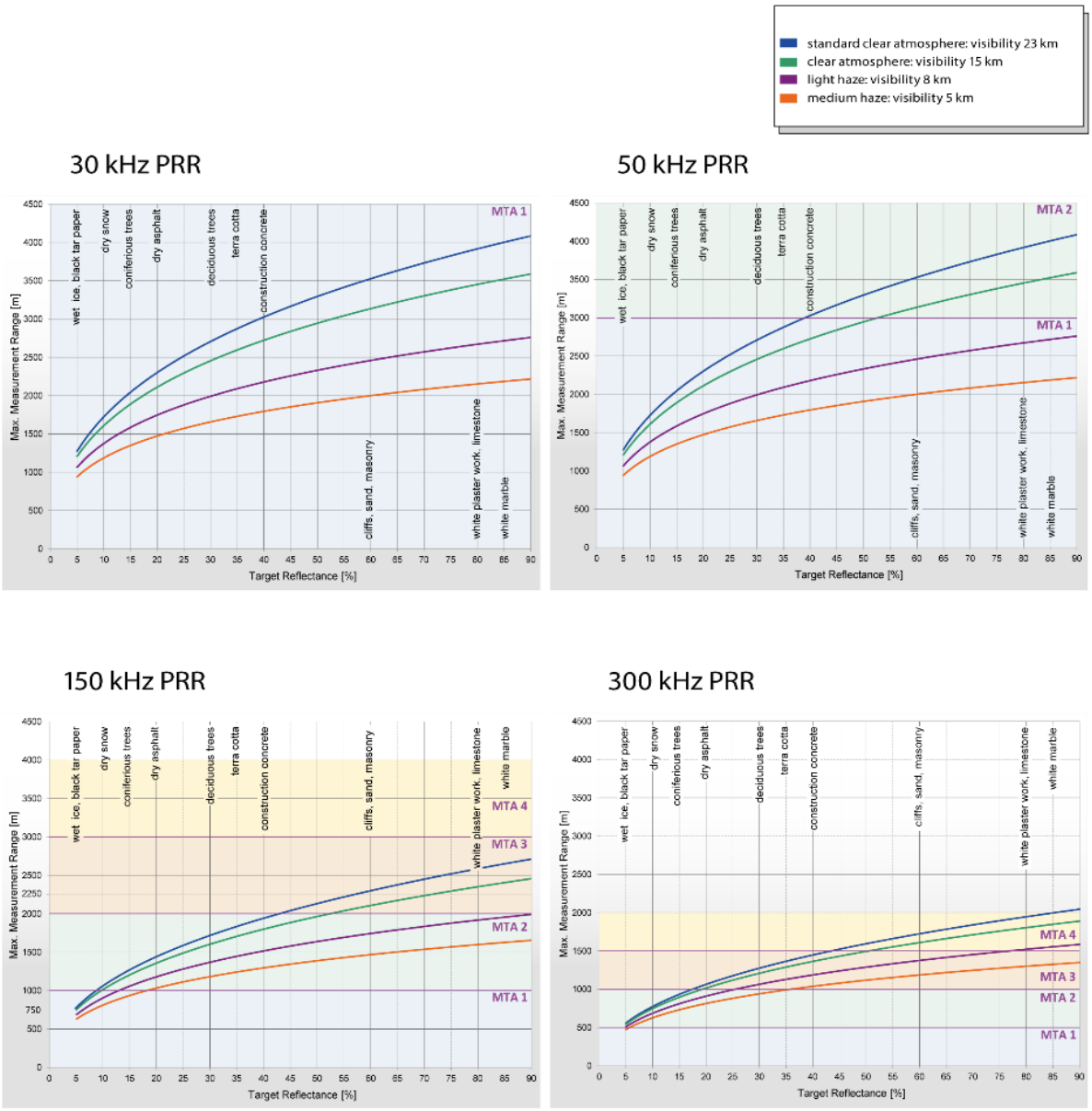

The following conditions are assumed:

- flat target larger than footprint of the laser beam
- perpendicular angle of incidence
- average brightness
- ambiguity resolved by post processing with RiMTA TLS

MTA zones:

MTA 1: no ambiguity / 1 pulse „in the air"
MTA 2: 2 pulses „in the air"
MTA 3: 3 pulses „in the air"
MTA 4: 4 pulses „in the air"

Appendix 2

Time series of profile 1 between 15:27 13th and 21:30 14th August. Grey lines are all scans between and blue these times and the blue line is the induvial scan time labelled for each plot.

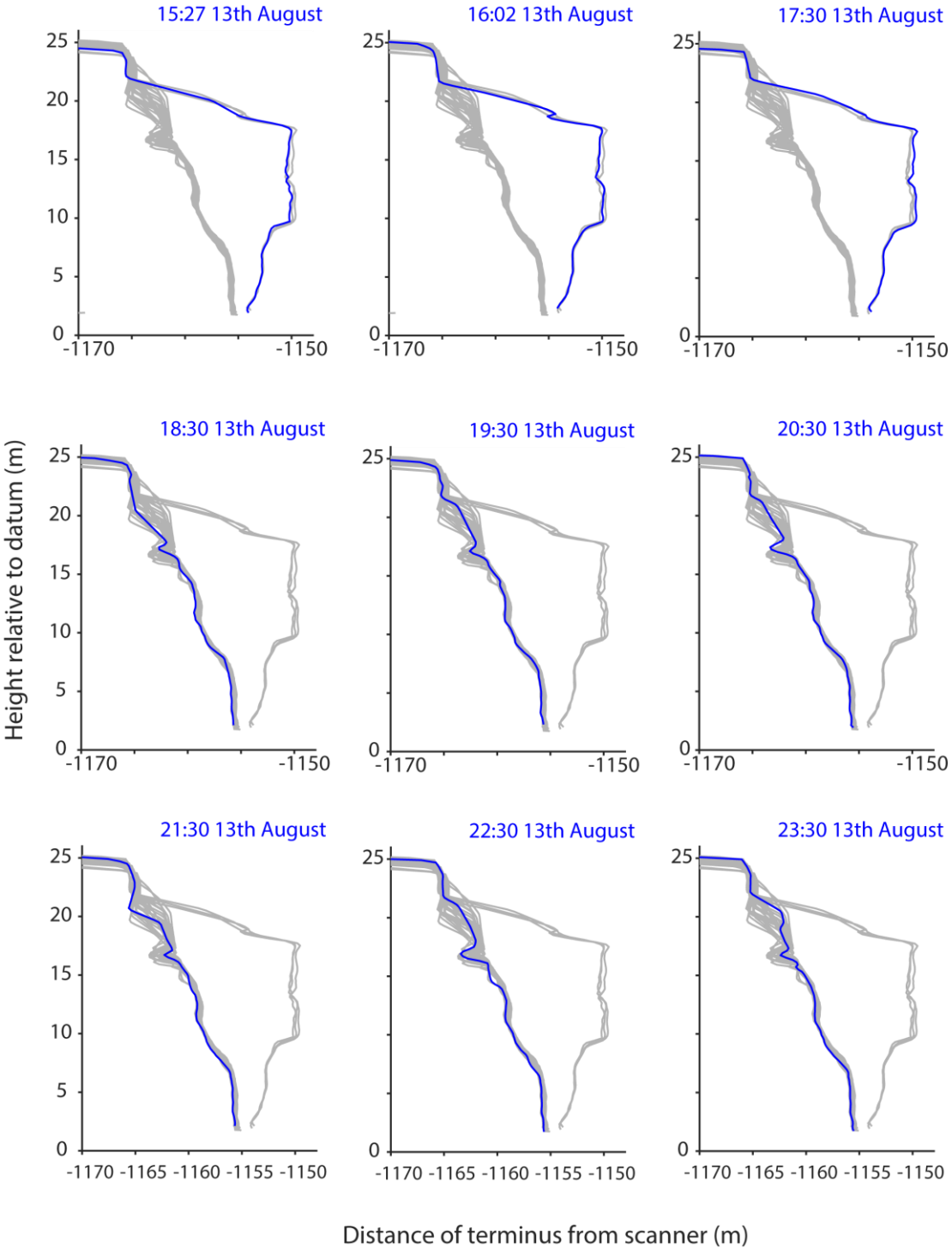

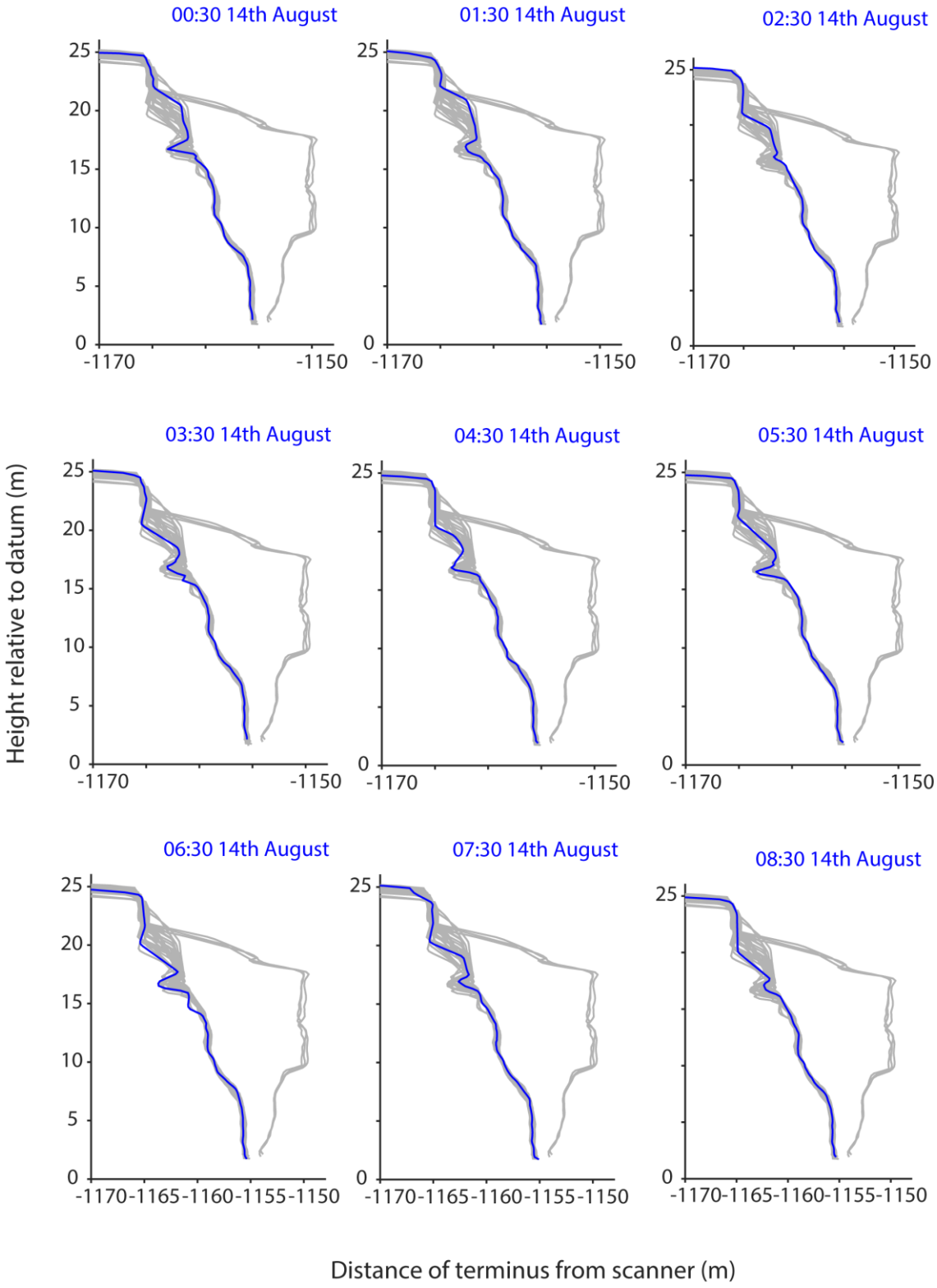
00:30 14th August
01:30 14th August
02:30 14th August
03:30 14th August
04:30 14th August
05:30 14th August
06:30 14th August
07:30 14th August
08:30 14th August
Height relative to datum (m)
Distance of terminus from scanner (m)
25
20
15
10
5
0
-1170
-1150
-1170-1165-1160-1155-1150

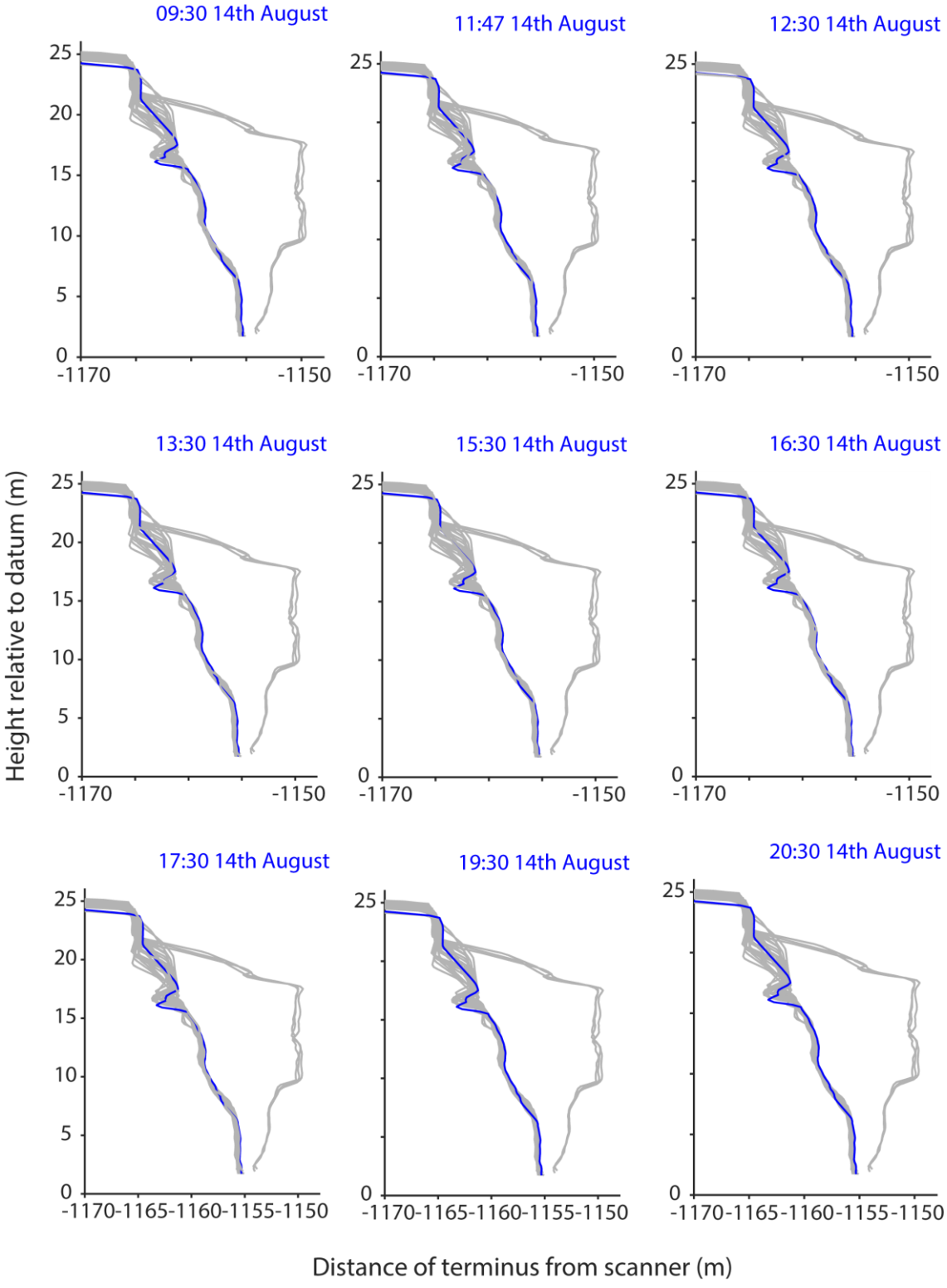
09:30 14th August
11:47 14th August
12:30 14th August
13:30 14th August
15:30 14th August
16:30 14th August
17:30 14th August
19:30 14th August
20:30 14th August
Height relative to datum (m)
25
20
15
10
5
0
-1170
-1150
-1170-1165-1160-1155-1150
Distance of terminus from scanner (m)

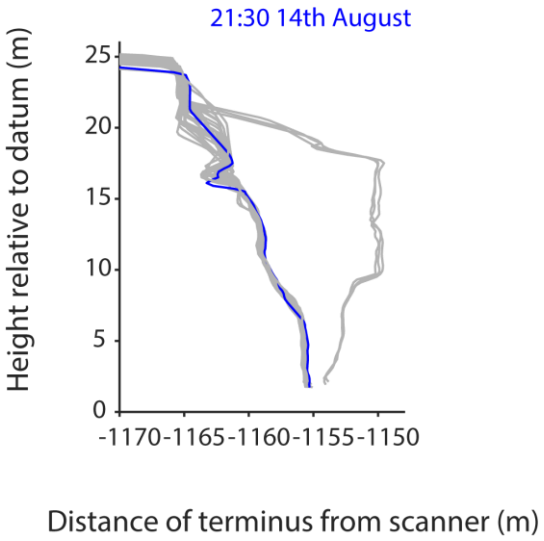
21:30 14th August
Height relative to datum (m)
25
20
15
10
5
0
-1170-1165-1160-1155-1150
Distance of terminus from scanner (m)

Appendix 3

Time series of profile 2 between 15:27 13th and 21:30 14th August. Grey lines are all scans between and blue these times and the blue line is the induvial scan time labelled for each plot.

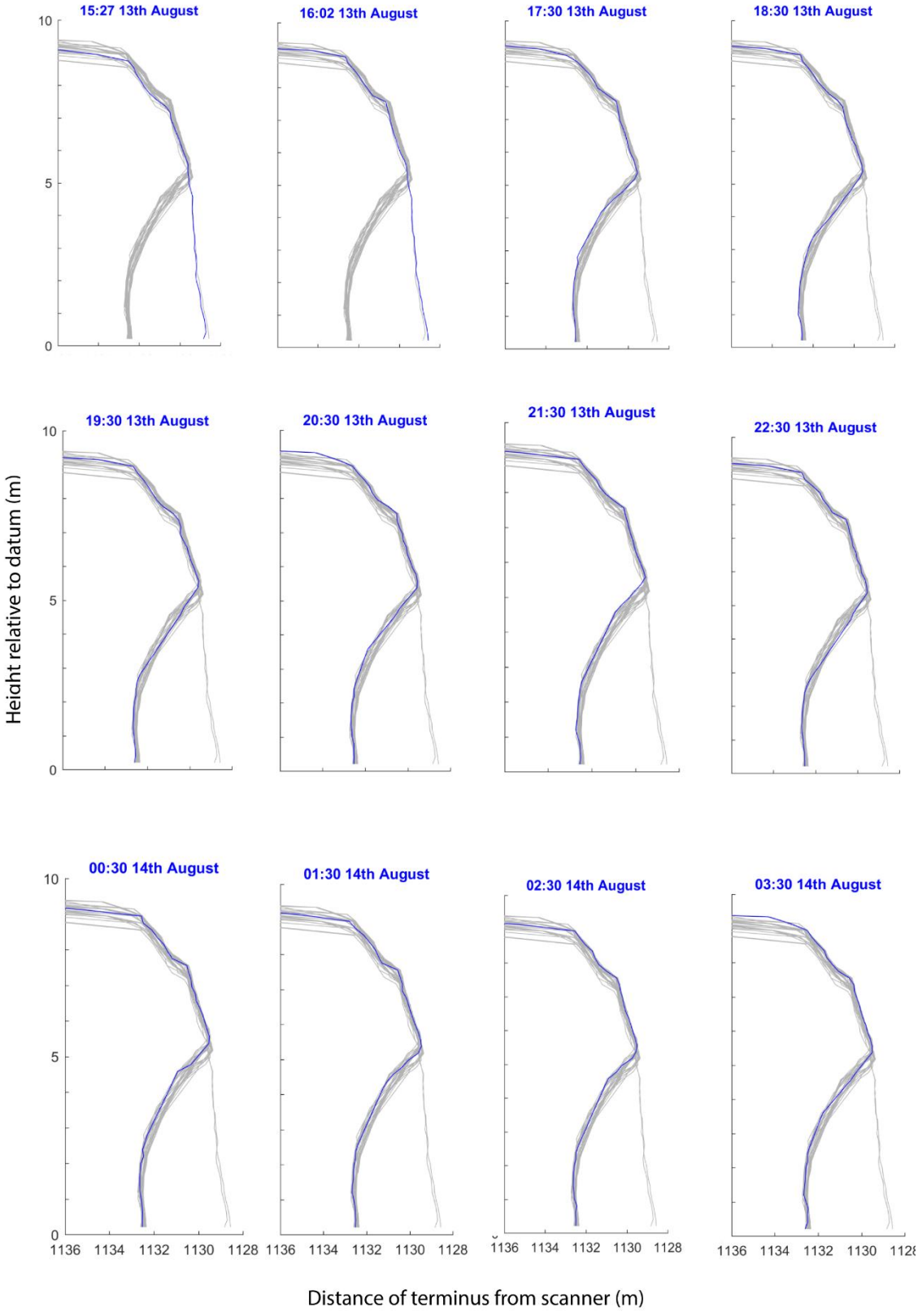

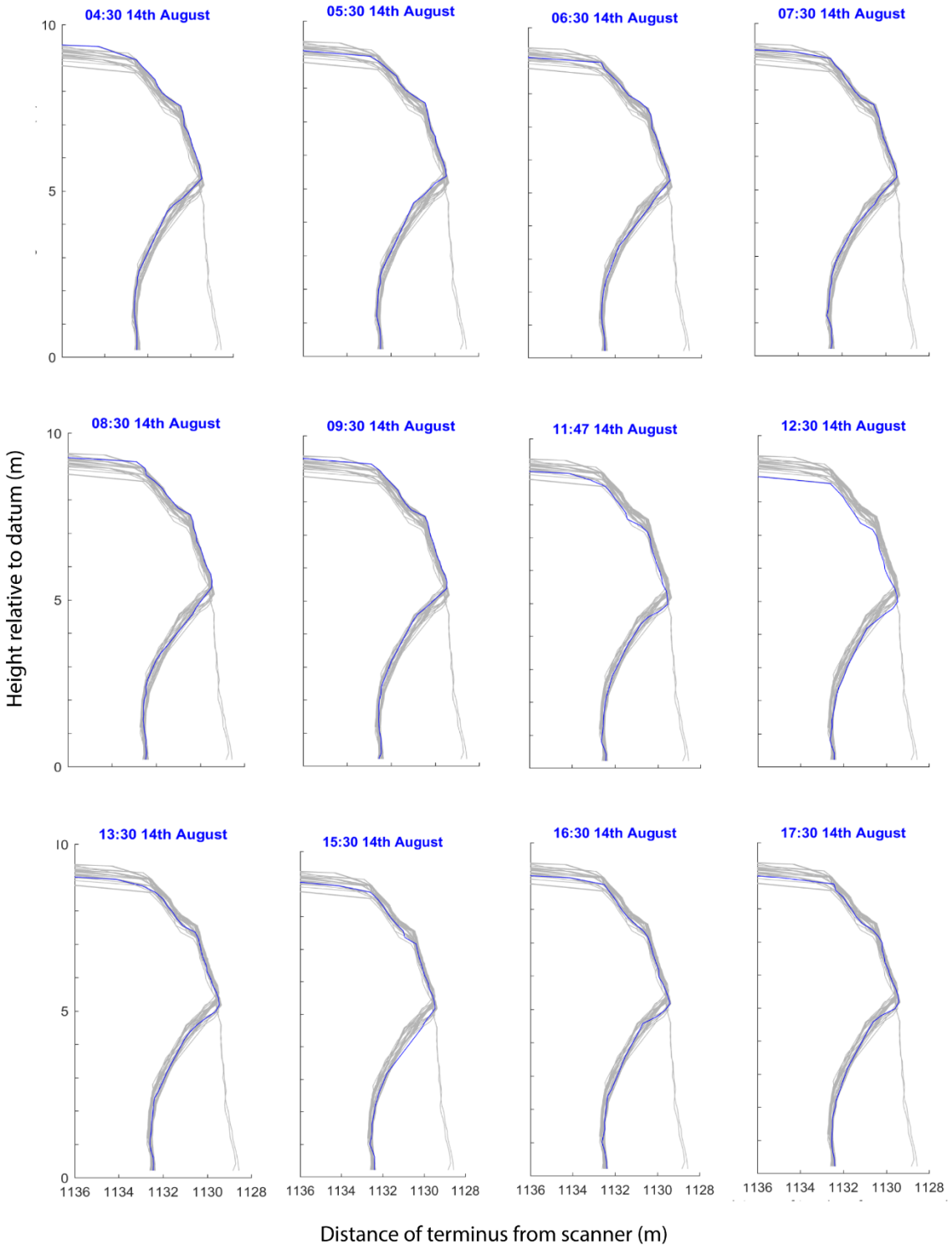
04:30 14th August
05:30 14th August
06:30 14th August
07:30 14th August
08:30 14th August
09:30 14th August
11:47 14th August
12:30 14th August
13:30 14th August
15:30 14th August
16:30 14th August
17:30 14th August
Height relative to datum (m)
Distance of terminus from scanner (m)
10
5
0
1136 1134 1132 1130 1128

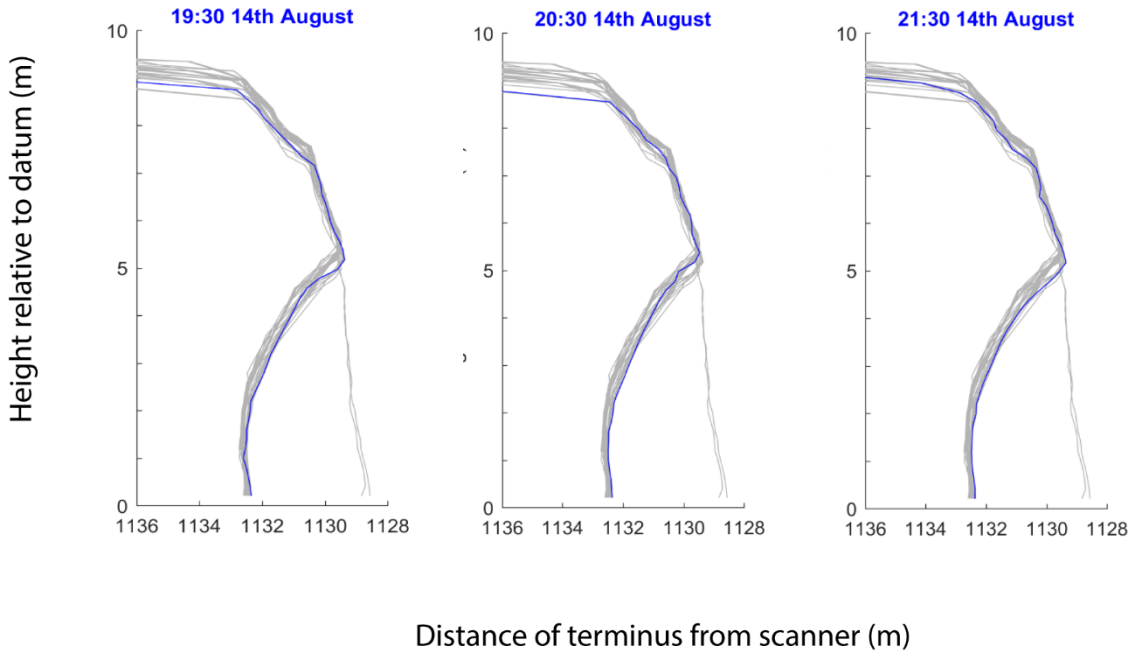
19:30 14th August
20:30 14th August
21:30 14th August
Height relative to datum (m)
10
5
0
1136
1134
1132
1130
1128
Distance of terminus from scanner (m)

Appendix 4

Time series of profile 3 between 15:27 13th and 21:30 14th August. Grey lines are all scans between and blue these times and the blue line is the induvial scan time labelled for each plot.

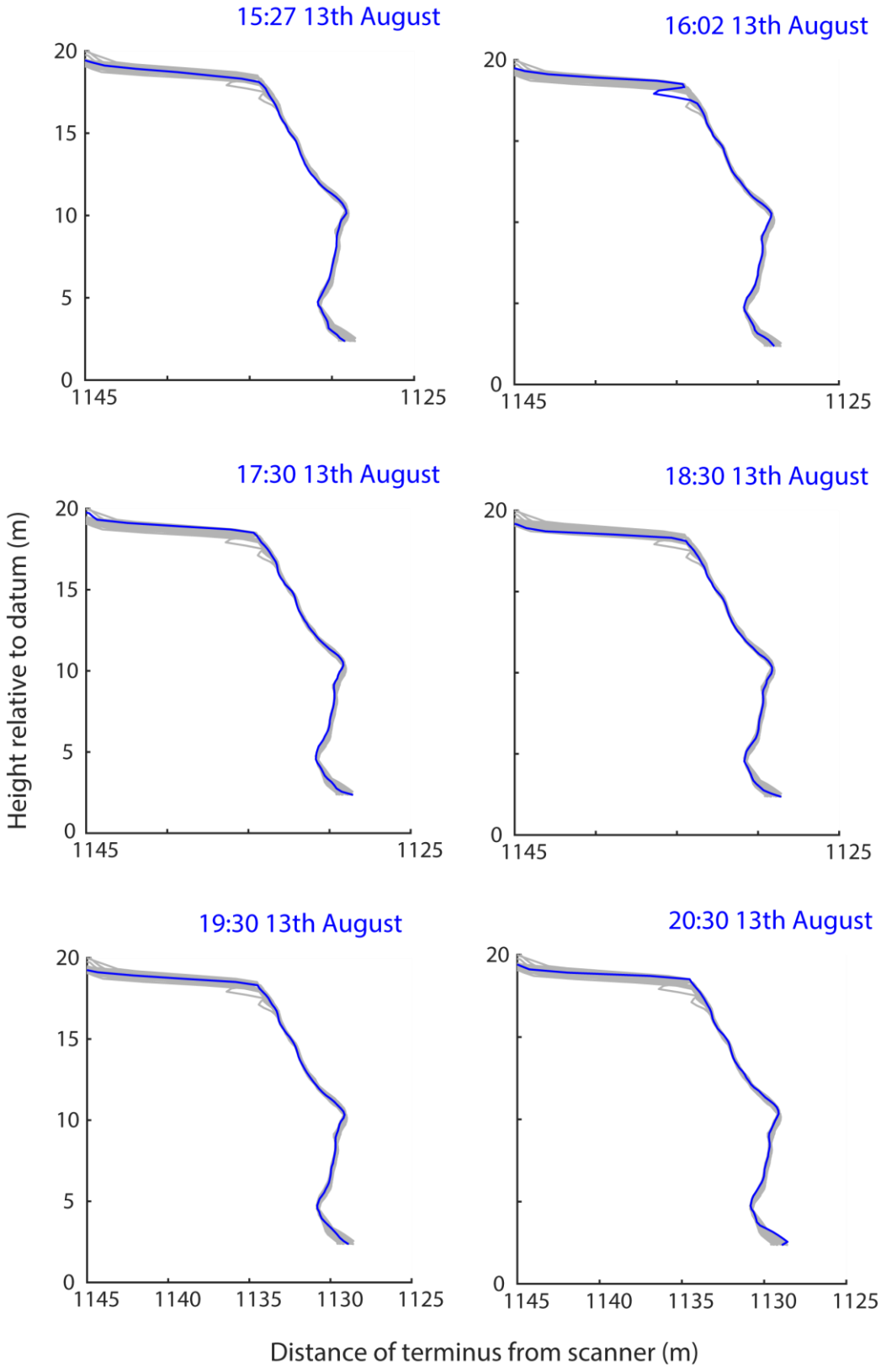

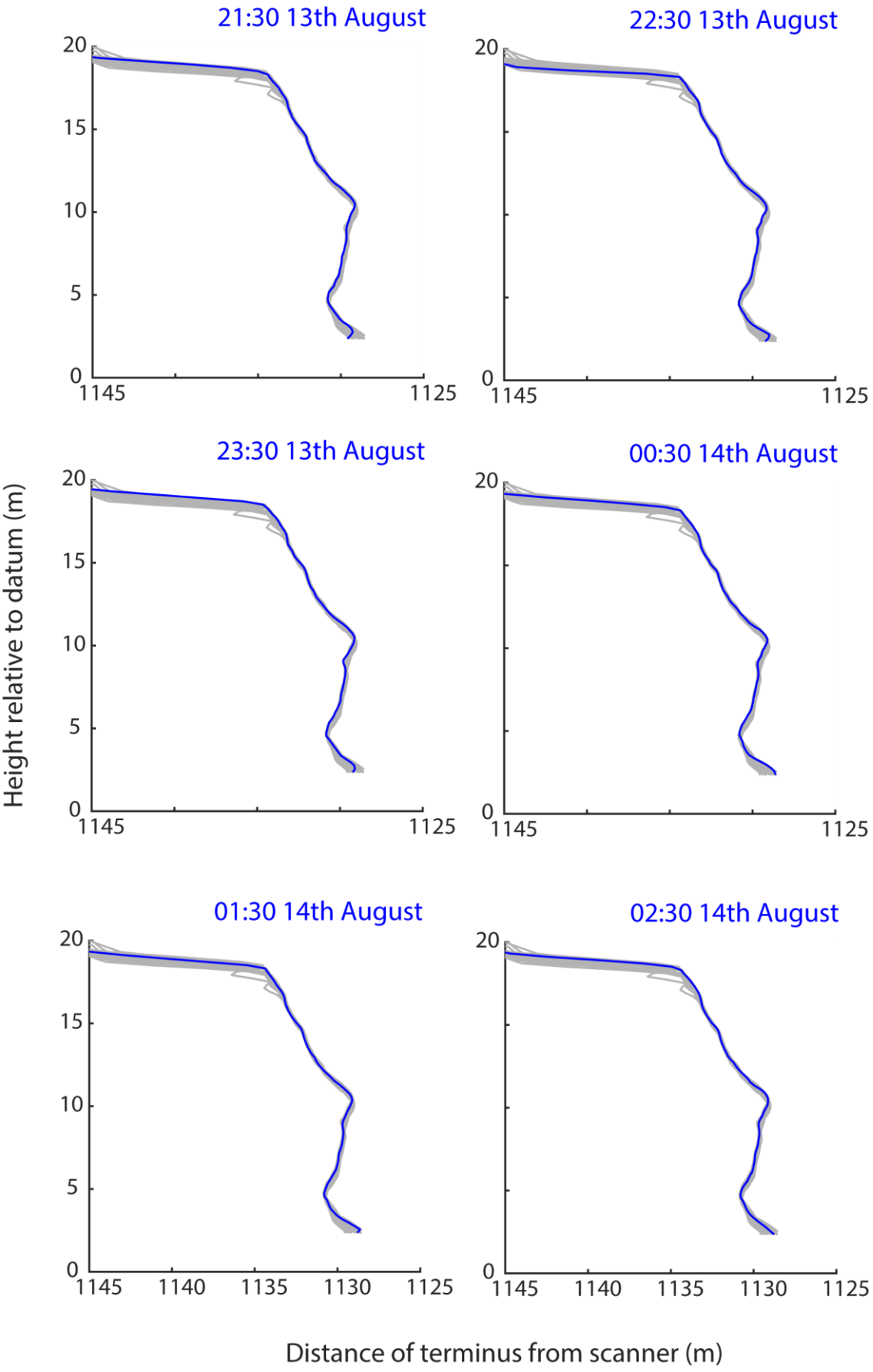
21:30 13th August
22:30 13th August
23:30 13th August
00:30 14th August
01:30 14th August
02:30 14th August
Height relative to datum (m)
Distance of terminus from scanner (m)
20
15
10
5
0
1145
1140
1135
1130
1125

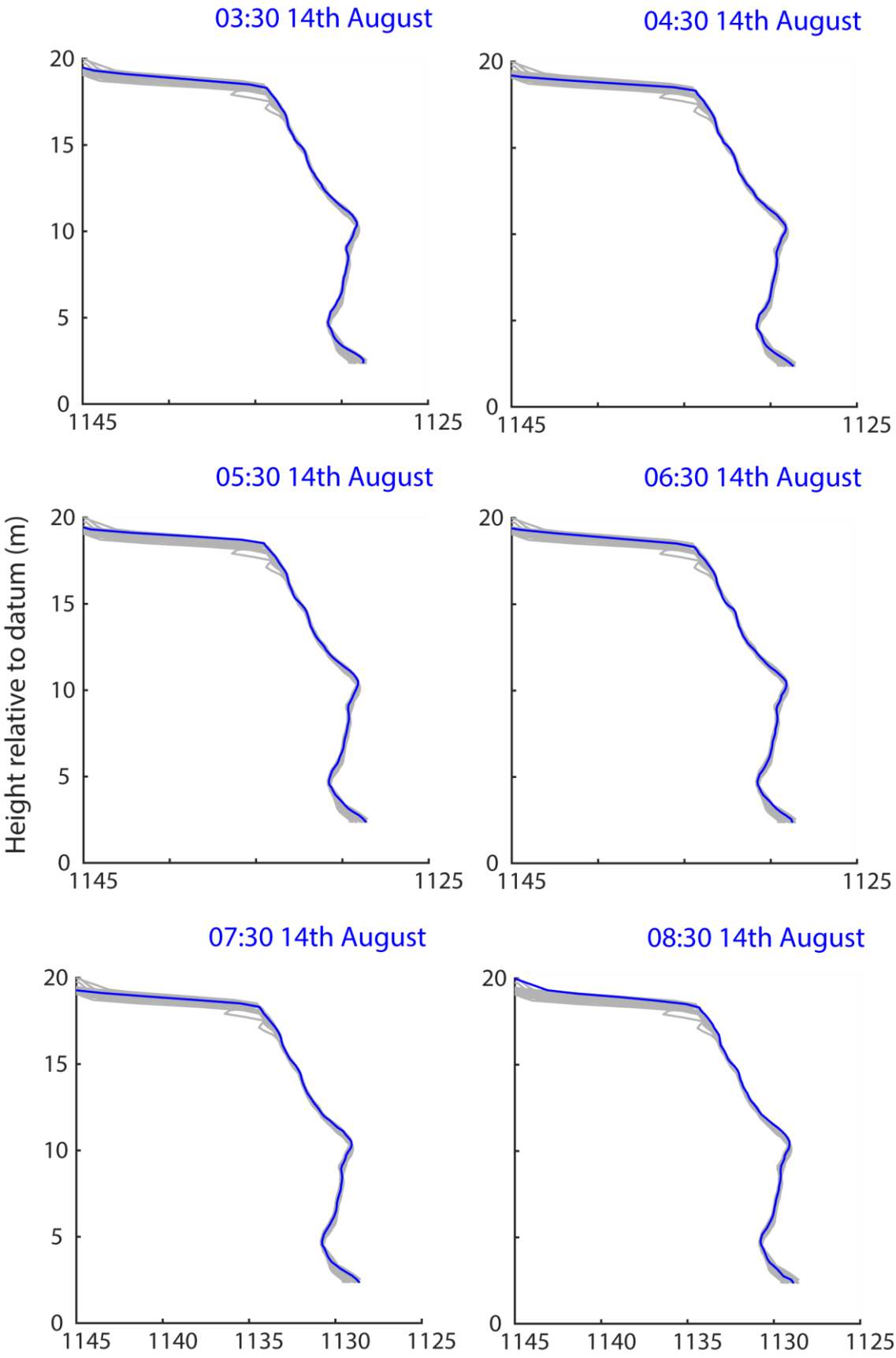
03:30 14th August
04:30 14th August
05:30 14th August
06:30 14th August
07:30 14th August
08:30 14th August
Height relative to datum (m)
Distance of terminus from scanner (m)
20
15
10
5
0
1145
1140
1135
1130
1125

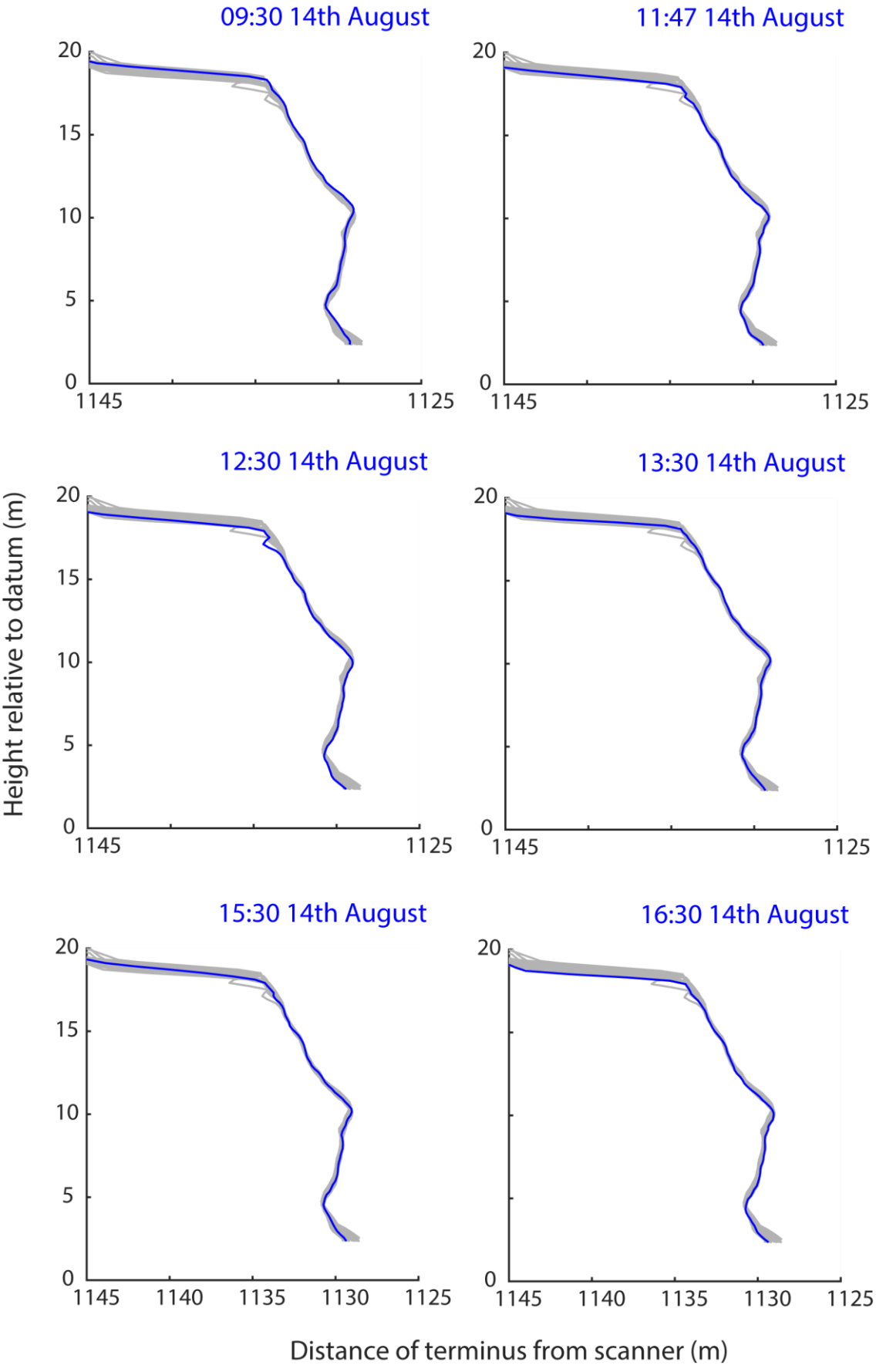
09:30 14th August
11:47 14th August
12:30 14th August
13:30 14th August
15:30 14th August
16:30 14th August
Height relative to datum (m)
Distance of terminus from scanner (m)
0
5
10
15
20
1145
1140
1135
1130
1125

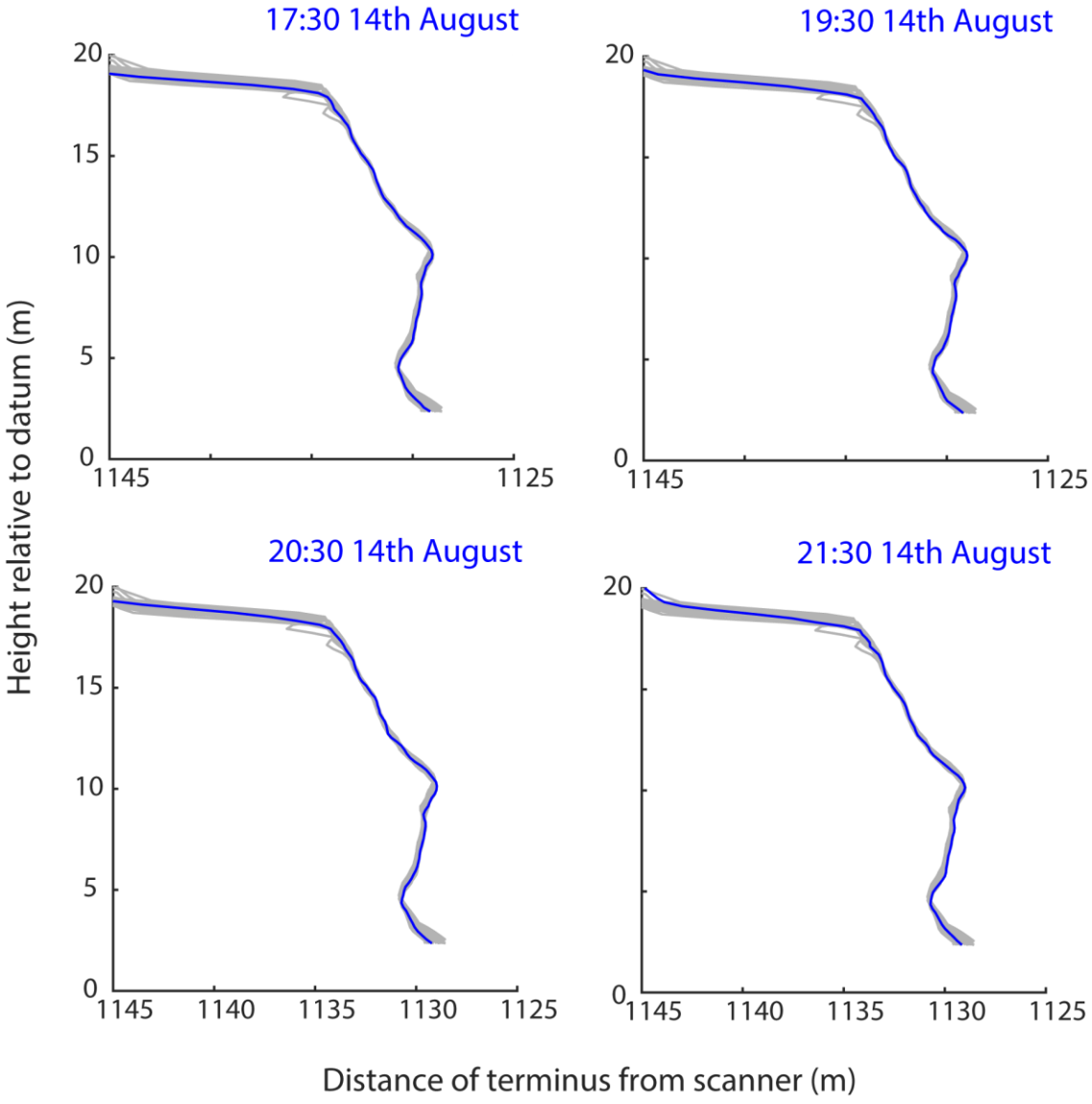
17:30 14th August
19:30 14th August
20:30 14th August
21:30 14th August
Height relative to datum (m)
Distance of terminus from scanner (m)
0
5
10
15
20
1145
1140
1135
1130
1125